Interface Engineering in SubPc/C_{60} based Organic Photovoltaics

by

Steven E. Morris

A dissertation submitted in partial fulfillment
of the requirements for the degree of
Doctor of Philosophy
(Chemical Engineering)
in the University of Michigan
2014

Doctoral Committee:

Associate Professor Max Shtein, Chair
Professor Peter F. Green
Professor Nicholas Kotov
Assistant Professor Charles W. Monroe

DEDICATION

To the pursuit of compassion, empathy, and kindness.

ACKNOWLEDGEMENTS

During my time in Ann Arbor, while working on my PhD, I have met many people who were an inspiration, source of motivation, or both. Without their presence in my life, this thesis would not be possible. I must take a moment to acknowledge their influence on me as a person and scientist, as well as the resulting influence on this work.

Of course, the members of my lab group, both past and present, have always been very supportive of me, as well as very influential of my thesis, and of great assistance with training, experiments, and discussion. I thank you for this Yiying Zhao, Brendan O'Connor, Kwang-Hyup An, Abhishek Yadav, Shaurjo Biswas, Denis Nothern, Yansha Jin, Matt Sykes, Kanika Agrawal, Adam Barito, Mark Hendryx, and Olga Shalev. I especially must point out the training and friendship from Yiying and Brendan, comradery from Shaurjo and Yansha, and discussions with Matt and Adam. To Kanika, I owe a special thanks for a great many things, but especially for helping me find myself.

Thanks to my friends and family who shared their time with me when I was outside of the lab. Kana, Indranil, and Sameer struggled with me from the very beginning. Nathan, Kelly, and Judah accepted me into their family in Michigan, with whom I made some great music and had wonderful times together. Mehreen, who opened my mind, and in which I found a kindred spirit. All of my friends in the Inter-cooperative Council and North

Campus Cooperative House – I have never before felt so included and with such purpose to my life; I hope to find it again, some day. My dear Mariana, with whom I share my joy and my pain, is always there for me without question – you have my heart. At the solid foundation of it all is my family, who always made it clear that I could succeed or fail, and I would never be judged and always welcomed home.

My thesis committee has been receptive, understanding, and helpful. Despite my fears of criticism, they have clearly shown that they wish only to see me grow and be successful. Most of all, I am thankful for my advisor, Max Shtein, for his constant dedication, can-do attitude, and especially for believing in me when I did not. Surely, we frustrated each other many times, but he always tried to give the most that he could while still ensuring I learn and grow.

TABLE OF CONTENTS

LIST OF FIGURES

LIST OF TABLES

LIST OF APPENDICES

ABSTRACT

Organic photovoltaic (OPV) devices have the potential to supply a significant portion of global electricity demand within the next 50 years. Though they're capable of rapid, inexpensive processing, current research-grade devices suffer from low efficiency and lifetime. The relationship between processing, microscopic structure the interface, and device properties is becoming well-defined to the point that suggestions for molecular structure and morphology at the interface may enable commercial viability of OPVs.

Conventionally, bilayer OPV cells involve the deposition of the electron donor layer on top of a transparent anode, with the cathode deposited last. In this work, a comparison is made between conventional (SubPc/C_{60}) and inverted (C_{60}/SubPc) junctions. There is a significant trade-off between the open circuit voltage and short circuit photocurrent, attributed to the formation of a C_{60}/ITO Schottky junction, and a change from exciton-quenching to exciton-blocking behavior of the SubPc:MoO_X interface in inverted devices. The interfaces show significant impact deposition order can have on interfaces responsible for encouraging exciton diffusion to a heterojunction.

To probe the influence of molecular dipole on the open circuit voltage (V_{OC}) of molecular heterojunction organic solar cells, axially fluorinated boron subphthalocyanine (SubPc-F) is synthesized and paired with fullerene as an acceptor. The energy levels and

structure of the heteromolecular polaron pair are calculated, and a modified ideal organic diode model is presented, successfully reproducing the experimental SubPc-F device characteristics from the SubPc-Cl device fit. The reproducible difference in V_{OC} is attributed to the permanent electric dipole on SubPc molecules effectively lowering the polaron pair binding energy, and thus influencing on polaron pair dynamics at the heterojunction. Importantly, this model has the ability to explain the low electric field dependence seen in some organic photovoltaics, as well as provide a more complete description polaron pair binding energy.

This work suggests a path forward for molecular design, with consideration for molecular orientation within the polaron pair, and incorporation of a permanent electric dipole capable of assisting polaron pair dissociation. The assistance of a dipole during dissociation could be a means of overcoming the tradeoff between high voltage and high current organic photovoltaics.

CHAPTER 1

INTRODUCTION

This chapter will reflect on the need for photovoltaic (PV) technology, particularly on organic photovoltaics as a long-term solution to some of the concerns of energy production, both in the present and in the future. As it is pertinent to this work, discussion begins with global power demands and possible solutions. Focus is maintained on renewable energy, considering the numerous, undesirable hidden costs of fossil fuels and nuclear power. After suggesting that organic photovoltaics (OPV) are possibly the most viable technology in the long term, the current challenges OPVs face before becoming viable in market are discussed. Concluding with the understanding that the efficiency must be increased, the study layout is presented – to understand the importance of molecular orientation and dipole strength at the dissociating interface, as it pertains to voltage and efficiency.

1.1 The future of energy

Worldwide power consumption in 2014 is approximately 18 TW, a number that has increased nearly 40% since the turn of the century. This growth is expected to continue, mostly as a result of rapid industrialization in developing nations such as China, India, and many African countries. Global power consumption is predicted to reach 25 TW by 2035 and 30 TW by 2050. As an interesting consideration of heavy energy usage, if everyone on Earth today had the same lifestyle and energy consumption of a citizen of the United States, at 90 MWh/yr [1], global power consumption would be an astounding 72 TW.

Fossil fuels remain the most common source of energy, supplying 83% of global energy demand. However, fossil fuels have come under harsh criticism, with widespread recognition that they are responsible for climate change, biodiversity loss, pollution, and even an unnecessarily high cost of healthcare arising from chronic illness to acute poisoning and cancer [2]. Focusing on less problematic sources, 6% of global energy is supplied from nuclear reactors, while the remaining 11% is from renewable sources (i.e. hydroelectric, wind, geothermal, and solar) [3]. The path forward over the next century is to begin shifting energy production away from fossil fuels, supplanting them with an energy infrastructure fed by a diverse range of clean, carbon-neutral sources.

Each renewable energy source has a fundamental upper limit to production. At ~0.5 TW, hydroelectric power is the most utilized renewable energy resource. Limited by availability, the upper bound to hydroelectric production is estimated to be about 1 TW. This is unfortunate, since hydroelectric power is the only renewable source that is relatively constant, day and night – an essential trait of a base load power source. Wind, limited by geographical location and wind speed variability, represents a large potential of 6 TW, and has seen strong investments in recent years, with a 5 year growth of 21% to 320 GW [4]. Other sources are geothermal and biomass, though current estimates suggest they are limited to a maximum contribution of 1 TW [5] and ~0.2 TW [6], respectively. Thinking broadly, most renewable sources arise indirectly from the Sun, due to heating and cooling of air or water, so gains can be made by harnessing the original source – the sun. With potential that dwarfs all previous mentioned power sources, the solar cell industry is growing rapidly, with demand for modules often outstripping supply. This represents the largest source of power available to the world, though it is severely underutilized.

96,000 TW of sunlight is incident upon the Earth at any moment, though there are significant limitations to the amount that is able to be harnessed. Considering only land area, since ocean installations are likely to be particularly difficult, we are limited to 28,000 TW. Assuming 2% of land is available for solar installations, we arrive at 560 TW. Solar insolation must be considered, so though 2% is an aggressive target, it will vary depending upon geography. Even with an installed module efficiency of merely 12%, which is considered low efficiency, we arrive at 67 TW of solar power, more than double the expected demand by 2050 [3]. This analysis of solar availability is illustrated in **Figure 1-1**. 67 TW is almost enough to fulfill the 72 TW needed for all 7 billion people on the planet to enjoy lavish power consumption as if living in United States.

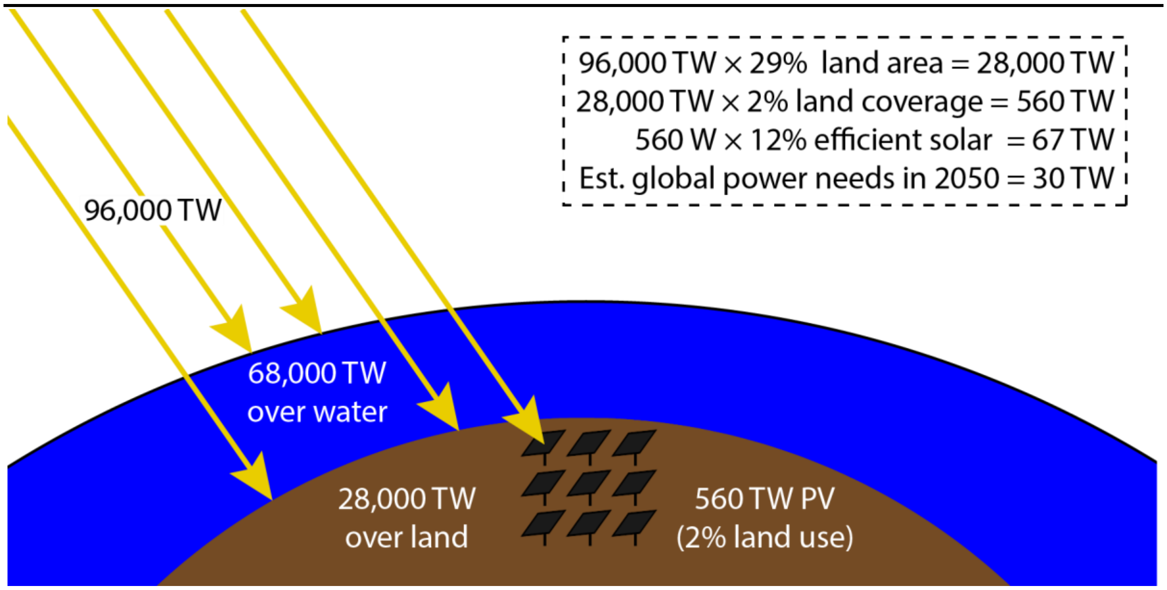

Figure 1-1 Available solar power for supplying energy to the world, assuming 12% efficient solar PV covers 2% of all land [7].

Despite the great availability of solar power, we must consider how rapidly we can produce the area of PVs needed to achieve these goals; 2% of all land area on Earth amounts to nearly 3 million km^2 or cumulative sum of all paved road area in the United States [8]. Estimates predict a continued growth averaging 22% year-over-year for the next 5 years, placing total global PV at approximately 375 GW by 2018 [9]. Though this is not yet substantial, many countries are making concentrated efforts to increase both research and production of PV modules. The U.S. Department of Energy has an aggressive plan – the SunShot initiative, which intends to achieve solar installations costing $1/W by 2020. Under this program, solar alone could produce 14% of the total U.S. electricity demand by 2030, and 27% by 2050 [10]. This is ambitious, considering less than 1% of all electricity in the U.S. was generated by solar, as of 2012. Such rapid growth requires consideration of the economics, largely in terms of subsidies driving solar adoption, as well as manufacturing capacity, and material availability, with the goal to be encouraging investment in technologies having either short or long and term viability.

Silicon panels dominate the market today, as either monocrystalline, polycrystalline, or amorphous cells. Unfortunately, production of silicon cells is costly, and additionally they are relatively heavy and fragile, keeping handling and installation costs higher than other technologies. Despite this, the maturity of the technology leads to efficiencies around 17%-21%, making them economically feasible. Other commercial technologies include thin film devices such as cadmium telluride (CdTe) and copper indium gallium diselenide (CIGS), both of which are considered second generation PV technology – high efficiency with lower costs than the first generation (i.e. silicon). However, there are concerns regarding scale-up that pertain to material scarcity, as well as toxicity regarding disposal of cadmium and selenium [7]. In particular, gallium, indium, and especially tellurium are unlikely to be available in necessary quantities for widespread use of these technologies [11]. Estimates of total production versus world reserves for critical PV elements are shown in **Figure 1-2**, with predictions that these materials will impose limits on the maximum contribution from second generation PV, totaling well below 10 TW [12]. Note that scarcity may indicate a limited supply in general, or limited economic ability to engage in large scale mining. Despite this, second generation technologies are essential to the SunShot initiative, which has three major objectives: increase efficiency, invest in technologies that lower production cost, and accelerate technology to the market. Success of the initiative will realize grid parity for much the U.S. by 2020 [10].

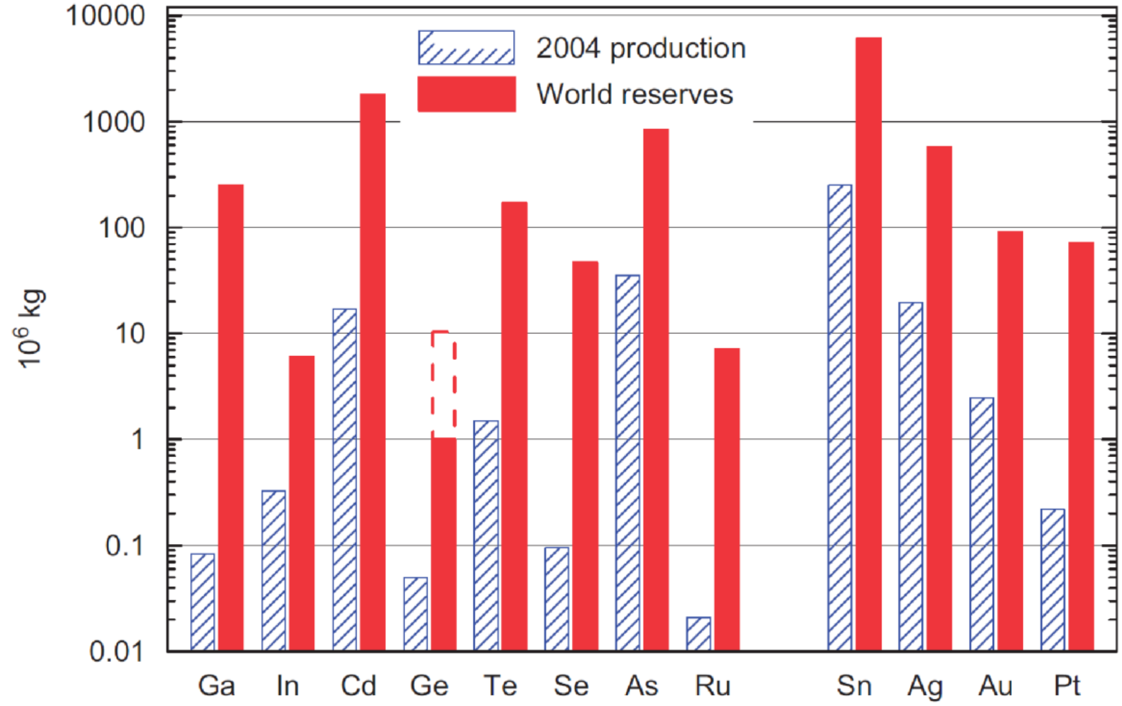

Figure 1-2 Total production of rare earth elements, as of 2004, versus estimated world reserves. The dashed line for germanium represents the best guess for world reserve. Reprinted from [12], with permission from Elsevier.

As of 2014, one of the major barriers to the suitable financial incentive for the adoption of PV technology lies in expenses that do not directly arise from the hardware or module (e.g. installation labor, financing, customer acquisition). In 2012, the cost of hardware represented only 36.4% of the total cost of an installed module, with leading non-hardware costs being that of supply chain and installation labor, at 11.7% and 10.5%, respectively [13]. The greatest opportunity for cost reduction is in new technologies that are manufactured rapidly, in a roll-to-roll process, as well as technologies that are less fragile, with low production costs – most likely processes that are solution based – which are also likely to reduce labor costs.

Only two modern technologies are not limited by rare materials, and thus have the capability for rapid scale-up: silicon and organics. Silicon is likely to remain dominant in the near future, considering its maturity, material availability, and production infrastructure. However, processing silicon is energy-intensive (i.e. expensive), and its mechanical properties lead to high soft costs, thus silicon is unlikely to remain dominant in the next 15 years. Though thin film technologies like CdTe and CIGS will replace silicon as the dominant technology, emerging technologies like OPVs appear to be the long-term solution to a PV-dominant energy infrastructure, thanks to their low material utilization of relatively abundant materials, compatibility with solution-based roll-to-roll manufacturing, ease of building-integration, and relative mechanical robustness.

1.2 Organic photovoltaics

Organic semiconductors have unique properties relative to inorganics that allow them to fill niche spaces which traditional inorganic solar cells cannot fill. Two of the greatest attributes of OPVs arise from their overall thickness of less than 200 nm: flexibility and low mass. These two advantages make OPVs excel in the area of small-scale, distributed solar devices. Potential applications include solar foils, fibers, fabrics, and lightweight coatings for energy harvesting, all of which represent new opportunities for installation and distribution that are likely to have significantly lower soft costs. These are especially important in areas where weight is important, such as wearable electronics and aerospace applications, where weight reduction is paramount.

One particular advantage OPVs have is energy payback time (EPBT), or the time the PV module must operate to produce the amount of energy required to manufacture it. Logically, every PV installation must generate more energy than was consumed during its production [14, 15], but OPVs are predicted to achieve this relatively quickly, even at low efficiency. A comparison of EPBT for OPVs versus other technologies is shown in **Figure 1-3**. The embedded energy in OPV materials is low enough that the EBPT could be measured in weeks, rather than years, as is common for inorganic cells.

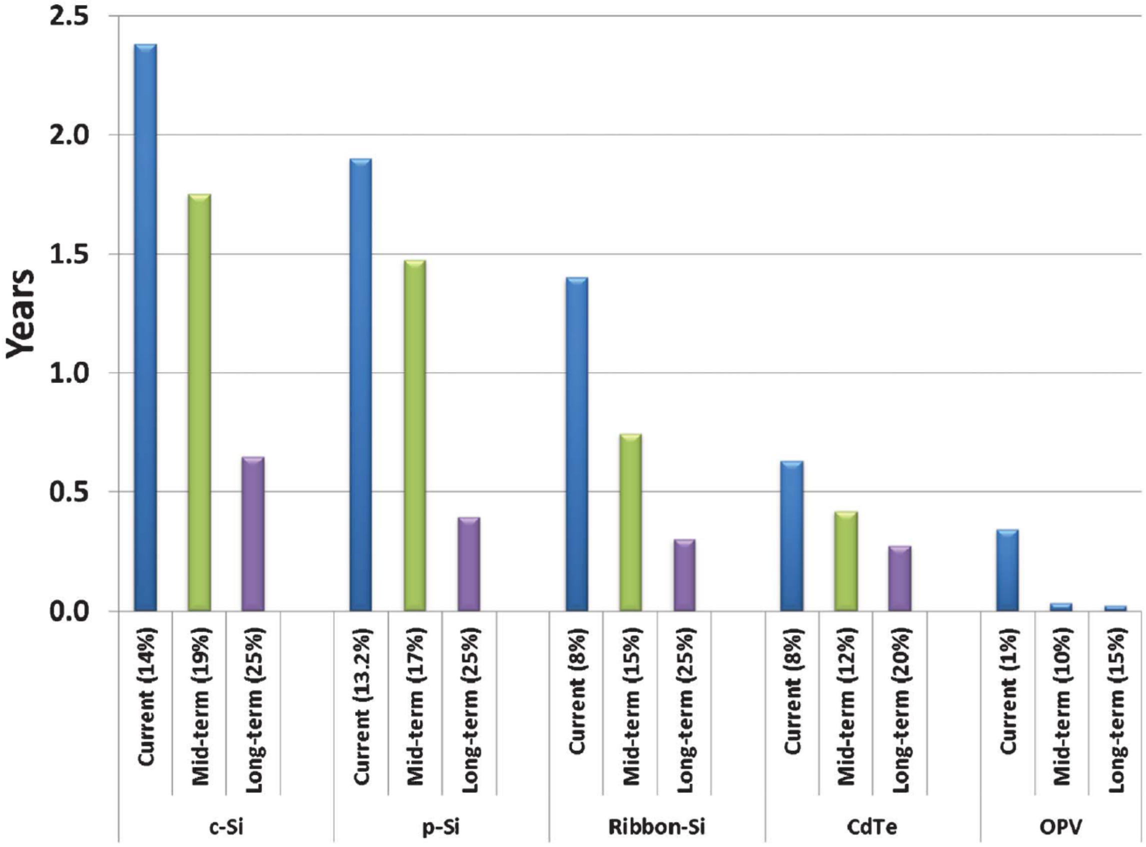

Figure 1-3 Energy payback times for PVs based on crystalline silicon, polycrystalline, ribbon silicon, CdTe, and OPV technologies. Payback time for estimated current, mid-term, and long-term efficiencies are shown for each PV type. Reproduced from Ref. [3] with permission from The Royal Society of Chemistry.

Of course, OPVs would be in widespread use today if there weren't major technological challenges to be overcome. As seen in **Figure 1-4**, the best certified research cell efficiencies for OPVs are near 11%, whereas silicon is near 25%, and both CdTe and CIGS are near 21%. Unfortunately, module efficiencies for mature technologies are approximately 80% of the best lab cell efficiencies, in general, suggesting that the best production OPV modules will be under 10% efficiency. Considering the industry expectation that 12% efficient modules are necessary for economic viability, the low efficiency of OPVs must be improved before widespread commercialization and adoption becomes a viable option, though there have been suggestions that a low-cost, reel-to-reel process operating at high production volume may need only 7% efficient cells to be cost effective [16]. Methods for improving efficiency will be discussed when exploring major energy loss mechanisms in OPVs in Chapter 2. Unfortunately, low efficiency is compounded by low operational lifetime, another significant barrier to OPV adoption.

Short operational lifetime is largely a result of degradation mechanisms related to water and oxygen exposure. Ideally, the substrate would be a cheap film of polyethylene; however, oxygen and water permeability are high in polyethylene, which will reduce the lifetime of OPVs significantly [17, 18]. Effective transparent barrier technologies (e.g. glass "lid") are not flexible or have poor impact resistance, requiring careful handling and installation, thus increasing costs. Alternatively, flexible, monolithically integrated barrier technologies do exist, but are expensive [19], so much research is focused on development of water-stable and air-stable materials for OPVs. Despite this, OPVs with lifetimes of 6 years [20] and 21 years [21] have been reported, after accelerated aging tests. Much longer lifetimes have been seen when using inverted devices, discussed in Chapter 3, which place the low work function (i.e. more reactive) materials away from the air interface. However, this method of increasing lifetime requires the substrate to be a good barrier film, which makes it difficult to overcome issues associated with the use of polyethylene, and most plastic substrates. Clearly, there is a strong need for organic materials that are efficient as well as resistant to degradation by oxygen and water, and these are the two areas of focused research in OPV companies.

As is mirrored by goals of the SunShot initiative, high efficiency at low cost, with cheap deployment strategies (e.g. BIPV) are necessary for commercial efforts to succeed. With low efficiency and lifetime, OPVs will fill niche markets first. High efficiencies are needed to bring OPVs to commercial markets, where they can be used in devices with short lifetimes such as consumer electronics. Widespread installation and integration into buildings will require improvements in operational lifetime. Both of these require fundamental research into the mechanisms of operation that will allow chemists and engineers to design the next generation of materials. The work described in this dissertation was intended to understand one of those mechanisms and suggest design principles useful for increasing OPV efficiency, specifically for the purpose of helping to establish the future of clean energy.

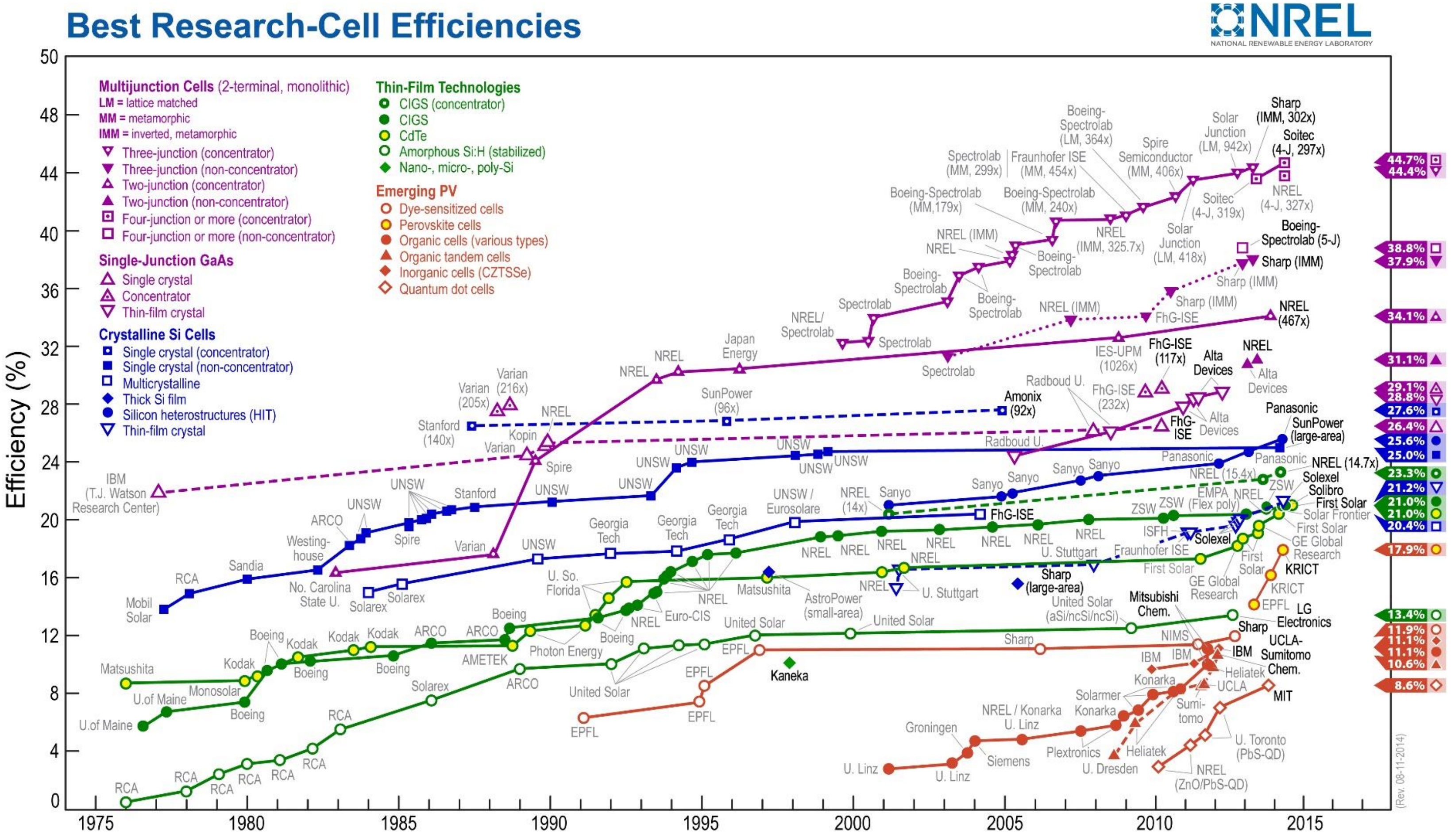

Figure 1-4 Best research cell efficiencies from 1976 through 2014, as certified by the National Renewable Energy Laboratory. Organic devices are represented by filled red circles and filled red triangles for tandem cells. This plot is courtesy of the National Renewable Energy Laboratory, Golden, CO.

1.3 Plan of Study and thesis layout

This thesis will explore the impacts of various interfaces on the performance of OPVs, with special interest on elucidating the relationship between both molecular dipole and orientation in a polaron pair on the open circuit voltage. As discussed in the previous sections, the efficiency of OPVs is not high enough to commercialize, except for niche applications. The work described below can help increase OPV efficiency through improvements to our fundamental understanding of energy transfer processes as they relate to molecular structure, orientation, and film morphology. Though many studies focus on improving the current, relatively few have investigated methods for controlling the voltage. Achieving high operating voltage is a significant challenge – energetic losses are incurred as a result of the low charge screening in OPVs, which causes coulombic binding energies to reduce voltage. This thesis focuses on the processes affecting the donor/acceptor heterojunction, as it relates to the voltage and power conversion efficiency.

A significant amount of time and effort went into development and implementation of the models necessary for the study. As such, Chapter 2 will discuss modeling, beginning with an overview of the energy transfer processes in an OPV, followed by an in-depth review of the models implemented for device design and analysis. Optical absorption modeling is followed by a brief discussion of exciton diffusion to complete external quantum efficiency (EQE) calculations necessary for an estimation of the J_{SC}. This is necessary for OPV device design, particularly for proper control experiments when evaluating different device architectures. Following this, details of diode modeling for

OPVs, which uses polaron pair geometry to estimate the device operating properties, allows for fitting of voltage-current density (JV) curves.

In Chapter 3, the discussion will first center on what molecular orientations may be present in a typical SubPc/C_{60} OPV. Starting with the naïve concept that polaron pair dynamics are affected by the interfacial morphology, which in turn may be altered with deposition order, a conventional device, in which the donor is deposited first, is prepared against an inverted device, in which the acceptor is deposited first. EQE models are first used to design the system for a similar exciton flux reaching the dissociating interface, and subsequently to confirm the operating characteristics of all films and interfaces, with surprising results that increase the iOPV current enough to make it more efficient than the cOPV. This modeling allows for isolation of the operating properties of the heterojunction.

Molecular and donor-acceptor interfacial chemical modification of the donor allows for investigation of the proposed model. Synthesis of SubPc-F, where the axial halogen atom is fluorine rather than chlorine, is followed by optical and electrical characterization. A small difference in molecular structure is accompanied by a significant difference in dipole strength. With an intent on modeling identical architectures, cOPVs were fabricated with only a change in the donor material. The resulting differences are explored with JV modeling suggested by *in silico* estimates of likely polaron pair structure and dipole strength.

Finally, future works are explored that could help refine the suggested model, and confirm the importance of permanent dipole moments, polaron pair geometry, and orientation. It may be possible to create highly optimized polaron pairs through molecular design or processing, thus leading to more efficient OPVs.

1.4 References

[1] July 2014 Monthly Energy Review, in: U.S.D.o. Energy (Ed.), U.S. Energy Information Administration, www.eia.gov, 2014.

[2] Hidden Costs of Energy:Unpriced Consequences of Energy Production and Use, The National Academies Press (2010).

[3] S.B. Darling, F. You, The case for organic photovoltaics, RSC Advances, 3 (2013) 17633-17648.

[4] Global Wind Report Annual Market Update 2013, Global Wind Energy Council, Brussels, Belgium, 2013, pp. 21.

[5] Ipcc, Special Report on Renewable Energy Sources and Climate Change Mitigation, Cambridge University Press, United Kingdom and New York, NY, USA, 2011.

[6] A.L. P. Meisen, Ocean Energy Technologies for Renewable Eenrgy Generation, Global Energy Network Institute, 2009.

[7] V. Fthenakis, Sustainability metrics for extending thin-film photovoltaics to terawatt levels, MRS Bulletin, 37 (2012) 425-430.

[8] The radius of the Earth is assumed to be 6370 km, with of the area 29.2% being land, and 2% of that being solar cells.

[9] S.O. Gaëtan Masson, Manoël Rekinger, Global Market Outlook For Photovoltaics 2014-2018, in: T. Rowe (Ed.), European Photovoltaic Industry Association, 2014.

[10] SunShot Vision Study, in: U.S.D.o. Energy (Ed.), Department of Energy, Washington, D.C., 2012.

[11] A.J. Hurd, R.L. Kelley, R.G. Eggert, M.-H. Lee, Energy-critical elements for sustainable development, MRS Bulletin, 37 (2012) 405-410.

[12] A. Feltrin, A. Freundlich, Material considerations for terawatt level deployment of photovoltaics, Renewable Energy, 33 (2008) 180-185.

[13] B. Friedman, Benchmarking non-hardware balance of system (soft) costs for U.S. photovoltaic systems, using a bottom-up approach and installer survey, Second edition. ed., National Renewable Energy Laboratory, Golden, Colorado, 2013.

[14] K. Knapp, T. Jester, Empirical investigation of the energy payback time for photovoltaic modules, Solar Energy, 71 (2001) 165-172.

[15] E. Alsema, Energy requirements of thin-film solar cell modules—a review, Renewable and Sustainable Energy Reviews, 2 (1998) 387-415.

[16] C.J. Mulligan, M. Wilson, G. Bryant, B. Vaughan, X. Zhou, W.J. Belcher, P.C. Dastoor, A projection of commercial-scale organic photovoltaic module costs, Solar Energy Materials and Solar Cells, 120, Part A (2014) 9-17.

[17] N. Grossiord, J.M. Kroon, R. Andriessen, P.W.M. Blom, Degradation mechanisms in organic photovoltaic devices, Organic Electronics, 13 (2012) 432-456.

[18] M.P. Nikiforov, J. Strzalka, S.B. Darling, Delineation of the effects of water and oxygen on the degradation of organic photovoltaic devices, Solar Energy Materials and Solar Cells, 110 (2013) 36-42.

[19] L. Moro, R.J. Visser, Barrier Films for Photovoltaics Applications, Organic Photovoltaics, Wiley-VCH Verlag GmbH & Co. KGaA, 2009, pp. 491-510.

[20] C.H. Peters, I.T. Sachs-Quintana, J.P. Kastrop, S. Beaupré, M. Leclerc, M.D. McGehee, High Efficiency Polymer Solar Cells with Long Operating Lifetimes, Advanced Energy Materials, 1 (2011) 491-494.

[21] F.C. Krebs, Summary and Outlook, Stability and Degradation of Organic and Polymer Solar Cells, John Wiley & Sons, Ltd., 2012, pp. 331-332.

CHAPTER 2

OPV DEVICE MODELING

Numerical device modeling is an important method to elucidate more fundamental properties of materials from well-defined physics and experimental measurements. The studies herein focus on models used for organic optoelectronic devices, which are probed through, as the term suggests, optical and electrical measurements. The goal of these models is to map energy transport and conversion rates throughout the device, to elucidate material and device parameters from well-defined relations and macroscopic measurements.

2.1 OPV Basics

A fundamental OPV stack consists of only four films – anode, electron donor, electron acceptor, and cathode. The donor and acceptor often both absorb light. In a conventional device, the light source illuminates the active layers through a transparent anode, with a “second pass” afforded by a reflective cathode. This type of cell was first demonstrated in 1986 by C.W. Tang, and birthed the field of heterojunction OPVs, which are now by far the dominant organic solar cell architecture [1].

A conventional OPV stack is shown inset in **Figure 2-1**. The donor and acceptor are together known as the active layers, responsible for collecting photons and generating free charges that are collected by the cathode and anode. The interface formed between the two active layers is the heterojunction, which is responsible for a majority of the diode behavior measured in a current density-voltage (JV) sweep. Often, there will also exist a buffer layer between any active layer and adjacent electrode, which is responsible for increasing efficiency through modifying the work function and controlling exciton diffusion, as discussed in section 2.2.2.

For photovoltaics, the JV behavior is characterized by four parameters, as shown in **Figure 2-1**. The short circuit current density (J_{SC}) is current density at a zero bias, or under no external load. Under operation, this will be the largest current density available. The open circuit voltage (V_{OC}) is the bias required to reduce the total current to zero. It is the maximum voltage attainable during cell operation, corresponding to an infinite external load. The fill factor (FF) and power conversion efficiency (PCE) relate the maximum electrical power to the V_{OC} and J_{SC} according to Eq. (2-1), where P_{inc} is the power of incident light,

$$PCE = \frac{V_{OC} J_{SC} FF}{P_{inc}}. \tag{2-1}$$

The FF represents the "squareness" of the JV curve, and represents a metric for the ideality of a diode is. The PCE is simply the ratio of maximum electrical power done by the PV divided by the power of the incident light, or the ratio of electrical power out to optical power in. Additional characterization parameters that relate to materials properties (e.g. saturation current, J_S, and ideality factor, n) are discussed in section 2.4.

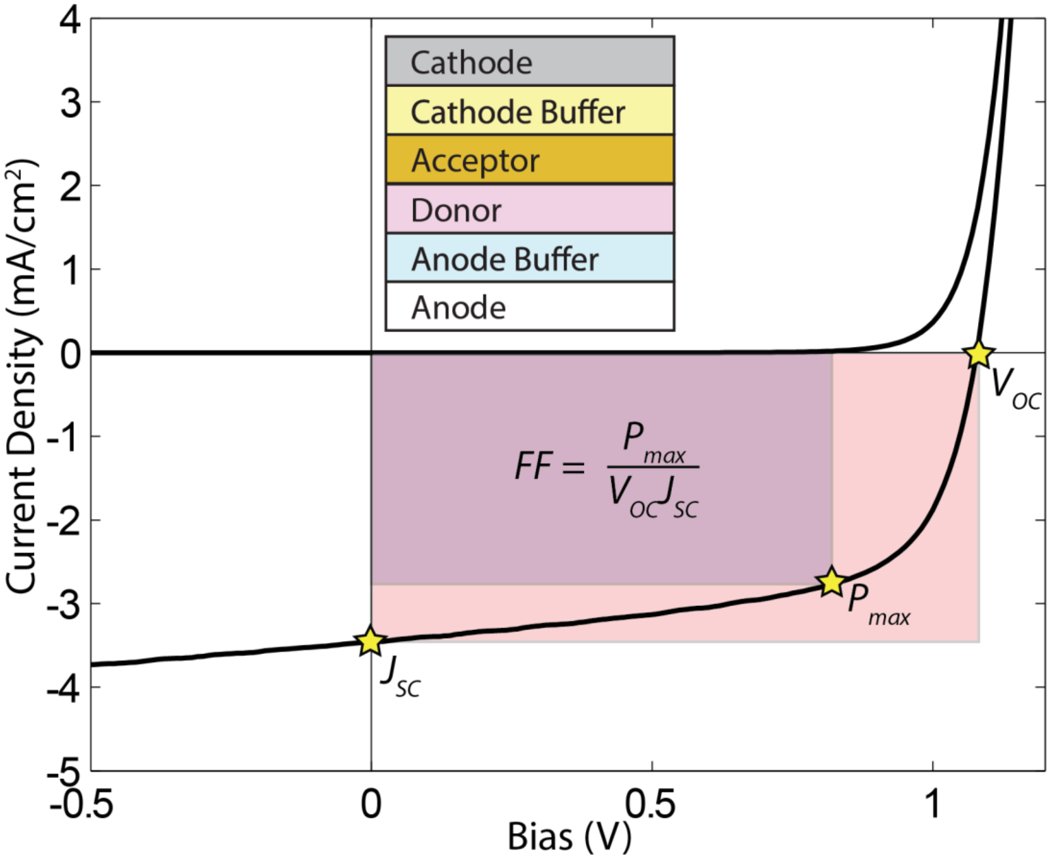

Figure 2-1 Example JV curve showing V_{OC}, J_{SC}, P_{max}, and *FF*. A basic, conventional OPV stack is shown in the upper center.

There is a limit to the maximum efficiency attainable by a PV cell. Through a detailed balance of energy absorption and radiative recombination within inorganic PVs, Shockley and Queisser calculated the upper limit to efficiency in a single-junction photovoltaic, dependent upon the optical band gap (E_g). For E_g = 1.1 eV (i.e. silicon) this limit is 29%, whereas 33.7% is the highest efficiency possible, corresponding to a band gap of 1.34 eV [2]. Recently, Rau, Paetzold, and Kirchartz updated these thermodynamic calculations to consider light trapping, non-radiative recombination, and entropic losses associated with the V_{OC} [3]. As seen in **Figure 2-2**, the losses are associated with (i) absorption of photons with an average energy lower than that of the full solar spectrum, as limited by E_g, (ii) Carnot (i.e. reversible) entropy generation, (iii) thermalization of photons above E_g, (iv) étendue expansion – irreversible entropy generation due to an increase in directional disorder, and (v) non-radiative recombination (i.e. entropy generated from carrier recombination). This is particularly useful for predicting PV efficiency based on the light management scheme employed. The maximum cell efficiency is proportionally reduced with any reduction in V_{OC}. Here, the focus is on non-radiative losses, which can affect both the J_{SC}, due to recombination in the bulk of the film, and V_{OC}, due to binding energy and recombination at the heterojunction. Both of which, along with FF, are essential to an efficient PV, thus the goal is to understand the fundamental processes underlying the origins of each.

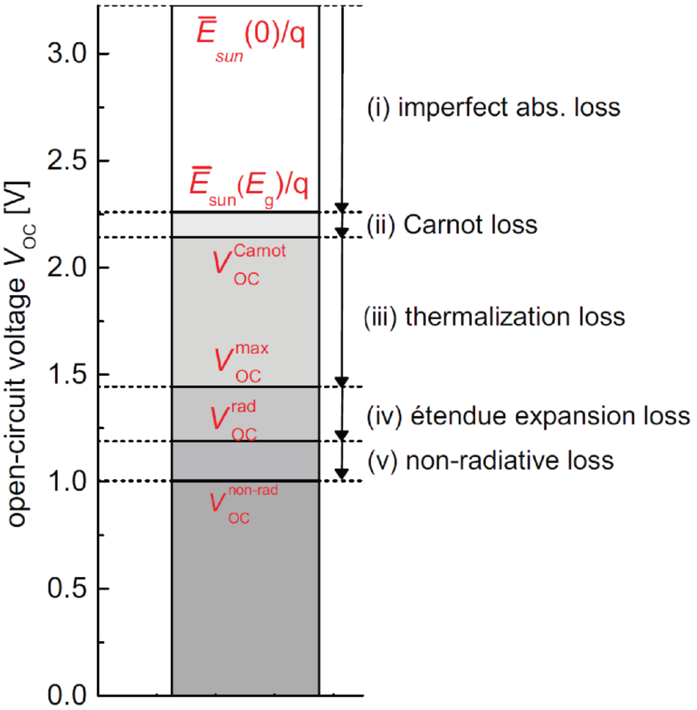

Figure 2-2 Diagram of thermodynamic losses before arriving at measured V_{OC}, with E_g = 1.38 eV. Reprinted by permission from Macmillan Publishers Ltd: Physical Review B [3], copyright (2014).

2.2 Quantum efficiency, and the origin of J_{SC}

There are four steps to energy transfer in an organic solar cell. The stages are shown in **Figure 2-3**, each with an associated efficiency. In organic semiconductors, we consider the highest occupied molecular orbital (HOMO), and lowest unoccupied molecular orbital (LUMO), analogous to the valence and conduction band in inorganic semiconductors. The first step is absorption of photons to generate electron-hole pairs. Due to their low dielectric constant (n ~ 3), the electron and hole form a tightly bound state know as an exciton. Such excitons in organics are typically Frenkel in nature, with an excited hole and electron residing in the HOMO and LUMO, respectively, of one molecule. Following absorption, excitons diffuse throughout the organic layers, preferably encountering a heterojunction, where dissociation of the excited state into a (trapped) hole and an electron can occur.

A distinct characteristic of a donor material is that both the HOMO and LUMO must be closer to the vacuum energy than in the corresponding acceptor, though donors are often also additionally characterized as having a high hole mobility. This creates an energy level offset between the donor HOMO and acceptor LUMO, ΔE_{HL}, which is necessary for exciton dissociation, or charge transfer (CT), where the difference in LUMO levels (or HOMO levels) causes the electron (hole) of an exciton to transfer to an adjacent acceptor (donor) molecule from the donor (acceptor). Being low permittivity materials, the charges will also impose a distortion on the molecular structure or crystal lattice [4]. We thus refer to polarons instead of charges. The charges remain Coulombically bound across the heterojunction as a polaron pair. In the event of both charge transfer of an exciton and dissociation of the polaron pair, free polarons (i.e. charge carriers) may be collected at the electrodes.

To summarize, the sequence of energy transfer events and their associated efficiency is as follows: (i) photon absorption, η_A, (ii) exciton diffusion, η_{ED}, (iii) exciton dissociation, η_D, and (iv) charge collection η_{CC}. The product of these efficiencies is the external quantum efficiency (EQE), summarized in Eq. (2-2),

$$EQE = \eta_A \eta_{ED} \eta_D \eta_{CC}. \tag{2-2}$$

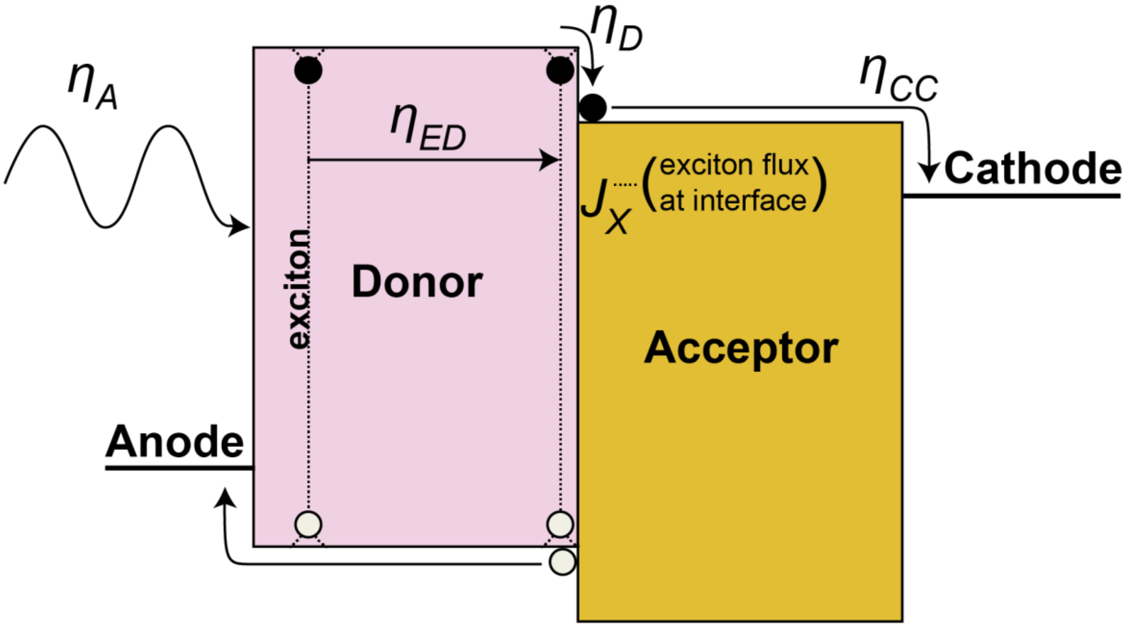

Figure 2-3 Energy level diagram for a basic 4-layer OPV. The four energy transfer processes represented are photon absorption, η_A, exciton diffusion, η_{ED}, exciton dissociation, η_D, and carrier collection, η_{CC}.

Note that EQE is a wavelength-dependent function, as are η_A and η_{ED}. Convolution of the EQE with the wavelength-dependent solar photon flux, $\phi(\lambda)$, according to Eq. (2-3), leads to a prediction of J_{SC} under solar illumination,

$$J_{SC} = q \int EQE(\lambda)\phi(\lambda)d\lambda. \tag{2-3}$$

Thus, calculation of the J_{SC} requires a model for each efficiency, optical absorption, exciton diffusion, exciton dissociation, and carrier collection.

2.2.1 Optics

Optical modeling of thin film stacks, for the purpose of calculating $\eta_A(\lambda)$, is one of the most important aspects of proper device design and analysis. Generally, every film comprising the stack, except the substrate, is on the order of 10 nm to 100 nm – much thinner than the wavelength of light. This requires any model to consider the effects of near-field interference, scattering, and depth-dependent absorption, including any parasitic absorption occurring in the substrate and electrodes. Importantly, these films are optically homogeneous, with well-defined interfaces between materials. This approach allows for simplifications including the assumption that light within the optical microcavity remains coherent.

Modeling of the optics of thin film stacks is accomplished through the transfer matrix method, which can solve for the spatially-varying optical electric field for further calculation of depth-dependent absorption, including the effects of interference resulting from multiple reflections at each interface within the stack [5, 6]. Briefly, the transfer matrix method is a formalism for the calculation of absorption, refraction, and reflections in optical stacks comprised of layers with layers sub-wavelength thickness. This calculation requires knowledge of the thickness and complex refractive index for each layer, comprised of the index of refraction, n, and extinction coefficient, k, for calculation of the Fresnel reflection and transmission coefficients at each interface, and the intensity attenuation incurred during propagation through each layer. A more detailed explanation of this model is found in Section 2.3 and 2.4 of reference [7], and the associated MATLab code is found in Appendix A. No modifications have been made to the basic method, though capabilities of the code have been expanded for rapid combinatorial calculation of varying thicknesses and materials within the stack.

Having calculated the total transmission, T, and reflection, R, for the stack, conservation of energy provides Eq. (2-4) for calculation of absorption, A,

$$\mathrm{A} + \mathrm{T} + \mathrm{R} = 1. \tag{2-4}$$

Total absorption for an example stack comprised of 150 nm ITO \ 5 nm MoO_X \ 13 nm SubPc \ 36 nm C_{60} \ 10 nm BCP \ 100 nm Al is plotted as the thick black line in **Figure 2-4**.

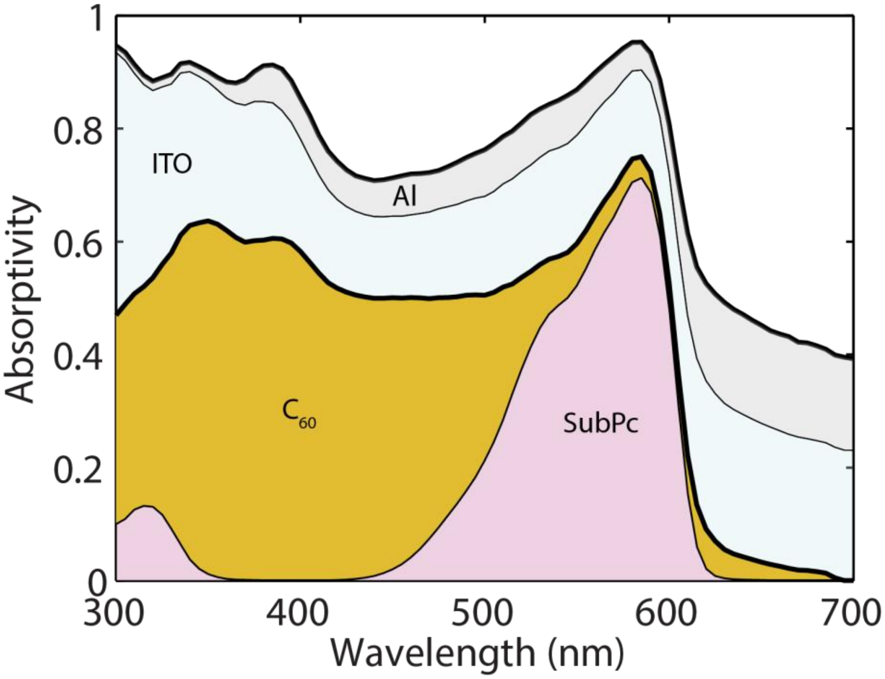

Figure 2-4 Calculated absorption curves for the example stack, 150 nm ITO \ 5 nm MoO_X \ 13 nm SubPc \ 36 nm C_{60} \ 10 nm BCP \ 100 nm Al, including absorption contribution from each individual layer. Absorption in MoO_X and BCP is negligible. In this case, transmission is zero for all of the visible range, thus all that is not absorbed is reflected. Note that the sum of absorption for the SubPc and C_{60} layers is η_A.

This stack will be used for throughout the rest of Chapter 2. Considering that transmission is negligible, the white region above the absorption curve is the reflectivity of the stack. Absorption of each individual film is shown in the shaded regions.

The presence of a metal electrode, which forces the optical electric field to reach zero in the reflective layer, combined with multiple reflections at other interfaces, forms a weak microcavity in which electric field confinement enhances absorption within the stack. Attenuation of the electric field is proportional to the imaginary term of the complex refractive index – the extinction coefficient, *k*. The solution for two wavelengths is plotted in **Figure 2-5**. 595 nm is the wavelength of peak absorption in SubPc, and 450 nm is strongly absorbed in C_{60}. Note that each wavelength peaks in its film of strongest absorption – this is by design.

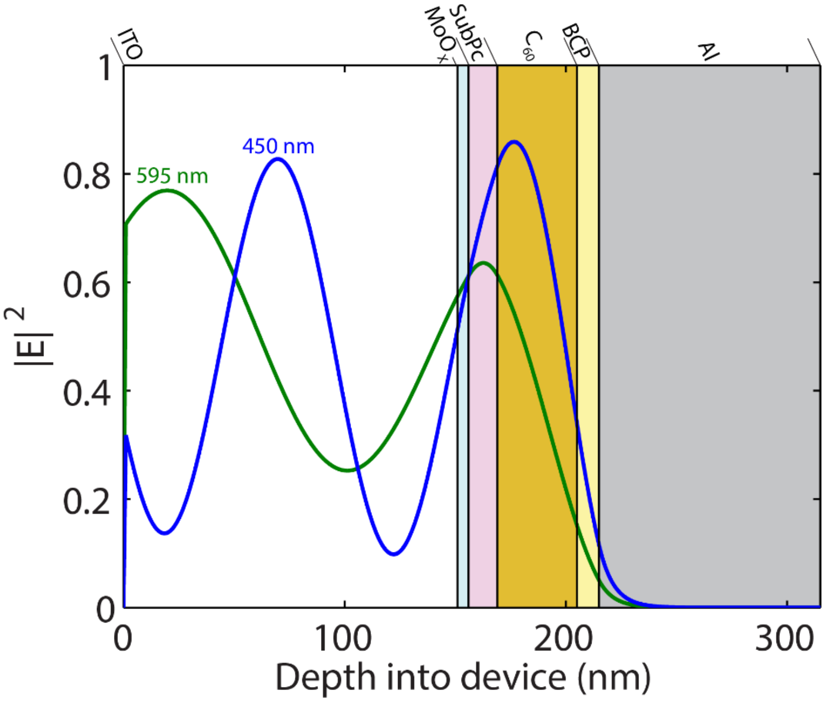

Figure 2-5 Calculated optical electric field in the example device stack for 450 nm (blue) and 595 nm (green) wavelengths. Note that the electric field goes to zero within the reflective metal film.

Shown in **Figure 2-6**, the time-averaged absorbed power, Q, is directly proportional to $|E|^2$ at any wavelength, through Eq. (2-5),

$$Q_j(z) = \frac{4\pi k_j n_j}{\lambda n_0 \cos(\theta_0)} \frac{c\epsilon_0}{2} \left|E_j(z)\right|^2, \tag{2-5}$$

where k_j and n_j are the extinction coefficient and refractive index, respectively, of layer j, n_0 is the refractive index of surrounding medium, λ is the wavelength, θ_0 is the angle of incidence, c is the speed of light, and ε_0 is the permittivity of free space. Note that n_j and k_j are wavelength dependent. As expected from the electric field and high extinction coefficient, SubPc and C_{60} absorb strongly at 595 nm and 450 nm, respectively. Importantly, there is non-arbitrary absorption seen in both the ITO layer and Al layer, both of which are largely indiscriminate to wavelength.

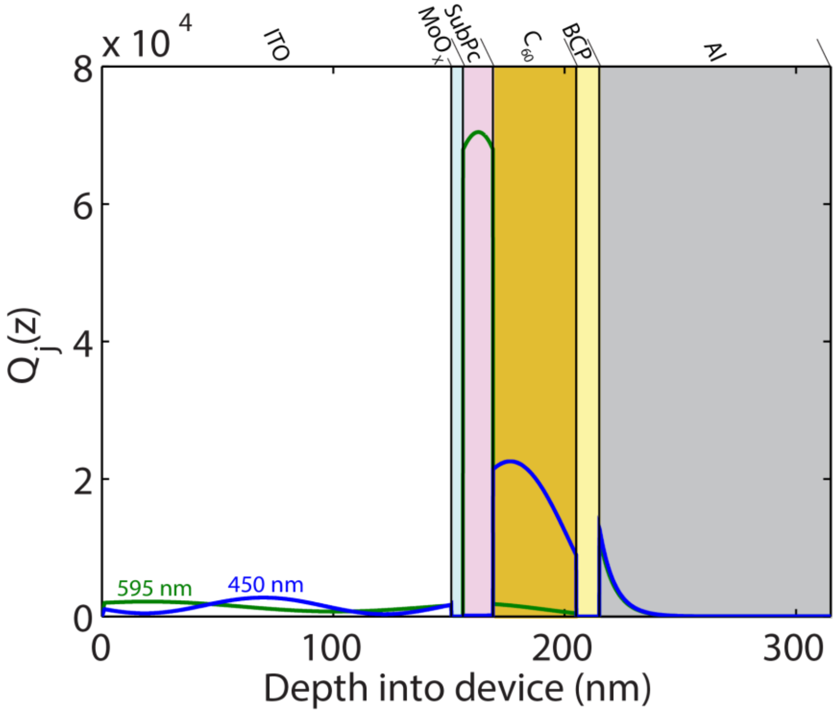

Figure 2-6 Time-averaged absorbed power plotted throughout the depth of the example stack for photons with a wavelength of 450 nm (blue) and 595 nm (green).

2.2.2 Exciton density

Rather than thinking solely in terms of absorbed power and energy, we can consider the exciton state, an electron and hole that are Coulombically bound, usually both on one molecule (i.e. Frenkel exciton), as opposed to being more delocalized (i.e. Wannier-Mott exciton) like those found in inorganic PVs. Calculation of exciton generation rate, $G_j(z)$, where z is depth into the stack, is straightforward, having been calculated from the time-absorbed power at any wavelength through Eq. (2-6), where h is Planck's constant. The exciton generation rate normalized to the peak exciton generation rate is shown in **Figure 2-7**.

$$G_j(z) = \frac{\lambda}{hc} Q_j(z), \tag{2-6}$$

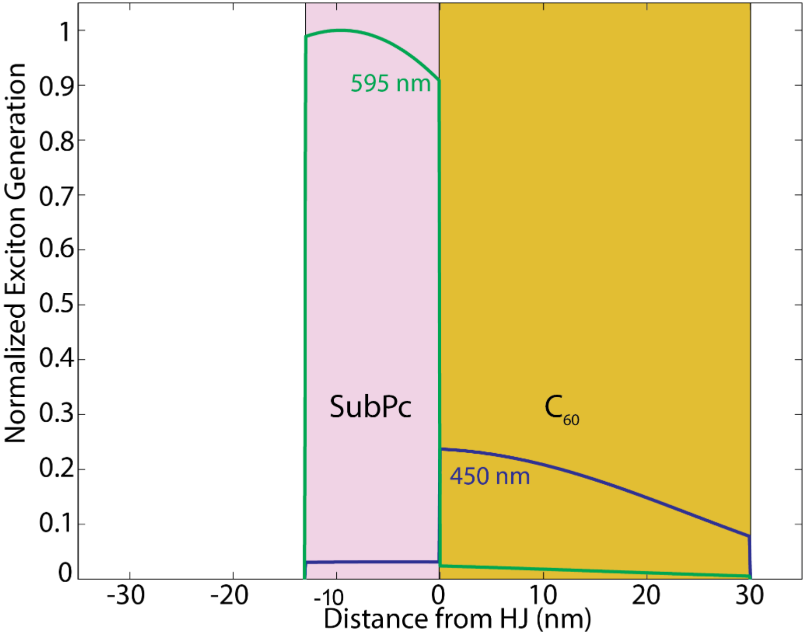

Figure 2-7 Calculated exciton generation rate within the example stack's SubPc and C_{60} films. Peak absorption is at 595 nm for SubPc (green) and 450 nm for C_{60} (blue). The results are normalized to the peak exciton generation rate.

After calculating the exciton generation rate, a one dimensional diffusion model is used to calculate the flux of excitons reaching the heterojunction. Excitons have no net charge, and will diffuse through a film via thermally activated "hopping" mechanism (i.e. Dexter transfer), as well as near-field resonant energy transmission (i.e. Förster transfer).

$$\frac{dp_{ex}}{dt} = \frac{L_{D,j}^2}{\tau_j}\frac{\delta^2 p_{ex}}{\delta z^2} - \frac{p_{ex}}{\tau_j} + G_j = 0, \tag{2-7}$$

Where p_{ex} is the exciton concentration, $L_{D,j}$ and τ_j are the exciton diffusion length and lifetime, respectively, of film j, thus making p_{ex}/τ_j the rate of exciton relaxation. Note that L_D^2/τ is the exciton diffusivity. As the diffusion time approaches the characteristic exciton lifetime for film j, τ_j (typically measured in nanoseconds), the probability of thermalization increases for excitons in the bulk of the film. However, excitons may also interact with adjacent films that have relatively different energy levels to either reflect, quench, or dissociate at the interface; (we here neglect the process of energy transfer by Dexter or Forster mechanisms into another film, as this is already accounted to some extent by the effective exciton lifetime and diffusivity, and to a large extent could be neglected in the material system in question). The exciton profile following diffusion is shown in **Figure 2-8**. Note the significant loss in exciton density when the SubPc interface at -13 nm is quenching rather than reflecting, and the subsequent reduction in J_X.

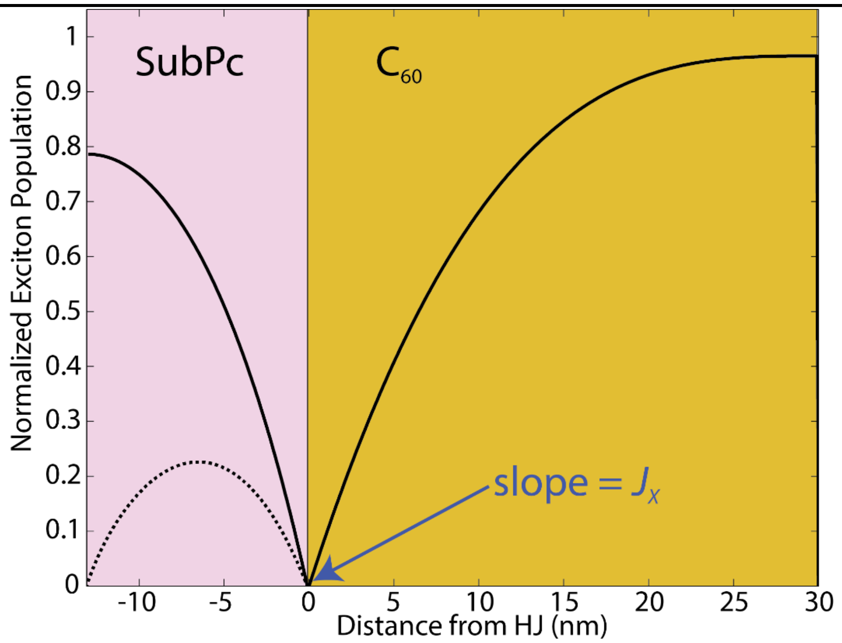

Figure 2-8 Example of one-dimensional steady-state exciton population profiles for the SubPc and C_{60} films in the example stack, normalized to the maximum exciton population. The interface to the left of SubPc either reflects (solid line) or quenches (dotted line) excitons.

Ideally, every interface would be one that dissociates excitons, however, the nature of a metal contact does not allow this. Quenching is a parasitic recombination pathway usually associated with non-radiative recombination of excitons, typically at a metal contact where an exciton may transfer into the valence and conduction bands, followed by thermal recombination. Alternatively, excitons can be confined on a site with a smaller band gap, and quench rapidly, depending on the exciton lifetime of that trap. Quenching can be a significant loss mechanism in OPVs, thus attempts at mitigating quenching interfaces led to creation of exciton blocking layers (EBL) by Peumans et al. [8].

EBLs employ molecules that have a higher HOMO and lower LUMO than the adjacent active layer, effectively creating a wide band gap interface that prevents excitons from transferring into the EBL, thus reflecting excitons rather than allowing them to encounter a quenching interface. Transfer of charge carriers through the EBL occurs through defect states induced by hot electrode deposition [9], however, alignment of the EBL LUMO to that of the active layer LUMO allows for unhindered electron extraction from the acceptor, which leads to an optimal FF [10].

Having identified the possible boundary conditions at any interfaces, the steady-state exciton population can be calculated using the Feng-Ghosh model [5]. It should be noted that any interface may have a combination of these three behaviors (e.g. partially reflecting and partially quenching), though these cases will not be considered further in this work. Calculation of the exciton flux reaching the interface at each wavelength is done via Eq. (2-8),

$$J_{X,j} = q\frac{L_{D,j}^2}{\tau_j}\left|\frac{\delta p_{ex}}{\delta z}\right|_{z=0}. \tag{2-8}$$

Finally, two assumptions allow calculation of the EQE: (i) at short-circuit conditions, the photocurrent is saturated, thus $\eta_D \sim 1$, an assumption that will become more clear in the following sections, and (ii) the short, non-tortuous path to the electrode, assisted by a strong build-in field, allows for the assumption that $\eta_{CC} \sim 1$. Calculation of the EQE for this type of stack is then straightforward. Additionally, internal quantum efficiency (IQE) is the ratio of collected charges to photo-generated excitons, which is the exciton diffusion efficiency in this case. The results are shown in **Figure 2-9**, including the individual contributions of each active layer to the total EQE. This is different from PCE in that it is the efficiency of photon to charge conversion - the aggregate efficiency of the four energy conversion steps, and thus independent of light intensity. The ability to look at individual contributions of each layer to the EQE makes this a powerful tool for stack optimization, especially because direct comparisons are experimentally extremely difficult, if possible at all.

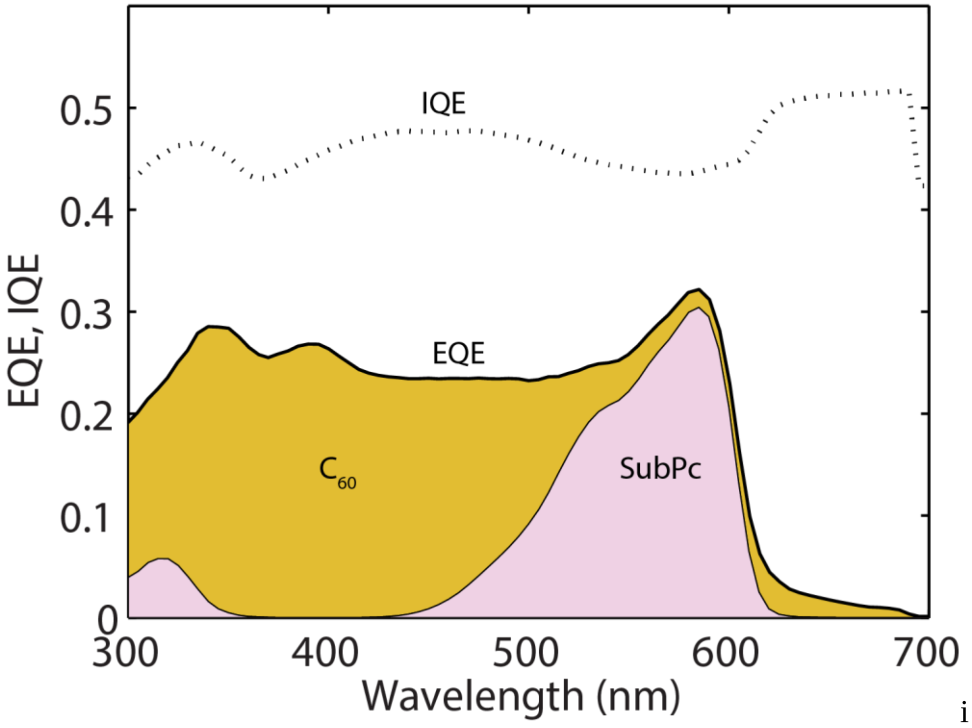

Figure 2-9 Calculate EQE (solid line) and IQE (dotted line) for the example stack. Convolution with the solar spectrum gives a current density of 4.21 mA/cm^2.

2.3 Origin of V_{OC}

The conditions necessary for V_{OC} occur when the forward current, originating from carrier injection into the organics from the electrodes, exactly balances the reverse current, originating from dissociation of excitons. Under this condition, all generated charge carriers must recombine, which ideally occurs at the heterojunction, but can also occur in the bulk (i.e. Langevin recombination) or at electrode interfaces. A simple way of measuring this recombination is to perform a JV sweep when the device is not illuminated to measure the "dark current". In an ideal device, all injected charge carriers will undergo bimolecular recombination at the heterojunction, thus making the dark current a measure of recombination current at the interface. Intuitively, reducing the recombination rate of charge carriers will allow the charge carrier concentration to grow higher until recombination has matched that of generation. Thus, V_{OC} has an inverse relationship to the recombination rate and dark current. On a microscopic level, the morphology of the interface, including molecular structure and orientation, which will be addressed in 2.4.1, will affect recombination, so understanding this relationship is essential to understanding V_{OC}.

The Shockley equation relates the current and voltage of an ideal diode through Eq. (2-9),

$$J = J_S \left[\exp\left(\frac{q(V - JR_S)}{nk_BT}\right) - 1\right] - J_{ph}(V), \tag{2-9}$$

where J_S is the saturation current density, n is the diode ideality factor, R_S is the series resistance, and J_{ph} is the bias-dependent photocurrent density. By setting $J = 0$ for the open circuit condition, we arrive at Eq. (2-10) for the V_{OC}. This requires two assumptions: first, that the exponential term in brackets is much larger than 1; and secondly, that the photocurrent is both constant and equal to J_{SC} for all biases up to V_{OC}.

$$qV_{OC} = nk_BT\ln\left(\frac{J_{SC}}{J_S}\right) \tag{2-10}$$

This is effectively the difference in generation rate and recombination rate, and gives the important result of V_{OC} changing logarithmically with J_{SC}. Measurement of J_S proceeds simply through fitting the model to the measured dark JV sweep.

2.3.1 Morphology considerations

The relationship between J_S and V_{OC} in Eq. (2-10) has been established for OPVs by Perez et al. [11], who suggested that donors with high disorder and steric hindrance have a significantly lower J_S, and thus higher V_{OC}. Indeed, disorder at the heterojunction, induced by deposition or post-processing, has been shown to increase V_{OC} over that of a more ordered heterojunction [12]. This has been attributed to the degree of overlap of electronic wave functions between the donor and acceptor. Less overlap provides less of an opportunity for an electron or hole to hop or tunnel to the other carrier, thus providing a low recombination rate. This leads to consideration of the polaron pair state's role in mediating dissociation, recombination, and general JV characteristics in an OPV device.

2.3.2 Polaron pairs

Though we have previously referred to exciton dissociation as the step preceding carrier collection, it can be expanded into two steps: (i) charge transfer from one excited molecule to a polaron pair state, and (ii) dissociation or recombination of the polaron pair, followed by carrier collection, as shown in **Figure 2-10**. This being the case, dissociation efficiency is simply the product of charge transfer efficiency, η_{CT}, and polaron pair dissociation efficiency, η_{PPd}.

At the electron donor-acceptor interface, polarons are generated by an exciton overcoming its binding energy and undergoing charge transfer at the heterojunction, where it's energetically favorable for an electron (hole) to leave the donor LUMO (acceptor HOMO) for an adjacent acceptor's LUMO (donor's HOMO). This geminate polaron pair is Coulombically bound, and must undergo dissociation to free polaron pairs, or otherwise recombine to the ground state. Considering that these are geminate polaron pairs, the process of bimolecular recombination does not apply, thus recombination occur through a first-order decay rate, with a recombination time that is independent of polaron pair concentration, typically on the order of 100 ns. In general, the recombination process will depend on the difference between the energy of the polaron pair state, and the ground state, as well as the overlap in corresponding wave functions, as mentioned previously.

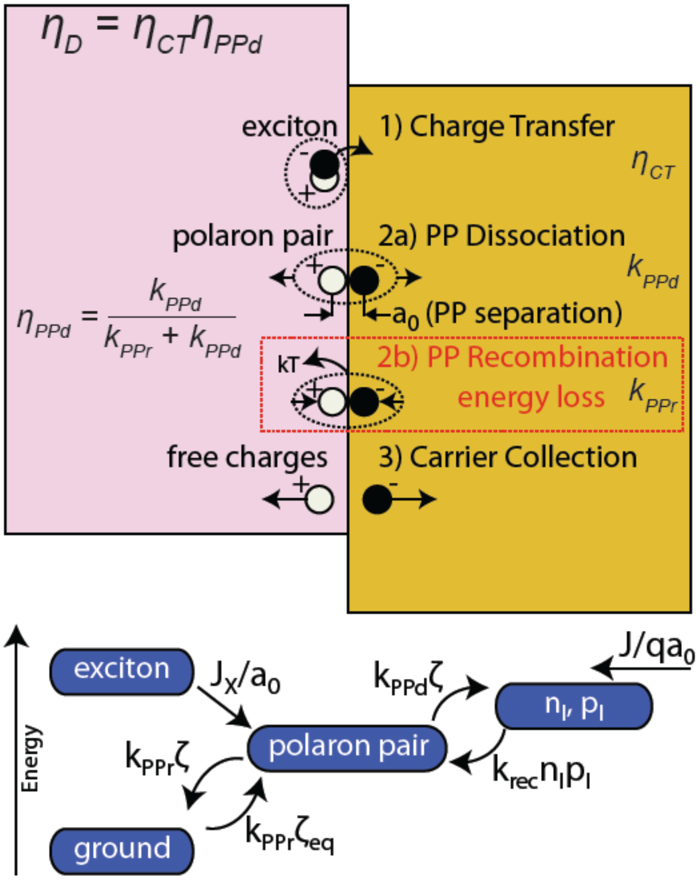

Figure 2-10 Diagram of theorized polaron pair recombination at organic heterojunctions. The top illustration represents physical space whereas the bottom represents energy space.

The exciton dissociation time scale is much shorter than that of polaron pair recombination, ~1 ns when assisted by the high electric field, which is typically ~10^7 V/m.

This process has been well modeled macroscopically through the Onsager-Braun relation [13], for which the dissociation rate of pair of oppositely charged molecules is presented in Eq. (2-11),

$$k_f = \frac{\langle\mu\rangle e}{\langle\epsilon_r\rangle\epsilon_0}\frac{3}{4\pi r_{PP}^3}\exp\left(-\frac{E_{PP}}{k_b T}\right)\left[1 + b + \frac{b^2}{3} + \frac{b^3}{18} + \cdots\right]. \tag{2-11}$$

This relies on the polaron pair separation distance, r_{PP}, binding energy, E_{PP}, and external electric field (i.e. the sum of the built-in field and external bias applied to the device), which is kept in Onsager's term, $b = e^2 F_I / 8\pi\langle\epsilon_r\rangle\epsilon_0 k_b^2 T^2$. The first term of Eq. (2-11) is derived from Langevin recombination; the second term is a Boltzmann term describing the efficiency of polaron pair separation in the absence of an electric field; and the third term is the Taylor expansion of a first order Bessel function, empirically derived by Onsager [4, 14]. Generally, E_{PP} is assumed to follow Coulomb's law,

$$E_{PP} = \frac{1}{4\pi\langle\epsilon_r\rangle\epsilon_0}\frac{q^2}{r_{PP}}. \tag{2-12}$$

For a separation distance of 1 nm, and a typical relative dielectric constant between 3 and 4, E_{PP} = 0.36-0.48 eV, which will not be dissociated by thermal energy alone. Alternative formulations of the Onsager-Braun relation have been used for materials with high mobility [15].

2.4 OPV Diode Model

Though the Shockley model presented in Eq. (2-9) works reasonably well, it does a poor job reproducing low-temperature behavior and the occasionally observed S-kink behavior in certain types of OPVs. An OPV-specific diode model was proposed by Giebink et al., derived from a mole balance on excitons, polaron pairs, and charge carriers. This resulted in an equation similar to the Shockley equation, but with individual contributions from each active organic layer, as well as a form more explicitly linked to energy levels and structure.

$$J = J_{sD}\left[\exp\left(\frac{qV}{n_D k_B T}\right) - \frac{k_{PPd}}{k_{PPd,eq}}\right] + J_{sA}\left[\exp\left(\frac{qV}{n_A k_B T}\right) - \frac{k_{PPd}}{k_{PPd,eq}}\right] - q\eta_{PPd}J_X, \quad (2\text{-}13)$$

Here, J_{sD} and J_{sA} are now the trap-dependent saturation current densities in the donor and acceptor, respectively. Analogous to the Shockley equation, n_D and n_A are the ideality factors, mostly related to the trap distribution and depth, for the donor and acceptor, respectively. The saturation currents can be further explained as being directly proportional to the product of the Langevin recombination rate, k_{rec}, LUMO density of states, N_{LUMO}, and trapped hole density in the donor, H_D, as described in Eq. (2-14) and the analogous for J_{sA} for the acceptor, Eq. (2-15). α is the effective energy offset, after accounting for losses from trapped charges and the steady-state charge profile in the organics; it is more explicitly defined in reference [16].

$$J_{sD} = q a_0 (1 - \eta_{PPd}) k_{rec,n} N_{LUMO} H_D \exp\left(-\frac{\alpha_D}{k_B T}\right) \quad (2\text{-}14)$$

$$J_{sA} = q a_0 (1 - \eta_{PPd}) k_{rec,p} N_{HOMO} H_A \exp\left(-\frac{\alpha_A}{k_B T}\right) \quad (2\text{-}15)$$

The photocurrent is now expressed as the product of the polaron pair dissociation efficiency and exciton flux reaching the heterojunction. Occasionally, J_x is assumed equivalent to J_{SC}, but it is more often used as a fitting parameter. However, η_{PPd} is now related to k_{PPd} and k_{PPr} through Eq.(2-16),

$$\eta_{PPd} = \frac{k_{PPd}}{k_{PPd} + k_{PPr}}. \tag{2-16}$$

Here, k_{PPd} is assumed to be the Onsager-Braun dissociation rate constant, k_f, Eq. (2-12). This makes k_{PPd} a function of the internal electric field at the heterojunction, F_I, which is often assumed to be linear across the device stack because of the low charge carrier concentrations during operation,

$$F_I = \frac{V_a - V_{bi}}{d}, \tag{2-17}$$

However, certain stacks with charge transport barriers, Fermi level pinning, surface dipoles, and non-Ohmic contacts may require solving the electrostatics of the system explicitly via the Poisson equation, a Ricatti equation, or using a discrete numerical solver.

2.4.1 Unique additions

Unique to the model used in this work is that nearly all variables were either empirically measured or taken from literature. Additionally, the EQE model and JV model are linked, whereas the exciton flux reaching the interface is usually considered a fit parameter for the JV model. Thus, this model represents a step forward in creating a complete predictive device model, with the potential for determining material parameters *ab initio*, opening the potential for rapid combinatorial studies *in silico*. This includes the complex refractive index, exciton lifetime and diffusion length, dielectric constant, electron and hole mobility, electronic energy levels, film thicknesses, and photoconductivity. Polaron pair separation distances are not assumed, as done in previous works, but calculated *in silico*, thanks to collaborator, Hossein Hashemi. This does not preclude assumptions inherent in the model, namely that the device performance is dominated by polaron dissociation and recombination.

Note that we consider r_{PP} a physical separation distance, whereas it is common to consider it a thermalization radius, a_0, instead. Thus, we are using it as a physical attribute of the system, rather than a fit parameter in the model more directly related to the initial separation seen in a hot CT state, than the thermalized polaron pair. This is an important distinction between the model used in this thesis and more common formulations, and is a result of our assumption that the dissociation process proceeds via a reorganized polaron pair state, rather than a hot one, where the excess energy between the exciton and polaron pair is important for dissociation. An immediately obvious consequence of using r_{PP} is that it is dependent on the orientation of the SubPc molecule with respect to C_{60}, as visualized in **Figure 2-11**.

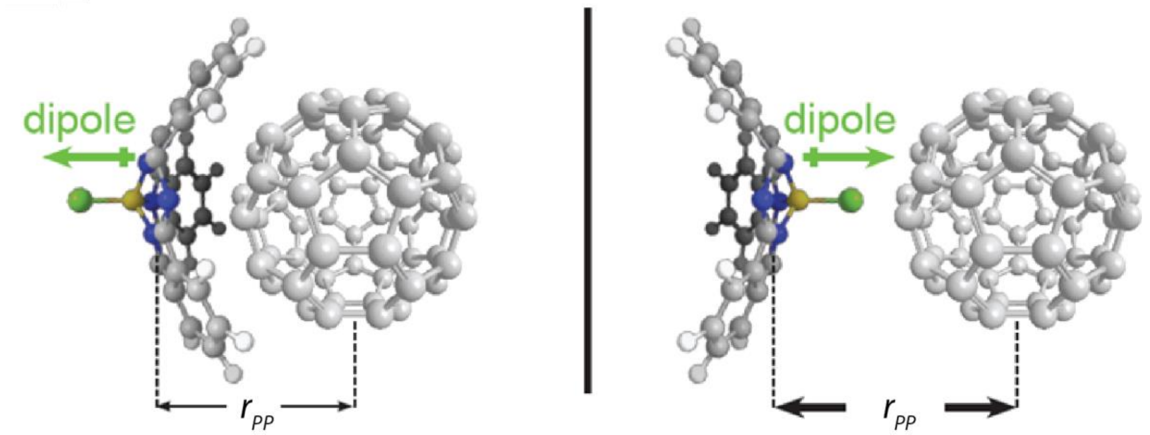

Figure 2-11 Diagrams depicting two possible configurations when a polaron pair is formed between SubPc and C_{60}. Note the separation distance of the charge centers is r_{PP}, and the dipole changes direction with the molecule, potentially assisting or hindering charge transfer and polaron pair dissociation.

Multiple authors have investigated the role of static and dynamic phenomena that lower the exciton binding energy, as this makes dissociation more probable and possibly explains both the low temperature photocurrent and weak dependence of dissociation on the electric field. These have been explained by bulk exciton dissociation [17], permanent dipoles or quadrupoles [18, 19], entropy effects [20], relaxation in energetically disordered states [21], and rapid dissociation of the hot CT state before relaxation to a polaron pair [4]. The energy of each state is shown in **Figure 2-12**, along with an inset that shows the polaron pair binding energy versus separation, and the predicted lowering of this energy when including the aforementioned dipoles and disorder.

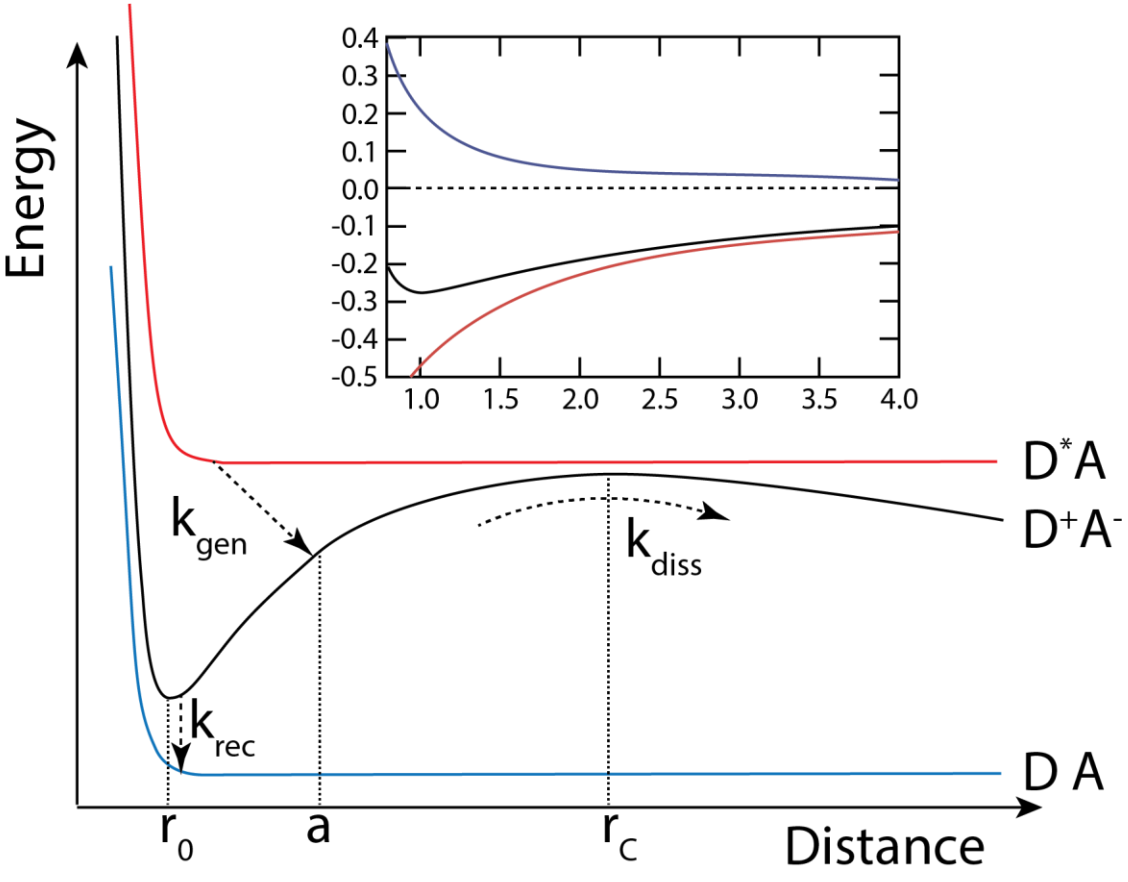

Figure 2-12 Energy diagram versus separation distance of an exciton (red), polaron pair (black), and the ground state (blue). The inset shows the coulomb binding potential (red), and the expected change (black) as a result sum of interface multipoles, dark dipoles, and entropy effects (blue line). Adapted from [4], with permission from John Wiley and Sons

As the V_{OC} is a function of balanced recombination and dissociation of polaron pairs, increasing the V_{OC} is a matter of decreasing the dark current density through decreasing the wave function coupling between the two geminate polarons at the interface. Unfortunately, steric hindrance and larger separation distances will likely result in poor charge and exciton transport in the bulk of the film, thus causing a tradeoff between voltage and current. A possible way of overcoming this is to have a layer that's highly ordered in the bulk of the film, but induce disorder at the interface, but this may result in transport gap broadening as a result of the disorder. Effectively, this will make excitons approaching the heterojunction more likely to reflect off the interface or back-diffuse, rather than increase in energy along with the broadened transport gap.

2.5 Advantages and Limitations

The more complexity that is introduced into a model, the more powerful it becomes, but also more likely that it is specialized, thus only being appropriate for a narrow range of conditions. In the case of this model, the advantages are profound, and arise from the fact that most of the parameters entered into the model are independently measurable material parameters, except for k_{PPr}, k_{PPd}, and r_{PP}. Additionally, the trap density and depth require very careful processing and handling to remain constant between batches. With the most advanced *ab initio* calculations of microscopic structure (i.e. polaron pair structure), and additional calculation of the rate constants, it may be possible to successfully predict a JV curve entirely *in silico*.

Utilizing the Onsager-Braun relation is useful in being able to reproduce the S-kink behavior seen in organic photovoltaics, since it allows the photocurrent density to approach zero prior to the JV curve being dominated by recombination current density. However, Braun suggested that the binding energy is not always Coulombic, and fails for many organic ion pairs [13]. We use DFT to calculate contributions from both Coulombic and local molecular dipole contributions in Chapter 4, which allows us to better match the JV curve of the two organic devices without relying on additional fitting parameters. Additionally, the electric field in a dipole that assists dissociation is able to reduce the electric field dependence of the Onsager-Braun relation by significantly reducing the polaron pair binding energy. This alleviates the discrepancy between that has been noticed between Monte Carlo models and macroscopic, Onsager-Braun based models like the one used in this work [22].

Additionally, both the Onsager-Braun relation and bulk polaron recombination mechanisms are related to the Langevin bimolecular recombination rate, though Langevin recombination is a gross assumption for organic semiconductors, considering the low charge screening, local energy from environment distortion (i.e. polaron state), and hopping mechanism in organic semiconductors. All of these increase the difficulty of two oppositely charged polarons encountering one another. On top of this is the assumption of an averaged permittivity across polaron pairs, geminate or not, which may not be true, considering the local environment of a polaron pair is very different from that in the bulk of the film.

Knowledge of the microscopic structure is paramount for the model used here, but mapping the distribution of polaron pairs at a heterojunction, or even measuring the geometry of some polaron pairs, has been very difficult and elusive. Without a known polaron pair distribution or geometry, we used DFT calculations to predict the structures, though prediction of a distribution or generalized room temperature morphology is currently out of the realm of computational prowess. Possibly, advancements in atomic force microscopy and synchrotron X-ray diffraction analysis could lead to the ability to determine the polaron pair geometry, though the mechanism of polaron pair charge transfer and dissociation are still under debate. Disorder at the interface could be responsible for broad energy states that allow for entropy to drive the hopping mechanism away from the interface – with each jump ending at a lower energy in the distribution of states [23-25]. Similarly, and of particular interest at the moment, is the capability of a hot charge transfer state to dissociate, and even be collected at the electrode, prior to relaxing into a lower energy state after having dissipated the energy gained during charge transfer.

Apart from the assumptions regarding recombination and dissociation mechanisms at the interface, the assumptions regarding charge transfer from an exciton to a polaron pair is assumed to have relatively low back-transfer (i.e. low reverse rate constant) or low polaron pair population. In most cases, this assumption is valid, and allows for decoupling the exciton flux calculation from the JV calculation. However, a sufficiently high polaron pair population or a very low LUMO-LUMO or HOMO-HOMO energy separation can cause significant generation of excitons from polaron pairs. This would then require a simultaneously solution of the exciton concentration in the active layers with the polaron pair and free carrier density, thus becoming much more complex. This is not important yet, but will become important when charge transfer rates are being engineered alongside polaron pair dissociation and recombination rates.

2.6 Towards complete characterization

A combination of the modeling methods described above allows for independent calculation of losses from reflection, parasitic absorption, exciton relaxation, and polaron pair recombination, as is seen in **Figure 2-13**. Of interest is the red band associated with recombination in the JV model, which varies with applied bias. With no applied bias, this band will be negligibly thin; however, the band will increase with the applied bias, as a result of lowering k_{PPd} and thus shifting polaron pairs towards recombination rather than dissociation.

The utility of modeling is evident in the potency of such a visual aid. Upon a single glance, it become readily apparent where the greatest urgency resides for improving device current. The three greatest losses of power are from reflected photons, parasitic absorption in ITO, and excessive exciton thermalization. For more detailed discussion and methods for overcoming these losses, addition of a third (or more) active layer can absorb an additional section of the visible spectrum and form a second heterojunctions, creating a cascade structure [26]. This reduces the effective distance required for excitons to reach the heterojunction, thereby reducing much of the thermalization loss in the bulk.

Finally, the complete characterization of a device with regards to absorption, exciton density, exciton flux at the heterojunction, and isolation of the diode behavior under illumination becomes possible. This will be discussed in the remaining chapters.

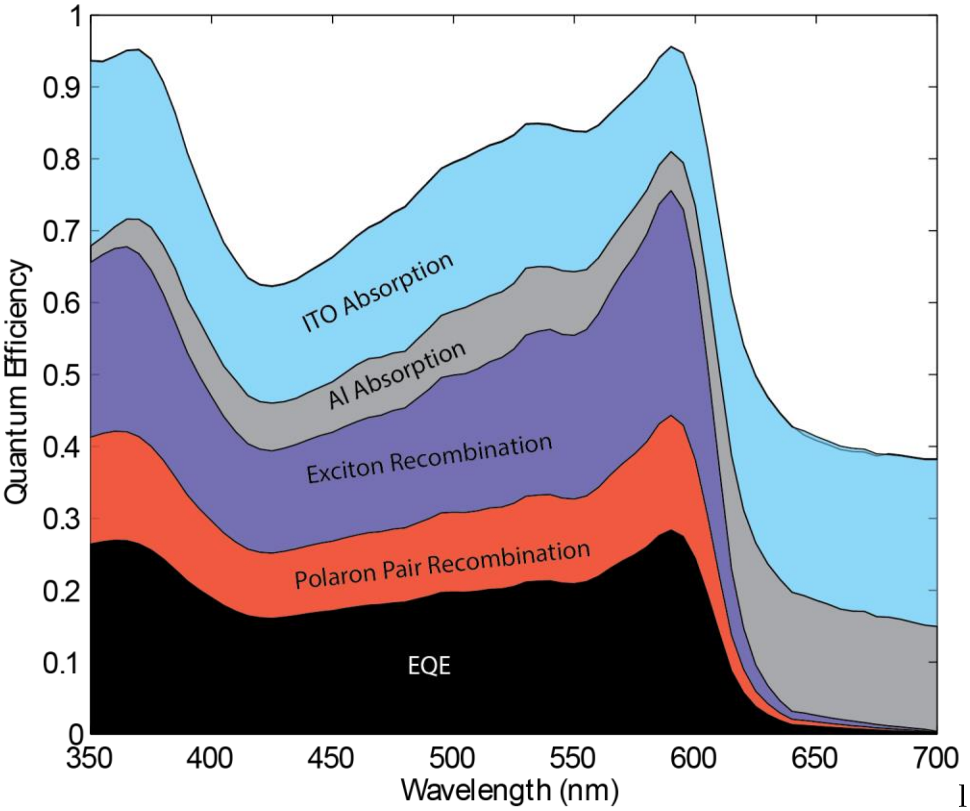

Figure 2-13 Diagram of dominant loss mechanisms in the example SubPc/C_{60}. This is at the maximum power point, whereas the red section would be nonexistent for J_{SC} and encompass nearly the entire black section at V_{OC}.

2.7 References

[1] C.W. Tang, S.A. VanSlyke, Organic electroluminescent diodes, Applied Physics Letters, 51 (1987) 913-915.

[2] W. Shockley, H.J. Queisser, Detailed Balance Limit of Efficiency of p-n Junction Solar Cells, Journal of Applied Physics, 32 (1961) 510-519.

[3] U. Rau, U.W. Paetzold, T. Kirchartz, Thermodynamics of light management in photovoltaic devices, Physical Review B, 90 (2014) 035211.

[4] C. Deibel, T. Strobel, V. Dyakonov, Role of the Charge Transfer State in Organic Donor–Acceptor Solar Cells, Advanced Materials, 22 (2010) 4097-4111.

[5] L.A.A. Pettersson, L.S. Roman, O. Inganäs, Modeling photocurrent action spectra of photovoltaic devices based on organic thin films, Journal of Applied Physics, 86 (1999) 487.

[6] G.F. Burkhard, E.T. Hoke, M.D. McGehee, Accounting for Interference, Scattering, and Electrode Absorption to Make Accurate Internal Quantum Efficiency Measurements in Organic and Other Thin Solar Cells, Advanced Materials, 22 (2010) 3293-3297.

[7] B.T. O'Connor, Organic Electronics on Fibers for Energy Conversion Applications, Mechanical Engineering, University of Michigan, Ann Arbor, MI, 2009, pp. 161.

[8] P. Peumans, V. Bulović, S.R. Forrest, Efficient photon harvesting at high optical intensities in ultrathin organic double-heterostructure photovoltaic diodes, Applied Physics Letters, 76 (2000) 2650-2652.

[9] T. Sakurai, S. Toyoshima, H. Kitazume, S. Masuda, H. Kato, K. Akimoto, Influence of gap states on electrical properties at interface between bathocuproine and various types of metals, Journal of Applied Physics, 107 (2010) -.

[10] B.E. Lassiter, G. Wei, S. Wang, J.D. Zimmerman, V.V. Diev, M.E. Thompson, S.R. Forrest, Organic photovoltaics incorporating electron conducting exciton blocking layers, Applied Physics Letters, 98 (2011) 243307.

[11] M.D. Perez, C. Borek, S.R. Forrest, M.E. Thompson, Molecular and Morphological Influences on the Open Circuit Voltages of Organic Photovoltaic Devices, Journal of the American Chemical Society, 131 (2009) 9281-9286.

[12] J.D. Zimmerman, X. Xiao, C.K. Renshaw, S. Wang, V.V. Diev, M.E. Thompson, S.R. Forrest, Independent Control of Bulk and Interfacial Morphologies of Small Molecular Weight Organic Heterojunction Solar Cells, Nano letters, 12 (2012) 4366-4371.

[13] C.L. Braun, Electric field assisted dissociation of charge transfer states as a mechanism of photocarrier production, The Journal of Chemical Physics, 80 (1984) 4157.

[14] L. Onsager, Deviations from Ohm's Law in Weak Electrolytes, The Journal of Chemical Physics, 2 (1934) 599.

[15] M. Tachiya, Breakdown of the Onsager theory of geminate ion recombination, The Journal of Chemical Physics, 89 (1988) 6929-6935.

[16] N.C. Giebink, G.P. Wiederrecht, M.R. Wasielewski, S.R. Forrest, Ideal diode equation for organic heterojunctions. I. Derivation and application, Physical Review B, 82 (2010) 155305.

[17] C.K. Renshaw, J.D. Zimmerman, B.E. Lassiter, S.R. Forrest, Photoconductivity in donor-acceptor heterojunction organic photovoltaics, Physical Review B, 86 (2012) 085324.

[18] S. Verlaak, P. Heremans, Molecular microelectrostatic view on electronic states near pentacene grain boundaries, Physical Review B, 75 (2007) 115127.

[19] W. Osikowicz, M.P. de Jong, W.R. Salaneck, Formation of the Interfacial Dipole at Organic-Organic Interfaces: C60/Polymer Interfaces, Advanced Materials, 19 (2007) 4213-4217.

[20] T.M. Clarke, J.R. Durrant, Charge Photogeneration in Organic Solar Cells, Chemical Reviews, 110 (2010) 6736-6767.

[21] H. Bässler, Charge Transport in Disordered Organic Photoconductors a Monte Carlo Simulation Study, physica status solidi (b), 175 (1993) 15-56.

[22] M. Wojcik, M. Tachiya, Accuracies of the empirical theories of the escape probability based on Eigen model and Braun model compared with the exact extension of Onsager theory, The Journal of Chemical Physics, 130 (2009) -.

[23] S. Gélinas, A. Rao, A. Kumar, S.L. Smith, A.W. Chin, J. Clark, T.S. van der Poll, G.C. Bazan, R.H. Friend, Ultrafast Long-Range Charge Separation in Organic Semiconductor Photovoltaic Diodes, Science, 343 (2014) 512-516.

[24] P.K. Nayak, K.L. Narasimhan, D. Cahen, Separating Charges at Organic Interfaces: Effects of Disorder, Hot States, and Electric Field, The Journal of Physical Chemistry Letters, 4 (2013) 1707-1717.

[25] J.C. Blakesley, D. Neher, Relationship between energetic disorder and open-circuit voltage in bulk heterojunction organic solar cells, Physical Review B, 84 (2011) 075210.

[26] A. Barito, M.E. Sykes, D. Bilby, J. Amonoo, Y. Jin, S.E. Morris, P.F. Green, J. Kim, M. Shtein, Recovering lost excitons in organic photovoltaics using a transparent dissociation layer, Journal of Applied Physics, 113 (2013) 203110.

CHAPTER 3

INVERTED OPVs

Experimentally measuring the geometry of polaron pair orientations is difficult, especially considering that the heterojunction is a buried interface likely to be destroyed upon most probing attempts. In this chapter, inverted OPVs (iOPV) are made alongside conventional architectures (cOPV), with a goal of isolating the heterojunction behavior in each device. Large sections of this chapter are derived from the paper “High efficiency organic photovoltaic cells based on inverted SubPc/C_{60}/ITO cascade junctions”, accepted for publication in Organic Electronics (2014), DOIL 10.1016/j.orgel.2014.08.046.

3.1 Inverted OPVs

Conventional organic solar cells rely on glass or plastic substrates pre-coated with indium tin oxide (ITO) or similar high work function transparent conductors, in part due to the combination of greater stability of high work function surfaces against oxidation, and in part due to the wide commercial availability of such substrates. In these structures, ITO (or analogous material) functions as an anode, where holes are extracted from the adjacent electron donor layer. Nevertheless, numerous publications show interest in inverted organic solar cell structures [1-3], in which the organic layer deposition sequence is switched to allow *electron* injection into the substrate. These structures offer advantages in some applications, including greater latitude in optical design [4-6], tandem cell integration [1, 6-9], and simplified deposition methods [10].

Previous work using inverted photovoltaic devices has yielded a variety of results. Placement of the low work function cathode away from ambient oxygen, and removal of bathocuproine (BCP), increases device lifetime dramatically [11, 12]. However, small molecular OPV cells typically exhibit a decrease in the open circuit voltage (V_{OC}), as well as short circuit current density (J_{SC}), lowering the power conversion efficiency relative to conventional (non-inverted) OPVs [2, 5, 13]. This is often explained through inverted devices offering a smaller offset between the work functions of the anode and cathode, thus providing a smaller built-in potential for polaron pair dissociation. Some work has expanded the limited number of materials available for electron and hole extraction that can maintain the high built-in potential necessary to achieve performance comparable to conventional architectures [4, 7, 11, 14-17]. Here we fully characterize both a cOPV and iOPV for the purpose of isolating the electrical behavior of the heterojunction. Ultimately, this results in the demonstration of an inverted device with an efficiency surpassing its conventional architecture counterpart.

3.2 OPV design for matched exciton flux

Device structures used in this study comprise organic absorber layers sandwiched between the ITO and 100 nm thick aluminum electrodes, with buffer layers inserted between the absorbers and electrodes to modify the electrode work function and prevent parasitic exciton quenching. cOPV devices, shown in **Figure 3-1**a, have the donor buffer layer and donor organic deposited first, followed by the acceptor organic and acceptor buffer layer prior to capping. iOPV devices, shown in **Figure 3-1**b, are defined as devices where the deposition order has been inverted, with the acceptor buffer and organic deposited prior to the donor organic and buffer. Molybdenum oxide (MoO_X) is used as an anodic buffer layer for its high work function and ability to reduce dark current [18] in both conventional and inverted devices. The cathode work function is determined by the deposited metal, thus cathode buffer layers are typically exciton-blocking layers (EBL) used to prevent quenching at the organic/metal interface and adjust the optical cavity. Bathocuproine (BCP) was used as an EBL in the conventional device, whereas ITO was used as a buffer layer for inverted devices.

As will be discussed below, the cOPV and iOPV structures in this comparison were at the outset designed to have identical exciton fluxes at the donor-acceptor (SubPc/C_{60}) interface, which should produce identical J_{SC} in each device. Nevertheless, we observe a clear trade-off between the current density and voltage, whose origins reveal surprising conclusions regarding excitonic processes at the organic-inorganic interfaces within the structure, as discussed below.

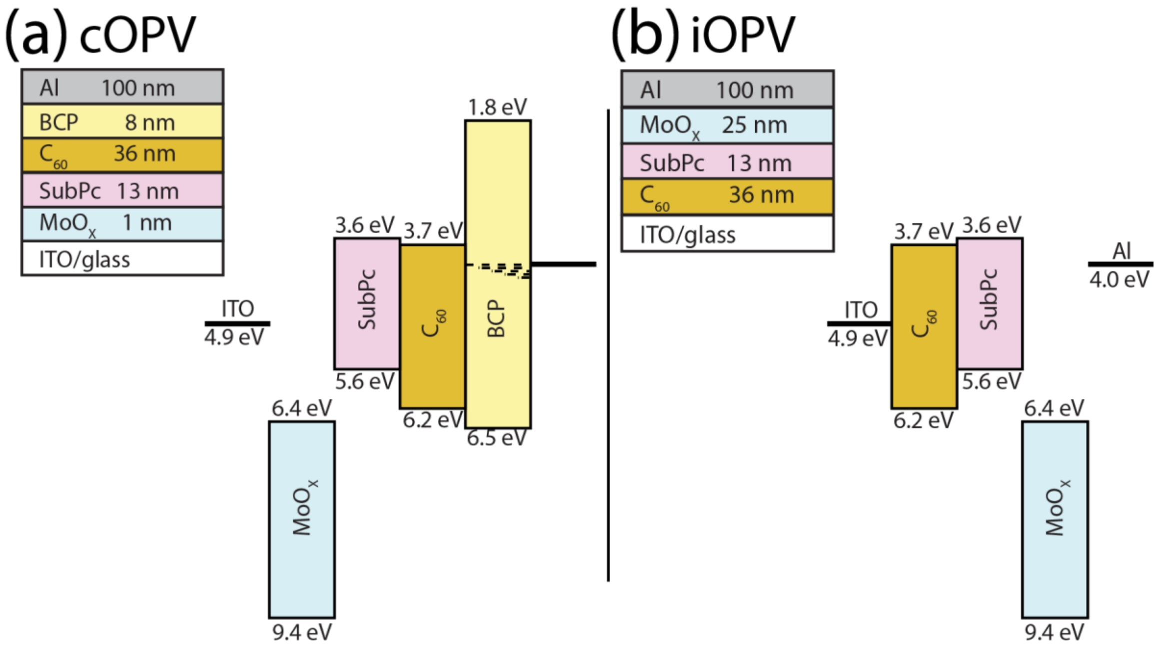

Figure 3-1 Deposition stack and energy level diagram for (a) cOPV and (b) iOPV. Dotted lines in BCP represent defect states for electron transport.

To understand the physical origins of the differences, we first recognize that EQE in OPVs can be expressed as the product of efficiencies corresponding to photon absorption, η_A, exciton diffusion, η_{ED}, exciton dissociation, η_D, and carrier collection, η_{CC}, as expressed in chapter 2:

$$EQE = \eta_A \eta_{ED} \eta_D \eta_{CC}. \tag{2-2}$$

Absorption, diffusion, and carrier collection are bulk properties of films, whereas charge transfer and interfacial polaron pair dissociation, combined to form η_D [19], are properties of the molecules comprising the heterojunction and its local morphology. Using homogeneous, amorphous films in thin bilayer stacks allows us to assume that $\eta_{CC} \sim 1$. The high electric field within the organic layers, moderate illumination intensity (1 Sun at maximum), steady-state operation, and short, non-tortuous path from the heterojunction allow us to neglect bulk recombination of charge carriers.

To optimize and better understand the behavior of the cOPV and iOPV structures, the EQE spectra were calculated for each layer structure according to Section 2.2. Based on photocurrent optimizations, the donor layer and acceptor film thicknesses were held at 13 nm and 36 nm, respectively, while the buffer layer thickness was adjusted until the exciton flux at the donor-acceptor interface was identical between the two stacks. This method of optimizing for a matched exciton flux is in contrast to the typical method of using simulations to optimize J_{SC} for high PCE; it does not necessarily maximize PCE, but allows for a direct probing of the relative influences of interfacial and bulk processes. (As a basis for comparison, conventional devices for optimized J_{SC} yielded PCE = 3% ± 0.2%, with an average $J_{SC} = 4.6 \pm 0.3$ mA/cm^2.) Subsequently, the optical and exciton transport models were used to calculate and match experimentally measured EQE spectra by adjusting the exciton diffusion lengths and exciton interaction (quenching, dissociating, or blocking) through defined boundary conditions at critical interfaces within the devices [20, 21].

3.3 Materials and Methods

Purified organic materials (SubPc, C_{60}, and BCP) were purchased from Lumtec, Inc. and stored in a nitrogen environment prior to deposition. ITO-coated glass substrates were purchased from Delta Technologies and cleaned in a process described elsewhere [20]. ITO substrates for inverted devices (i.e. the cathode) were used immediately after the cleaning process, whereas substrates for conventional devices were intended as the anode, thus placed in an ultraviolet ozone chamber for 10 minutes to maximize the work function [22]. All layers prior to the (reflective) top electrode were deposited sequentially in a sixsource “A-mod” vacuum thermal evaporation system from Angstrom Engineering. High vacuum of 10^{-7} Torr was interrupted once, for the placement of shadow masks, to create the 1 mm diameter top contacts. SubPc was deposited at 0.5 Å/s, C_{60} at 1 Å/s, and BCP at 0.6 Å/s. Devices were immediately electrically characterized in air with a Hewlett Packard HP 4156B semiconductor parameter analyzer while under AM 1.5G illumination at one sun, provided by an Oriel 94166 solar simulator. EQE measurements were taken with a lock-in amplifier under illumination from monochromated halogen source. Absorption measurements were taken in a UV-vis mode Perkin-Elmer Lambda 750 spectrometer, and used to calculate the internal quantum efficiency.

As a standard practice, our thin film deposition apparatus and process are calibrated using very precise spectroscopic ellipsometry, and subsequently perform optical modeling of our device structure. This model accounts for interference and electrode absorption, but eschews scattering effects, because they occur at a wavelength range (i.e. 610-700 nm) where absorption in the organic layers is minimal, with minimal contributions to EQE. The good fit of absorption modeling to measurement shown in **Figure 3-2** indicates that the stack thicknesses are accurate.

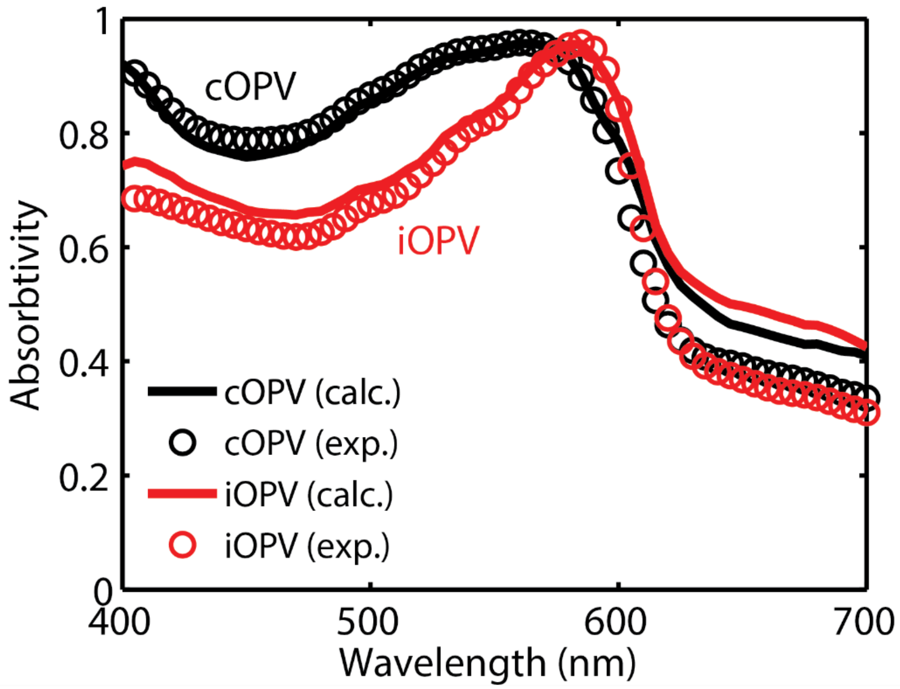

Figure 3-2 Reflectance-mode absorption spectra of cOPV (black) and iOPV (red) devices with a 26 nm SubPc layer. Scattering effects are not included in the optical model, leading to the deviation between the model and measurement at longer wavelengths.

3.4 Voltage-current tradeoff

Although previous work has demonstrated a reduction in J_{SC} for inverted devices [2], our results show that J_{SC} can increase upon deposition order inversion. **Figure 3-3** plots the current density versus voltage characteristics for cOPV and iOPV devices, in which J_{SC} switches from 4.15 mA/cm^2 in cOPV to 5.23 mA/cm^2 in iOPV cells. Despite the associated reduction in V_{OC}, from 1.11 V to 1.02 V, the inverted device efficiency is greater than the conventional device, resulting in a maximum recorded power conversion efficiency of 3.50%. A full summary of device performance parameters is listed in **Table 3-1**.

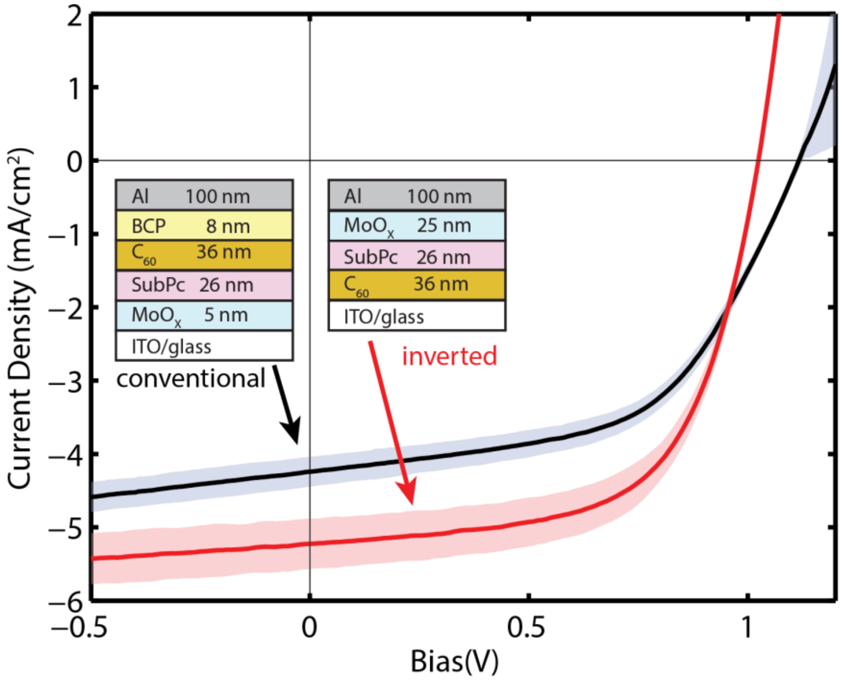

Figure 3-3 Current density-voltage curves comparing conventional and inverted devices. There is a clear tradeoff between a high V_{OC} in the conventional device (black), and high J_{SC} in the inverted device (red) for a devices with a 26 nm SubPc film. Shaded areas represent a 95% confidence interval.

Table 3-1: JV parameters of cOPV and iOPV.

	J_{SC} (mA/cm2)	V_{OC} (V)	FF (%)	PCE (%)
cOPV	4.15 ± 0.19	1.11 ± 0.026	54.6 ± 1.0	2.50 ± 0.56
iOPV	5.23 ± 0.36	1.02 ± 0.005	61.8 ± 0.5	3.31 ± 0.22

We note, however, that modeling predicted an exciton flux of 2.38×10^{16} cm^{-2} s^{-1} in the iOPV device, equivalent to J_{SC} = 3.81 mA/cm^2. One intuitively obvious source of the discrepancy might be variations in film thickness between the two devices, but extensive sampling and similarity in the deposition methods significantly reduce that as a possibility, necessitating a different hypothesis. Although the (conventional) SubPc/MoO_X and BCP/C_{60} interfaces are well established to be, respectively, exciton-quenching [20, 21] and exciton-reflecting [23], the behavior has not been established for inverted devices. To elucidate the boundary conditions for excitons at the interface between a buffer layer and an active layer, the SubPc film thickness was varied. The V_{OC}, J_{SC}, FF, and PCE of these devices are seen in **Figure 3-4**. For all values of SubPc thickness, the V_{OC} of iOPV devices is lower than that of cOPV devices, while the J_{SC} is larger. The fill factor is lower for iOPV devices for 13 nm thick SubPc, but higher for thicker films. The peak PCE for iOPV devices exceeds that for cOPV cells and occurs at 26 nm of SubPc. In general, increasing the thickness of an active layer in an optimized stack will reduce the J_{SC} and PCE. Increases in the J_{SC} with thickness especially suggest that the exciton diffusion length and boundary conditions assumed from literature must be re-evaluated for the iOPV devices.

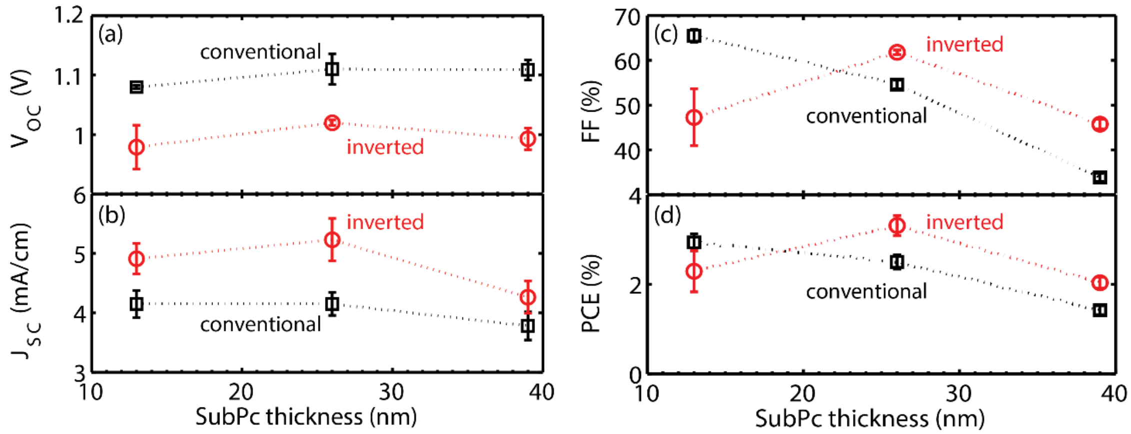

Figure 3-4 (a) V_{OC}, (b) J_{SC}, (c) FF, and (d) PCE of iOPV (red circles) and cOPV (black squares) devices versus thickness of SubPc while all other film thicknesses are unchanged.

A wide range of values for the exciton diffusion length of C_{60}, $L_{D\text{-}C60}$, has been reported, ranging from 7 nm to 40 nm, but is most commonly accepted to be ~15 nm.[24-27] Exciton diffusion in SubPc has been reported to be dominated by Förster transfer [28]. With a value of $L_{D\text{-}SubPc}$ = 7.7 nm when corrected for Förster transfer to the acceptor [29], and ~8 nm when uncorrected and adjacent to C_{60} [30-32]. Photoluminescence quenching studies have not been performed for C_{60}, which exhibits rapid intersystem crossing to a dark triplet state that is believed to be responsible for its long exciton diffusion length [26]. Fitting both EQE spectra with a SubPc thickness of 26 nm is shown in **Figure 3-6**. Note that the predicted EQE peak at 595 nm is below that of the measured peak for the cOPV. This is often seen in OPVs with a MoO_X\SubPc junction, which is assumed to be perfectly quenching, though it’s likely to be partially reflecting, hence the higher EQE in the measured curve.

3.5 Interface characterization

The exciton handling nature of the interfaces (i.e. reflecting, quenching, or dissociating) changes upon inversion. Fitting the EQE of all inverted devices simultaneously requires that the C_{60}/ITO interface is dissociating, revealing that it contributes approximately 0.77 mA/cm^2 to the J_{SC} of the inverted devices. This accounts for 55% of the difference between measured and calculated current in inverted devices. The exciton-dissociating nature of the C_{60}/ITO interface is confirmed experimentally, with the JV curve plotted in **Figure 3-5**. At 1 sun illumination, the C_{60}/ITO interface is contributing the correct order of magnitude, ~ 0.5 mA/cm^2, to the J_{SC} of the iOPV.

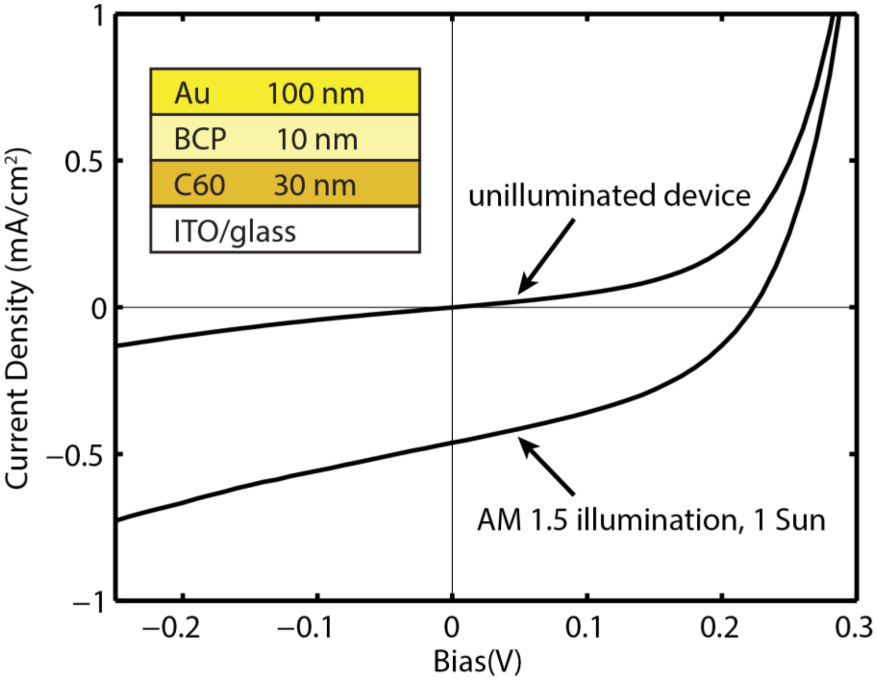

Figure 3-5 Current density vs. bias plot of a Schottky diode formed by C_{60} and ITO. Although the V_{OC} is 0.24 V in this device, the junction will dissociate excitons up to V_{OC}.

Perhaps more unexpected is that the remaining 45% of the difference between measured and calculated J_{SC} can be accounted for by allowing the MoO_X/SubPc interface to reflect excitons. It has recently been established that this interface in conventional devices is largely a quenching interface [33], and our data supports this conclusion when fitting cOPV devices. However, the very same interface in iOPV devices is responsible for exciton reflection, allowing for the same exciton flux from SubPc despite the lower absorption, resulting in a higher EQE at 600 nm, where SubPc absorbs strongly.

The change in exciton behavior at the SubPc/MoO_x interface is plausible, if the oxide undergoes a chemical transformation. The junction between aluminum and MoO_X is likely to be reactive, oxidizing aluminum and reducing molybdenum(VI) to molybdenum(IV), thus forming a tertiary mixture [36]. Oxygen deficiencies and molybdenum reduction have been shown to shift the valence and conduction bands, as well as modify the d-band filling, which transitions the material behavior between that of an n-type semiconductor and metal [37]. The electronic levels of the tertiary compound may be less amenable to exciton quenching from SubPc, explaining the exciton reflecting boundary condition necessary to fit EQE data to physically plausible exciton diffusion lengths. Indeed, a report by Sykes, et al., observed that EQE spectra in metal-organic-metal plasmonic cavity PV devices could be better explained if the model assumed a similar change from exciton-quenching to exciton-reflecting behavior by the SubPc/MoO_3 interface [38].

3.5.1 Diffusion length

The exciton diffusion lengths for the cOPV and iOPV sets are fit independently of each other to find that they are similar, regardless of deposition order. As seen in **Table 3-2**, $L_{D\text{-}C60}$ remains approximately 16 nm for all SubPc thicknesses, despite the optical fields varying with SubPc thickness.

Table 3-2: Diffusion lengths fit for various SubPc thickness

SubPc thickness (nm)	$L_{D\text{-}SubPc}$ (nm)	$L_{D\text{-}C60}$ (nm)
13	8.5	16.1
26	15.5	16.1
39	19.0	16.2

Varying the optical fields will shift the depth of peak exciton generation, which will cause $L_{D\text{-}C60}$ to vary if the boundary conditions are incorrect or the diffusion length varies with thickness. However, $L_{D\text{-}SubPc}$ does vary with SubPc thickness, indicating that morphological changes occur as thicker films are deposited, or the MoO_X\SubPc interface is partially dissociating. Though it has been suggested that the MoO_X\SubPc interface forms a Schottky junction that contributes to the high V_{OC} of SubPc\C_{60} devices, this is only observed at cryogenic temperatures [33]. Indeed, 15.5 nm for a SubPc thickness of 26 nm, although higher than in some other reports, corroborates a previously reported increase in $L_{D\text{-}SubPc}$ with SubPc film thickness even without MoO_X [34, 35].

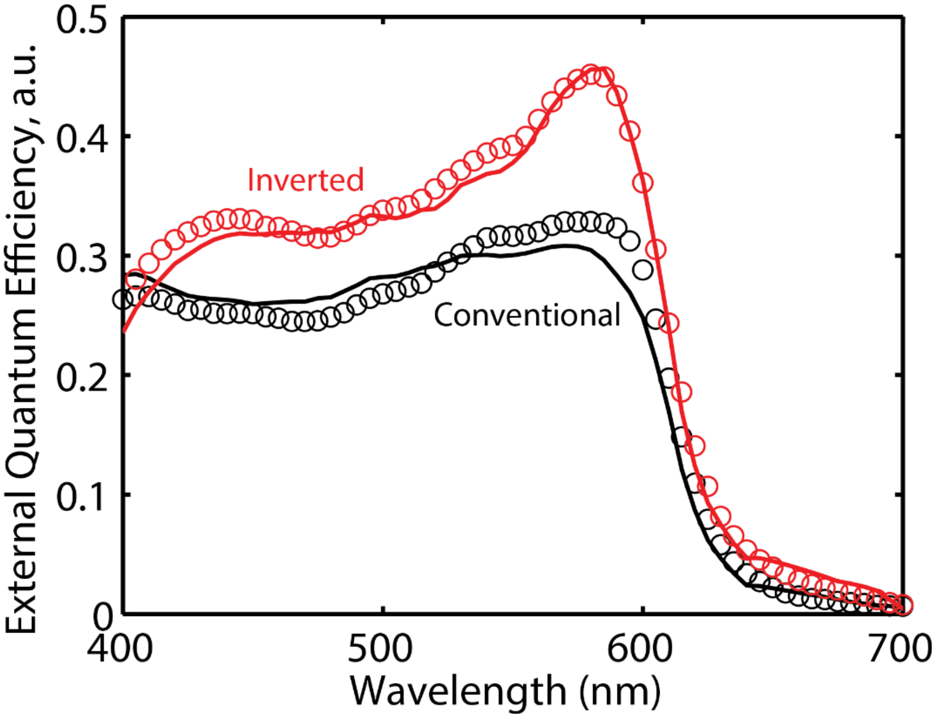

Figure 3-6 External quantum efficiency spectra for the iOPV (red) and cOPV (black), with calculated (solid) and measured (open circles) values. Note that the cOPV EQE peak near 600 nm originates from current collected from the SubPc film, where the MoO_X interface is assumed to be perfectly quenching in the simulation; the experimental peak, however, is slightly higher, suggesting quenching efficiency is high, but not unity.

We found that the exciton diffusion lengths remain constant regardless of deposition order, but molecular templating (or lack thereof) could conceivably occur, potentially increasing the exciton diffusion length in any active layer, thus affecting J_{SC}.

Previous templating studies have improved film crystallinity, which has created anisotropy in the exciton diffusion length, resulting in higher current density when the diffusion length was increased perpendicular to the heterojunction [39]. While improved crystallinity could increase exciton diffusion length, it would also lead to greater wave function overlap at the donor-acceptor interface, increasing parasitic polaron pair recombination [40]. Though this templating-based explanation is a possibility, X-ray diffraction studies of the multi-layers used here show completely amorphous active layers. Amorphous results were found regardless of deposition of C_{60} on SubPc or SubPc on C_{60}, even for multiple thickness, as shown in **Figure 3-7**. However, the use of grazing incidence X-ray diffraction may offer additional morphology information [41].

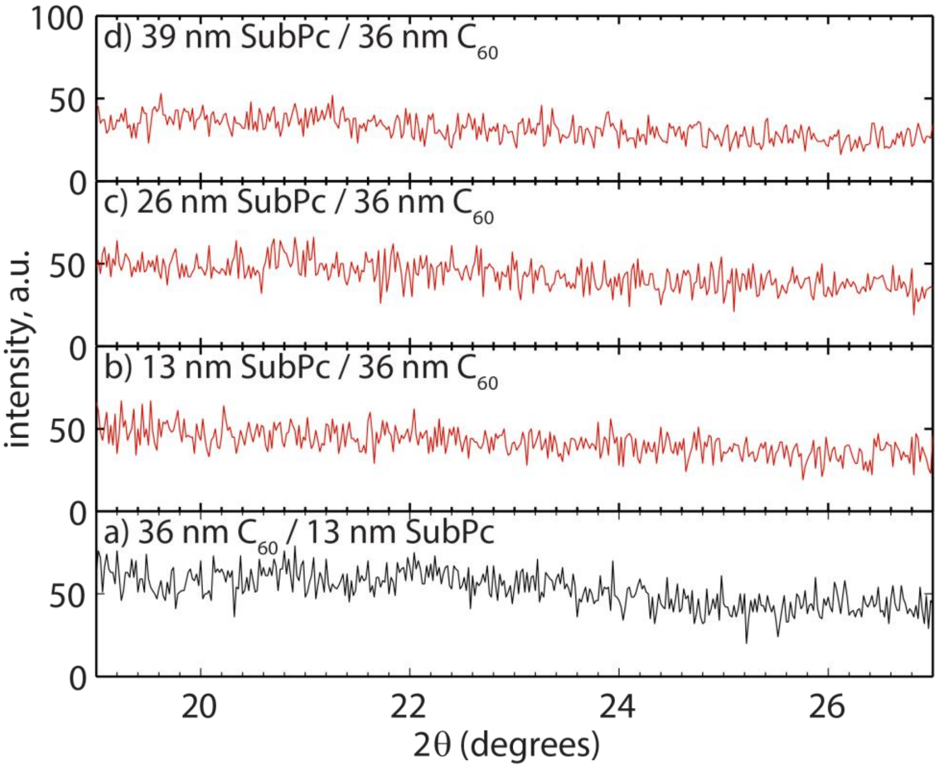

Figure 3-7 X-ray diffraction data for a sweep of 19 to 27 degrees of active layers deposited on a silicon substrate. Completely amorphous morphology is shown for all stacks, including a) 36 nm C_{60} on 13 nm SubPc, b) 13 nm SubPc on 36 nm C_{60}, c) 26 nm SubPc on 36 nm C_{60}, and d) 39 nm SubPc on 36 nm C_{60}.

Although templating of SubPc on MoO_X and C_{60} on ITO was not explored, they are unlikely due to the highly disordered nature of the oxides, whereas the J_{SC} difference is well explained by exciton boundary conditions at buffer layer interfaces. Additionally, as previously discussed, the diffusion lengths align well with previously reported values, suggesting that morphology is similar as well. In light of this, we discount templating with regard to SubPc on MoO_X, or C_{60} on ITO, from having a significant effect on diffusion lengths or J_{SC}. However, short range ordering has been seen in SubPc-C_{60} mixtures [42], which suggests that an interface between the two (i.e. occurring only at the heterojunction) may exhibit similar nanocrystalline morphologies. Thus, SubPc-on-C_{60} versus C_{60}-on-

SubPc layer deposition sequences could show differences in short range ordering that will affect the dark current and V_{OC}.

Both inverted and conventional SubPc/C_{60} OPVs have been reported in literature with V_{OC} values that match those reported in this work: 1.10 V for conventional devices, and 1.00 V for inverted devices [2]. Despite greatly increasing the built-in potential (V_{bi}), Tong *et al.* saw the iOPV V_{OC} saturate at 1.0 V, rather than 1.10 V as with the cOPV, suggesting fundamentally different diode properties. This potentially can be attributed to a difference in morphology at the interface, with the average polaron pair separation distance or local electric field affecting charge transfer and separation, per Onsager-Braun theory [43]. Alternatively, the V_{OC} may drop as a result of greater recombination due to increased surface roughness or differences in interfacial mixing as a result of the greater potential energy of C_{60} over SubPc during deposition. Lastly, the V_{OC} is directly related to the offset between the LUMO energy of the acceptor and the HOMO energy of the donor, which may be shifted from their measured values as a result of Fermi level pinning and band bending [44].

3.6 Conclusions

In conclusion, we explore the tradeoff between J_{SC} and V_{OC} exhibited between cOPV and iOPV architectures, with the iOPV reaching a power conversion efficiency of 3.50%. In depth analysis reveals the ability of MoO_X to reflect excitons when adjacent to SubPc, as well as a Schottky junction between the acceptor and cathode, resulting in a cascade device despite using fewer processing steps and films than the conventional device alone. This demonstrates the unrealized potential in processing existing materials, which may result in pushing OPVs to greater efficiencies, especially when used in conjunction with anode-based cascade junctions. Though the nearly 100 mV difference in V_{OC} between the iOPV and cOPV not yet explained, future work is intended to explore the possibility of variations in the polaron pair orientation *in silico* to address the contribution of heterojunction morphology to this difference.

3.7 References

[1] F. Zhang, X. Xu, W. Tang, J. Zhang, Z. Zhuo, J. Wang, J. Wang, Z. Xu, Y. Wang, Recent development of the inverted configuration organic solar cells, Solar Energy Materials and Solar Cells, 95 (2011) 1785-1799.

[2] X. Tong, B.E. Lassiter, S.R. Forrest, Inverted organic photovoltaic cells with high open-circuit voltage, Organic Electronics, 11 (2010) 705-709.

[3] C. Trinh, J.R. Bakke, T.P. Brennan, S.F. Bent, F. Navarro, A. Bartynski, M.E. Thompson, Power losses in bilayer inverted small molecule organic solar cells, Applied Physics Letters, 101 (2012) 233903.

[4] S. Wilken, T. Hoffmann, E. von Hauff, H. Borchert, J. Parisi, ITO-free inverted polymer/fullerene solar cells: Interface effects and comparison of different semi-transparent front contacts, Solar Energy Materials and Solar Cells, 96 (2012) 141-147.

[5] X. Tong, R.F. Bailey-Salzman, G. Wei, S.R. Forrest, Inverted small molecule organic photovoltaic cells on reflective substrates, Applied Physics Letters, 93 (2008) 173304.

[6] B. O’Connor, K.P. Pipe, M. Shtein, Fiber based organic photovoltaic devices, Applied Physics Letters, 92 (2008) 193306.

[7] C.H. Chou, W.L. Kwan, Z. Hong, L.M. Chen, Y. Yang, A metal-oxide interconnection layer for polymer tandem solar cells with an inverted architecture, Adv Mater, 23 (2011) 1282-1286.

[8] A. Colsmann, J. Junge, C. Kayser, U. Lemmer, Organic tandem solar cells comprising polymer and small-molecule subcells, Applied Physics Letters, 89 (2006) 203506.

[9] B. O?Connor, D. Nothern, K.P. Pipe, M. Shtein, High efficiency, broadband solar cell architectures based on arrays of volumetrically distributed narrowband photovoltaic fibers, Opt. Express, 18 (2010) A432-A443.

[10] S. Biswas, K.A. Luck, M. Shtein, Guard flow-enhanced organic vapor jet printing of photovoltaic donor materials in air, Organic Electronics, 13 (2012) 2905-2909.

[11] M.T. Lloyd, C.H. Peters, A. Garcia, I.V. Kauvar, J.J. Berry, M.O. Reese, M.D. McGehee, D.S. Ginley, D.C. Olson, Influence of the hole-transport layer on the initial behavior and lifetime of inverted organic photovoltaics, Solar Energy Materials and Solar Cells, 95 (2011) 1382-1388.

[12] H.R. Wu, Q.L. Song, M.L. Wang, F.Y. Li, H. Yang, Y. Wu, C.H. Huang, X.M. Ding, X.Y. Hou, Stable small-molecule organic solar cells with 1,3,5-tris(2-N-phenylbenzimidazolyl) benzene as an organic buffer, Thin Solid Films, 515 (2007) 8050-8053.

[13] M.F. Lo, T.W. Ng, T.Z. Liu, V.A.L. Roy, S.L. Lai, M.K. Fung, C.S. Lee, S.T. Lee, Limits of open circuit voltage in organic photovoltaic devices, Applied Physics Letters, 96 (2010) 113303.

[14] J. Meiss, M.K. Riede, K. Leo, Optimizing the morphology of metal multilayer films for indium tin oxide (ITO)-free inverted organic solar cells, Journal of Applied Physics, 105 (2009) 063108.

[15] J. Meiss, M.K. Riede, K. Leo, Towards efficient tin-doped indium oxide (ITO)-free inverted organic solar cells using metal cathodes, Applied Physics Letters, 94 (2009) 013303.

[16] Y. Zang, J. Huang, H. Li, J. Yu, Y. Jiang, Effect of Molybdenum Oxide Anode Buffer Layer on the Performance of Inverted Small Molecular Organic Solar Cells, Energy Procedia, 12 (2011) 513-518.

[17] J.-J. Zhu, Z.-Q. Xu, G.-Q. Fan, S.-T. Lee, Y.-Q. Li, J.-X. Tang, Inverted polymer solar cells with atomic layer deposited CdS film as an electron collection layer, Organic Electronics, 12 (2011) 2151-2158.

[18] I. Hancox, P. Sullivan, K.V. Chauhan, N. Beaumont, L.A. Rochford, R.A. Hatton, T.S. Jones, The effect of a MoOx hole-extracting layer on the performance of organic photovoltaic cells based on small molecule planar heterojunctions, Organic Electronics, 11 (2010) 2019-2025.

[19] N. Giebink, S. Forrest, Limits to accumulation of electric-field-stabilized geminate polaron pairs in an organic semiconductor thin film, Physical Review B, 76 (2007).

[20] A. Barito, M.E. Sykes, D. Bilby, J. Amonoo, Y. Jin, S.E. Morris, P.F. Green, J. Kim, M. Shtein, Recovering lost excitons in organic photovoltaics using a transparent dissociation layer, Journal of Applied Physics, 113 (2013) 203110.

[21] X. Xiao, J.D. Zimmerman, B.E. Lassiter, K.J. Bergemann, S.R. Forrest, A hybrid planar-mixed tetraphenyldibenzoperiflanthene/C70 photovoltaic cell, Applied Physics Letters, 102 (2013) 073302.

[22] J. Xue, S.R. Forrest, Carrier transport in multilayer organic photodetectors: II. Effects of anode preparation, Journal of Applied Physics, 95 (2004) 1869-1877.

[23] P. Peumans, S.R. Forrest, Very-high-efficiency double-heterostructure copper phthalocyanine/C[sub 60] photovoltaic cells, Applied Physics Letters, 79 (2001) 126.

[24] L.A.A. Pettersson, L.S. Roman, O. Inganäs, Modeling photocurrent action spectra of photovoltaic devices based on organic thin films, Journal of Applied Physics, 86 (1999) 487.

[25] H. Gommans, B. Verreet, B.P. Rand, R. Muller, J. Poortmans, P. Heremans, J. Genoe, On the Role of Bathocuproine in Organic Photovoltaic Cells, Advanced Functional Materials, 18 (2008) 3686-3691.

[26] D. Qin, P. Gu, R.S. Dhar, S.G. Razavipour, D. Ban, Measuring the exciton diffusion length of C60 in organic planar heterojunction solar cells, physica status solidi (a), 208 (2011) 1967-1971.

[27] P. Peumans, S. Uchida, S.R. Forrest, Efficient bulk heterojunction photovoltaic cells using small-molecular-weight organic thin films, Nature, 425 (2003) 158-162.

[28] S.M. Menke, W.A. Luhman, R.J. Holmes, Tailored exciton diffusion in organic photovoltaic cells for enhanced power conversion efficiency, Nature materials, 12 (2013) 152-157.

[29] W.A. Luhman, R.J. Holmes, Investigation of Energy Transfer in Organic Photovoltaic Cells and Impact on Exciton Diffusion Length Measurements, Advanced Functional Materials, 21 (2011) 764-771.

[30] W.A. Luhman, R.J. Holmes, Adv. Funct. Mater., 21 (2011) 764-771.

[31] R.R. Lunt, N.C. Giebink, A.A. Belak, J.B. Benziger, S.R. Forrest, J. Appl. Phys., 105 (2009) 053711-053711-053717.

[32] H. Gommans, B. Vereet, B.P. Rand, R. Muller, J. Poortmans, P. Heremans, J. Genoe, Adv. Funct. Mater., 18 (2008) 3686-3691.

[33] Y. Zou, R.J. Holmes, Influence of a MoOx interlayer on the open-circuit voltage in organic photovoltaic cells, Applied Physics Letters, 103 (2013) 053302.

[34] H. Gommans, S. Schols, A. Kadashchuk, P. Heremans, S.C.J. Meskers, Exciton Diffusion Length and Lifetime in Subphthalocyanine Films, The Journal of Physical Chemistry C, 113 (2009) 2974-2979.

[35] K.J. Bergemann, S.R. Forrest, Measurement of exciton diffusion lengths in optically thin organic films, Applied Physics Letters, 99 (2011) 243303.

[36] M. Kassem, Phase relations in the Al2O3-MoO3 and Al-MoO3 systems, investigated by X-ray powder diffraction, FTIR, and DTA techniques, Inorg Mater, 42 (2006) 165-170.

[37] M.T. Greiner, M.G. Helander, W.M. Tang, Z.B. Wang, J. Qiu, Z.H. Lu, Universal energy-level alignment of molecules on metal oxides, Nature materials, 11 (2012) 76-81.

[38] M.E. Sykes, A. Barito, J.A. Amonoo, P.F. Green, M. Shtein, Broadband Plasmonic Photocurrent Enhancement in Planar Organic Photovoltaics Embedded in a Metallic Nanocavity, Advanced Energy Materials, (2014) 1301937.

[39] B.E. Lassiter, R.R. Lunt, C.K. Renshaw, S.R. Forrest, Structural templating of multiple polycrystalline layers in organic photovoltaic cells, Opt. Express, 18 (2010) A444-A450.

[40] M.D. Perez, C. Borek, S.R. Forrest, M.E. Thompson, Molecular and Morphological Influences on the Open Circuit Voltages of Organic Photovoltaic Devices, Journal of the American Chemical Society, 131 (2009) 9281-9286.

[41] C. Schünemann, D. Wynands, L. Wilde, M.P. Hein, S. Pfützner, C. Elschner, K.-J. Eichhorn, K. Leo, M. Riede, Phase separation analysis of bulk heterojunctions in

small-molecule organic solar cells using zinc-phthalocyanine and C60, Physical Review B, 85 (2012) 245314.

[42] R. Pandey, A.A. Gunawan, K.A. Mkhoyan, R.J. Holmes, Efficient Organic Photovoltaic Cells Based on Nanocrystalline Mixtures of Boron Subphthalocyanine Chloride and C60, Advanced Functional Materials, 22 (2012) 617-624.

[43] C.L. Braun, Electric field assisted dissociation of charge transfer states as a mechanism of photocarrier production, The Journal of Chemical Physics, 80 (1984) 4157.

[44] T.W. Ng, M.F. Lo, Z.T. Liu, F.L. Wong, S.L. Lai, M.K. Fung, C.S. Lee, S.T. Lee, Substrate effects on the interface electronic properties of organic photovoltaic devices with an inverted C60/CuPc junction, Journal of Applied Physics, 106 (2009) 114501.

CHAPTER 4

CHEMICALLY MODIFIED POLARON PAIRS

The V_{OC} in OPVs is considerably lower than the minimum absorbed photon energy, reducing the practical efficiency of OPV cells relative to their thermodynamic limit [1]. While losses due to exciton binding energy are understood, other factors are currently debated. Previously demonstrated links between dark current and V_{OC} have suggested that charge recombination at the heterojunction is partially responsible [2], influenced by both molecular structure and ordering [3]. This chapter examines the influence of the permanent electric dipole moment of the donor molecule on V_{OC}.

4.1 Theory

As discussed in Chapter 2, Giebink *et al.* introduced an Onsager-Braun kinetics-based model for ideal organic photovoltaic heterojunctions, successfully fitting current-voltage characteristics of OPV devices across a wide range of environmental conditions [4]. In the Onsager-Braun model, the probability of dissociating a Coulombically bound polaron pair at the heterojunction depends on the charge separation distance and the local electric field. This probability is less than unity, and has the effect of reducing the V_{OC}, relative to the maximum allowed by the energy level difference ΔE_{HL}, minus the polaron pair binding energy E_{PP} according to Eq. (4-1):

$$qV_{OC} = \Delta E_{HL} - E_{PP} - kTln\left(\frac{k_r N_H N_L}{\frac{\varsigma J_X}{r_{PP}}}\right), \tag{4-1}$$

where k_r is the polaron pair recombination rate, N_H and N_L are the HOMO and LUMO tail densities, respectively, ς is the maximum polaron pair density, J_X is the exciton flux reaching the heterojunction, and r_{PP} is the polaron pair separation distance. The polaron pair binding energy is usually calculated from the charge separation distance, as a Coulombically bound pair.

$$E_{PP} = \frac{1}{4\pi\langle\epsilon_r\rangle\epsilon}\frac{q^2}{r_{PP}}. \tag{2-12}$$

Clearly, intermolecular distance and the spatial distribution of occupied and unoccupied molecular orbitals affect r_{PP}, which in turn affects E_{PP} and V_{OC}. Additionally, the polaron pair dissociation rate, k_{PPd}, has a dependence on the local dipoles' strength and orientation, as they contribute to electric field at the interface, although their significance is not fully understood [5-8].

4.2 Previous work

Some previous work used a contact transfer technique to study how the strength and orientation of an interfacial dipole affects V_{OC} [8]. The dipole shifts the ionization potential at the interface, thus increasing or decreasing $\Delta \boldsymbol{E_{HL}}$ and the V_{OC}. Similarly, there is also a shift in the LUMO-LUMO and HOMO-HOMO offset, which may weaken the driving force for charge transfer, resulting in a lower dissociation efficiency.

One widely used donor of interest is boron subphthalocyanine chloride (SubPc-Cl). Its permanent molecular dipole and asymmetry suggests that polaron pair recombination could be orientation dependent, as molecular orientation with respect to the acceptor will affect both r_{PP} and the local electric field during charge transfer and separation. In addition to becoming one of the archetypal materials used in small molecular OPVs, the SubPc-Cl/C_{60} junction is one of the first material sets to have its field-dependent recombination rate constant measured [9].

SubPc-Cl coupled with C_{60}, shown in **Figure 4-1a**, produces a large ΔE_{HL}, resulting in one of the highest reported V_{OC}'s for bilayer OPVs [10, 11]. Its short exciton lifetime limits exciton diffusion [12, 13], but at 585 nm the solid state absorption of SubPc-Cl exhibits a strong Q-band typical of porphyrins [14], arising from π-π* transitions in the conjugated macrocyclic ring [15, 16]. This strong absorption is in the yellow-orange range of the visible spectrum, where both solar photon flux and energy flux are relatively high. The high extinction coefficient [14] allows for thinner layers, which mitigates the short exciton diffusion length bottleneck. The high current density, when coupled with a high V_{OC}, enables efficiencies for single planar heterojunction devices upwards of 3% [11, 17]. Nevertheless, the observed V_{OC} for SubPc-Cl/C_{60} junctions is 0.8 volts below ΔE_{HL}, presumably due to polaron pair binding and the strength of the interfacial dipole *vis-à-vis* Eq. (4-1).

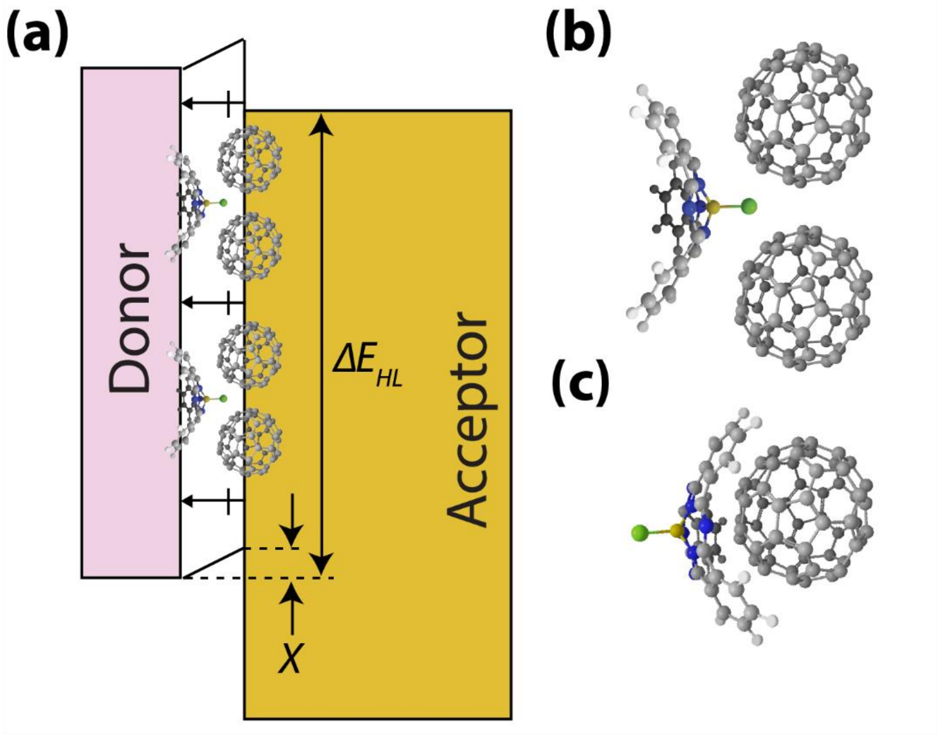

Figure 4-1 Energy levels are shifted by the dipole at the heterojunction, resulting in a decrease in ΔE_{HL}, as shown in (a). Potential orientations of SubPc include the (b) "bed" configuration and (c) "umbrella" configuration.

Halogenation of a donor is a common means of shifting the HOMO and LUMO as a means of engineering ΔE_{HL}, and thus significantly affecting the V_{OC} according to the first right-hand term of Eq. (4-1). Sullivan et al. have done this for SubPc, showing that it is capable of being used as an acceptor, despite its low electron mobility [18]. Although contradictory to expectations, they show V_{OC} to increase with a decrease in ΔE_{HL}, as shown in **Figure 4-2**. This can be attributed to poor dissociation due, again, to a low HOMO-HOMO or LUMO-LUMO offset. This type of substitution is undesirable, as it will significantly change the donor optical and electronic properties.

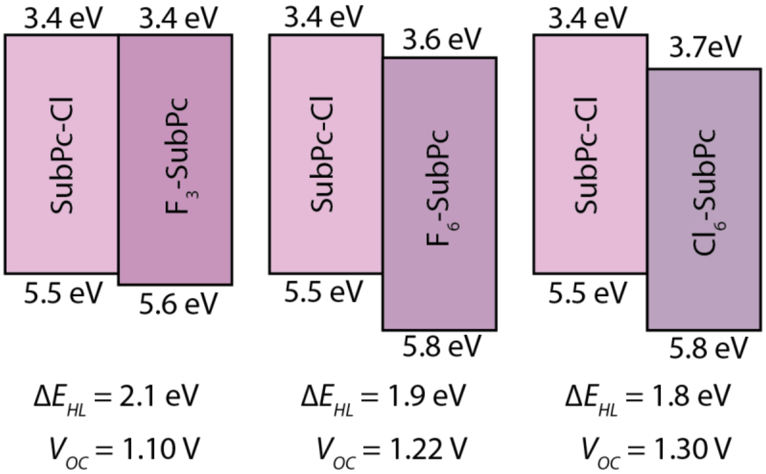

Figure 4-2 Effect of chemical modification on energy levels of donor molecules based on SubPc-Cl in which hydrogen on the macrocycle has been substituted for halogen atoms [18].

Substituting the axial chlorine atom for fluorine (creating SubPc-F) is expected to shorten then boron-halogen bond length, reducing the electric dipole of the donor molecule, thereby affecting the local polaron pair kinetics and presenting an opportunity to isolate the effects of molecular dipole strength. As previously mentioned, the macrocycle is largely responsible for the absorption, so substitution of the axial halogen is not expected to significantly affect absorption or exciton diffusion. Thus, it is possible to study the effect of nearly isolating the effect of dipole strength on device performance.

Below, we calculate the expected polaron pair geometry and dipole, followed by synthesis and characterization of both donor. We then compare performance characteristics of SubPc-Cl and SubPc-F donor layers in a heterojunction OPV cell with C_{60} as the acceptor material, highlighting important differences and interpreting them in terms of the molecular-scale mechanisms that may be responsible.

4.3 Polaron pairs *in silico*

Electronic structure determination for SubPc-F and SubPc-Cl were carried out through density functional theory (DFT) calculations in Gaussian 09, using the B3LYP functional and 6-31G(d) basis set for all atoms [19-21]. The molecular orbital basis set used was the 6-31G(d), as followed by Petersson *et al* [22]. The structures have been optimized using the above-mentioned basis set without any symmetry (allowing for a maximum of degrees of freedom). The UV absorption peaks were estimated considering the vertical excitations from the ground state applying time-dependent density functional linear response theory [23, 24].

Calculation of the polaron pair binding energy requires three contributions: the energy from Coulombic interaction, E_c, between the dimer electron (LUMO) and hole (HOMO), the interface polarization energy (E_p), and the Coulombic interaction between the induced charges at the interface and the polarons. Our calculations suggested that the latter contribution is negligible.

In order to calculate the E_c, molecules were first relaxed into their optimal isolated geometries, which were used to calculate the ionization energies of SubPc-Cl and SubPc-F, and electron affinity of C_{60}. Several configurations were calculated, notably a “bed” configuration, with the dipole facing SubPc, as seen in **Figure 1b**, and a ball-in-cup “umbrella” configuration, with a dipole facing C_{60}, as seen in **Figure 1c**. To compute the interaction, the empty HOMO was treated as a positively charged cloud, and, likewise, the LUMO was treated as a negatively charged cloud. This energy was computed from the wave function data projected onto a regular 3D grid as follows,

$$E_c = \frac{-q_e^2}{2\pi(\epsilon_{C60} + \epsilon_{SubPc})} \iint \frac{|\psi_H(\vec{r}_H)|^2 |\psi_L(\vec{r}_L)|^2}{|\vec{r}_H - \vec{r}_L|} d^3 r_H d^3 r_L, \tag{4-2}$$

where q_e is the charge of an electron, ϵ_{C60} is the dielectric constant of C_{60}, ϵ_{SubPc} is the dielectric constant of SubPc, $\psi_H$is the dimer HOMO, ψ_L is the dimer LUMO (See **Figure 4-1**), $\vec{r}_H$ is a position in the SubPc HOMO, and $\vec{r}_L$ is a position in the C_{60} LUMO.

Areas of the heterojunction where SubPc is regularly aligned with C_{60} have a net polarization at the interface. This system can be treated as a polarized monolayer at the interface of the two materials, similar to a polarizing interface texture effect. However, there is no dependence on the distance to the interface, thus the energy for transfer of a charge carrier across the interface is,

$$E_p = \frac{\sigma_{dp}\langle p_z \rangle}{2} \left[\frac{1}{\epsilon_{SubPc}} + \frac{1}{\epsilon_{C60}} \right]. \tag{4-3}$$

The interface polarization energy is $E_{\langle p_z \rangle}$, σ_{dp} is the dipole interface density, and $\langle p_z \rangle$ is the average individual dipole perpendicular to the interface. As mentioned above, we need to add E_c and $E_{\langle p_z \rangle}$ in order to calculate the binding energy. Therefore, the polaron pair binding energy is calculated through Eq. (4-4),

$$E_{PP} = E_c + E_{p.} \tag{4-4}$$

Based on *ab initio* calculations, the electron affinity of the fluorine atom changes the partial charges on the two molecules of the polaron pair, as well as causing structural differences in the donor, relative to SubPc-Cl. Specifically, the axial bond length of SubPc-F (1.39 Å) is shorter than SubPc-Cl (1.88 Å). Similarly, the calculated r_{PP} is 6.7 Å and 5.9 Å for SubPc-F and SubPc-Cl, respectively. The dipole of the donor results in an energetic hindrance to dissociation of the polaron pair into individual charge carriers, which has been calculated as an energy penalty equal to 0.17 eV and 0.24 eV for SubPc-F and SubPc-Cl, respectively. The calculated r_{PP} for the "bed" configuration is 9.3 Å and 9.1 Å for SubPc-F and SubPc-Cl, respectively. In this case, the dipole of the donor results in an energetic hindrance to dissociation of the polaron pair into individual charge carriers, which has been calculated as an energy penalty equal to 0.21 eV and 0.15 eV for SubPc-F and SubPc-Cl, respectively. Note that the larger separation distance for SubPc-F already provides a slightly lower binding energy, via Eq. (2). Subtraction of energetic assistance from the polaron pair binding energy has a direct influence on V_{OC}, as understood from Eq. (1).

4.4 SubPc-F synthesis and donor characterization

Subphthalocyanine fluoride (SubPc-F) was synthesized from SubPc-Cl, using a previously reported method [25], with the reaction shown in **Figure 4-3**. Following synthesis and evaporation of the solvent, products were rinsed with methanol and hexane (purchased from VWR and used as received) before subsequent purification by thermal gradient sublimation twice. The absence of SubPc-Cl and presence of SubPc-F was confirmed using atmospheric pressure chemical ionization mass spectroscopy, from which the purity was estimated to be greater than 92% SubPc-F by mass.

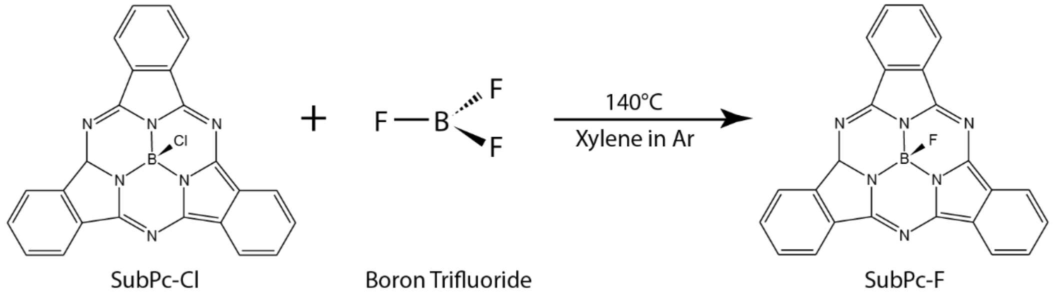

Figure 4-3 Reaction of SubPc-Cl with BF_3 to synthesize SubPc-F.

HOMO levels were measured by cyclic voltammetry on samples drop-cast onto a glassy carbon working electrode. Redox currents were recorded while ramping voltage at 0.1 V/s relative to an Ag/AgNO$_3$ reference electrode and Pt counter electrode in 0.1 M tetrabutylammonium hexaflourophosphate in acetonitrile. Ferrocene was used to calibrate the oxidation potential. LUMO levels were inferred by adding the optical absorption "bandgap" to the HOMO levels determined by cyclic voltammetry.

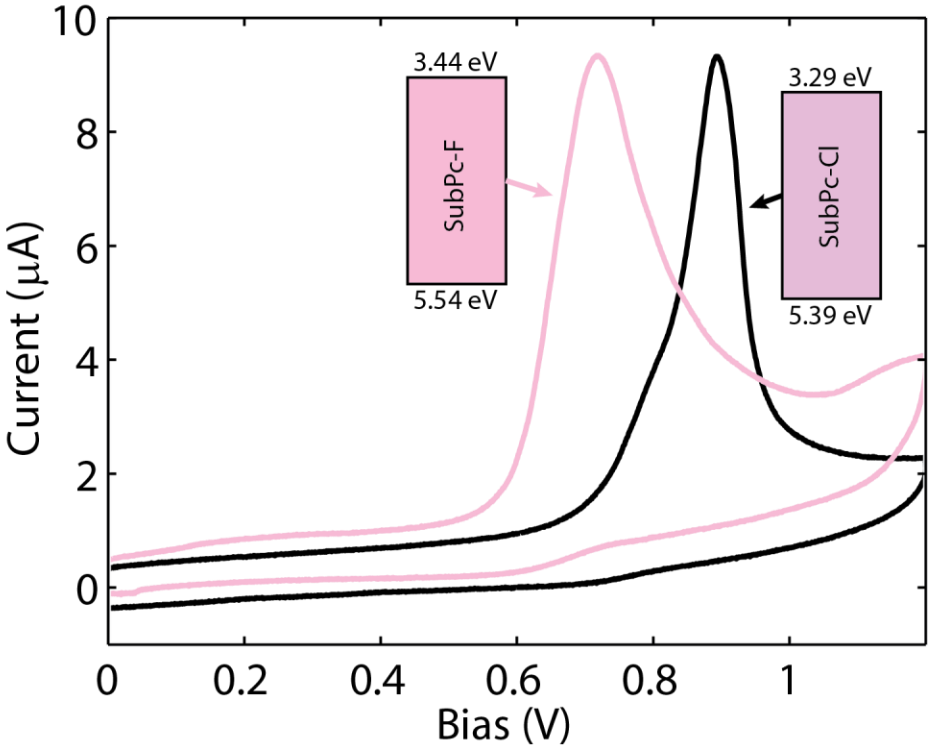

Figure 4-4 CV data performed on samples of SubPc-F and SubPc-Cl.

SubPc-Cl and -F complex refractive indices were fitted to measurements of 30 nm thick films on a silicon substrate. The refractive index and extinction coefficient for solid films are shown in **Figure 4-5**. As a result of the absorption being largely due to resonance within the macrocycle, the optical constants remain mostly unchanged upon halogen substitution. The characteristic absorption spectrum of the subphthalocyanine molecule peaks near 580 nm, and two higher energy shoulders at 570 nm and 540 nm are present. The intense peak in the Q region is blue-shifted 3 nm upon halogen substitution, from 585 nm to 582 nm. In agreement with experimental results, the TDDFT calculated UV absorptions suggest a 5 nm blue-shift.

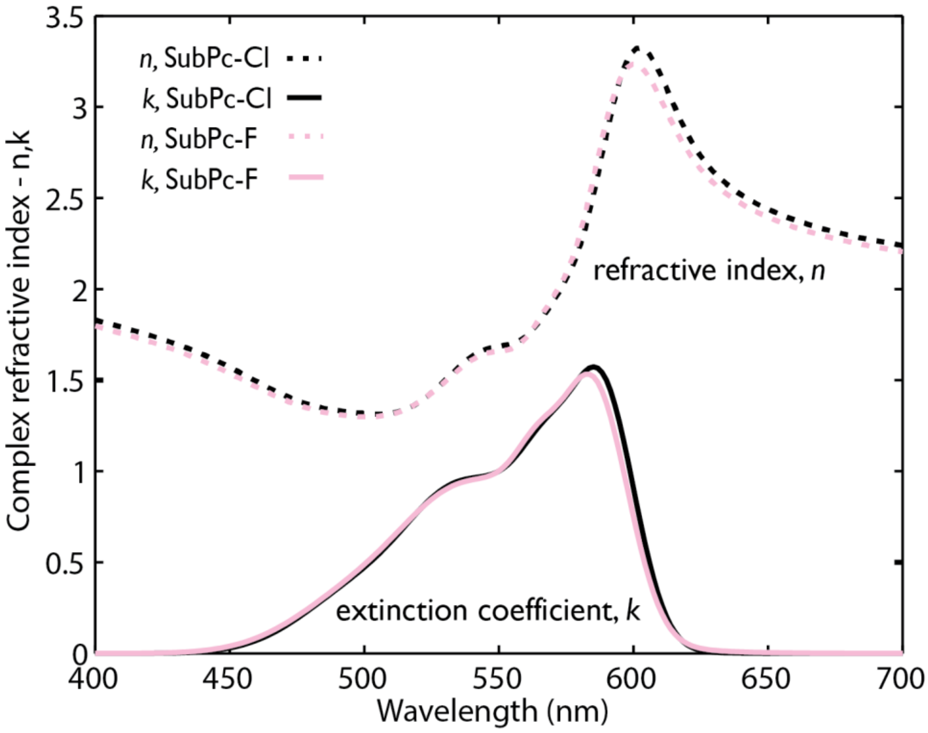

Figure 4-5 Imaginary (solid lines) and real (dotted lines) refractive indexes as function of wavelength for SubPc-Cl (black) and SubPc-F (red).

To ensure that mixing, crystallinity, and morphology were not difference between the SubPc-Cl and SubPc-F device, the topography of each donor was mapped with atomic force microscopy in tapping mode. The root-mean-square (RMS) roughness is 0.2 nm for MoO_X on ITO, shown in **Figure 4-6**, whereas the RMS roughness in SubPc-Cl and SubPc-F is 2.4 nm for each. To further ensure that the device performance would not be affected by differences in structure, X-ray diffraction way carried out on both films deposited on <100> Si. These results showed the donor films to be completely amorphous.

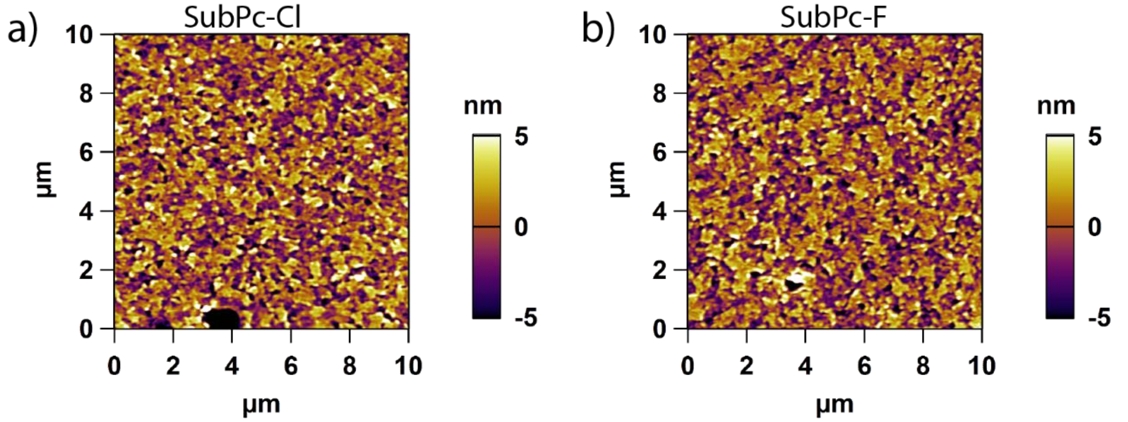

Figure 4-6 Images of the surface of (a) SubPc-Cl, and (b) SubPc-F. The root-mean-square roughness is 2.4 nm.

4.5 OPV devices

Organic and inorganic thin films were thermally evaporated under a pressure of 10^{-7} Torr while thickness was monitored *in situ* by a calibrated quartz crystal microbalance. Substrates consisted of 15 Ω/☐ ITO-coated glass slides purchased from Delta Technologies, LLC, and were cleaned in 250 mL each of dish soap in de-ionized water, pure de-ionized water, acetone, trichloroethylene twice, acetone twice, and 2-propanol twice before being boiled in a third beaker of 2-propanol for 10 minutes. After cleaning, substrates were immediately dried in nitrogen and treated using UV-generated ozone for 10 minutes. Film thicknesses used for devices were as follows: 5 nm MoO_3 \ 13 nm SubPc-X \ 36 nm C_{60} \ 10 nm BCP \ 100 nm Al, with the top cathode defined by depositing through a shadow-mask having approximately 1 mm diameter circular apertures; X = Cl or F. Film thicknesses were calibrated with spectroscopic ellipsometry. Photovoltaic cells were electrically characterized in an inert atmosphere under AM1.5D conditions for current density-voltage (JV) sweeps, and in air at 5 nm increments of monochromated light from a halogen lamp source for EQE measurements.

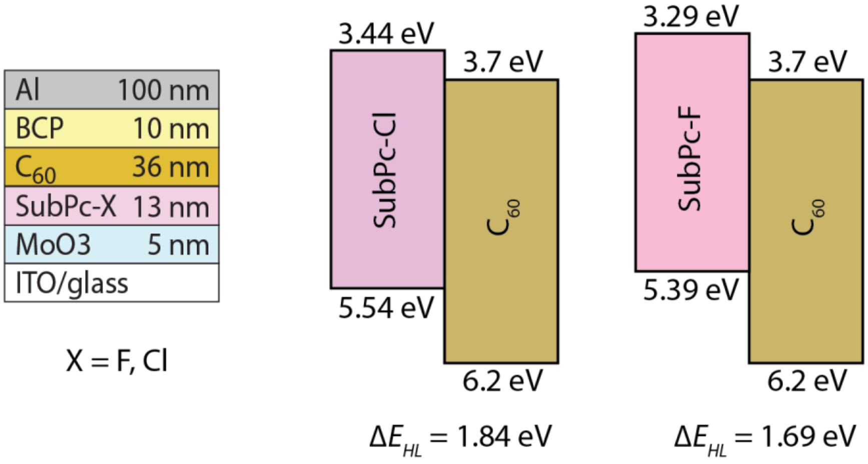

Figure 4-7 Diagram of (a) OPV stack and energy levels of active layers the device containing (b) SubPc-Cl as a donor, and (c) SubPc-F as a donor.

Following the work of Pettersson *et al.*, data from donor film characterization are used in a Feng-Ghosh model [26] to predict EQE spectra and ensure that the exciton flux reaching the heterojunction is similar between the two donors, thus allowing for a direct comparison of the V_{OC} among otherwise identically performing devices. Though stacks optimized for maximum efficiency upwards of 3% achieve this through increased absorption, thus increasing J_X, these changes have a minimal effect on the V_{OC}.

The experimentally measured EQE plotted in **Figure 4-8** shows that the absorption, exciton diffusion, exciton dissociation, and carrier collection at zero bias are largely the same between the two devices, resulting in similar EQE. It’s understood from the complex refractive index shown in **Figure 4-5** that absorption efficiency in a PV cell incorporating either material should remain nearly identical. Assuming the post-dissociation carrier collection efficiency for thin bilayer OPVs to be unity, exciton diffusion lengths fitted to the EQE suggest exciton dissociation efficiency to be comparable between the devices (L_D = 10.2 nm for SubPc-Cl, and 10.3 nm for SubPc-F). The interface between MoO_3 and SubPc has been recognized as not fully quenching, as understood from previously reported EQE fits [27], thus leading to overestimation of the exciton diffusion length in these samples [11, 13, 14].

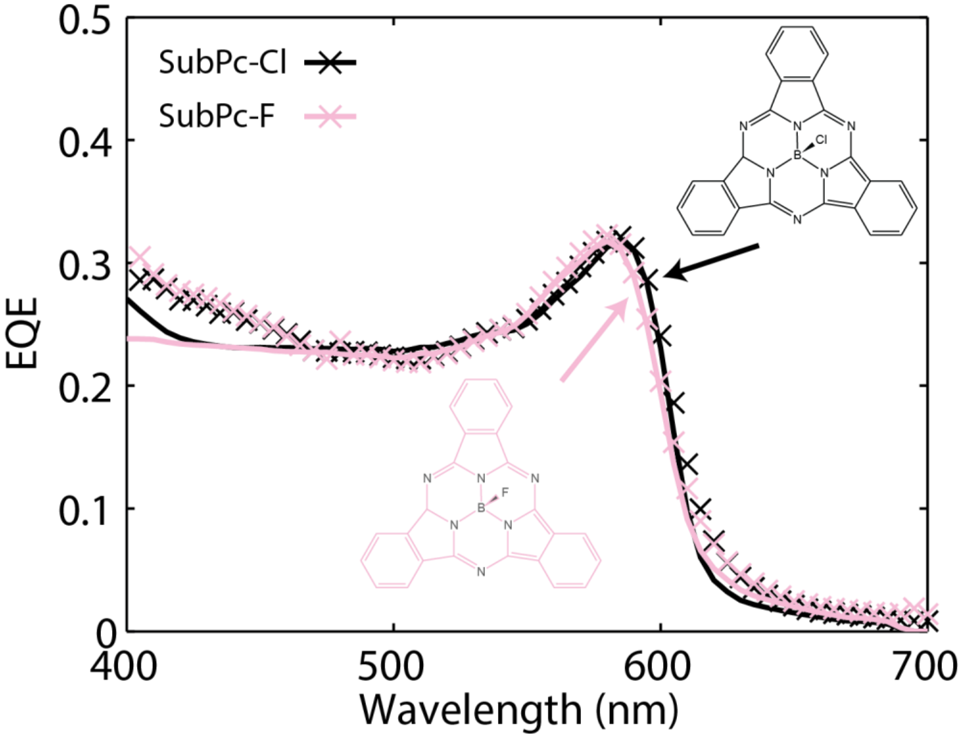

Figure 4-8 External quantum efficiency of devices made using SubPc-Cl (black) and SubPc-F (red) as the donor. Experimental measurements (X's) are overlaid on calculated EQE curves (solid lines).

The point wise product of the EQE and AM1.5D spectra results in similar short-circuit current density (J_{SC}) between the two devices. Though this is somewhat lower than the J_{SC} measured at zero bias under AM1.5D illumination, the loss is most likely due to degradation in air. Indeed, we see in **Table 4-1** that the J_{SC} is statistically the same between the two device sets. The largest difference between the performance of SubPc-Cl and

SubPc-F as OPV donors is clearly observed in the device current-voltage characteristics, as shown in **Figure 4-9**. The shaded areas show a 95% confidence interval on the measurement, further illustrating that the difference in current measurements near J_{SC} is not statistically significant. In contrast, the difference between the V_{OC} values is indeed significant. Despite being lower in absolute value, the V_{OC} of SubPc-F is substantially closer to the thermodynamic limit than that of SubPc-Cl, as discussed below.

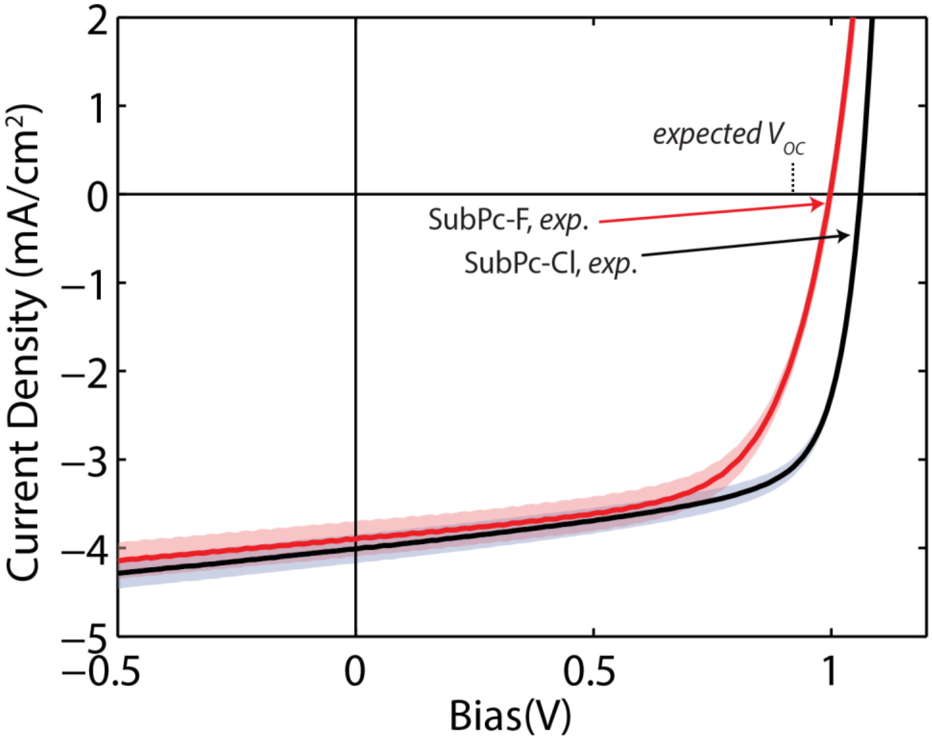

Figure 4-9 JV curves for ITO \ 5 nm MoO3 \ 13 nm SubPc \ 36 nm C_{60} \ 10 nm BCP \ 100 nm Al, where SubPc refers to either SubPc-F (red) or SubPc-Cl (black). Dark lines represent the mean values averaged over 9 devices, whereas shaded regions represent a 95% confidence interval at that bias.

Table 4-1: JV parameters of SubPc-Cl, SubPc-F, and the modeled SubPc-F

		SubPc-Cl (Exp.)	SubPc-F (Exp.)	SubPc-F (Calc.)
J_{SC}	mA/cm^2	4.0 ±0.26	3.9 ±0.23	3.85
V_{OC}	V	1.06 ±0.002	1.00 ±0.019	0.98
FF	%	67.0 ±1.0	62.8 ±2.1	63.9
PCE	%	2.85 ±0.16	2.44 ±0.22	2.40

4.6 Modeled dipole effects

One source of the absolute V_{OC} difference between SubPc-Cl and SubPc-F can be attributed to the shift in the HOMO and LUMO levels upon halogen substitution. The inset of **Figure 4-9** shows the electronic levels of the active organic layers. The measured SubPc-F HOMO and LUMO energy levels are uniformly shifted 150 meV towards vacuum level relative to SubPc-Cl. This shift brings the HOMO of the donor closer to the LUMO of the acceptor, reducing ΔE_{HL}, the first term of Eq. (4-1). Namely, $\Delta E_{HL-SubPc\text{-}Cl/\mathrm{C60}}$ = 1.84 eV, while $V_{OC-SubPc\text{-}Cl/\mathrm{C60}}$ = 1.06 V, implying that the last two terms of Eq. (4-1) add up to 0.78 eV, a 42.4% loss due to polaron pair binding and Onsager-Braun dynamics. In comparison, $\Delta E_{HL-SubPc\text{-}F/\mathrm{C60}}$ = 1.69 eV, while $V_{OC-SubPc\text{-}F/\mathrm{C60}}$ measures 1.00 V, implying that the last two terms of Eq. (4-1) add up to 0.69 eV, a 40.8% loss due to polaron pair binding and Onsager-Braun recombination dynamics.

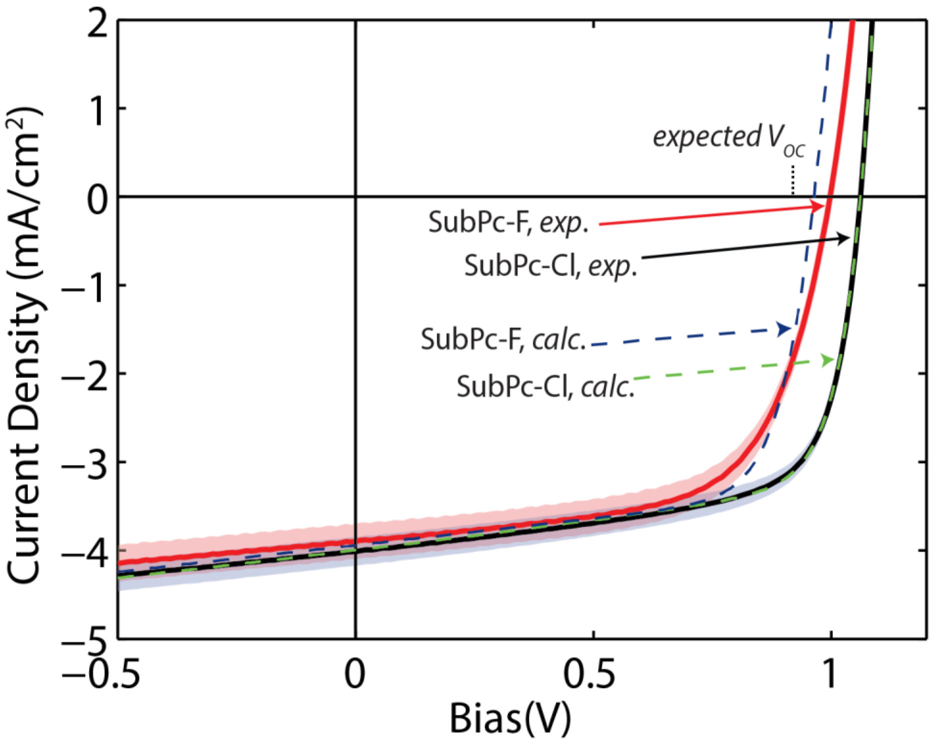

Figure 4-10 Fitted device JV curves using dipole model. The SubPc-F model is based solely on the SubPc-Cl fitting parameters except for HOMO energy, r_{PP} and X.

JV curves calculated using the model proposed by Giebink *et al.* are shown as dotted lines in **Figure 4-9**. The curve for the device using SubPc-Cl was fit to experimental data and used to generate the curve overlaid on the SubPc-F data, with only the HOMO level, LUMO level, polaron pair separation distance, and binding energy used from DFT calculations. The exciton flux from EQE modeling was fed into the model. Note that the modeled J_{SC} values are nearly identical to those that were measured. The J_{SC} of SubPc-F is lower than that of SubPc-Cl, despite less of an energetic barrier; however, this region of the JV curve is likely dominated by photoconductivity in the organics, rather than the junction dissociation efficiency [28]. As such, the lower J_{SC} for SubPc-F may simply be a result of lower exciton flux reaching the interface; however, a greater population of exciton quenching sites found in the (lower purity) SubPc-F may also lower J_{SC}. Additionally, the difference in fill factors is both an artifact of the lower V_{OC}, as well as potential trap states from impurities in SubPc-F, resulting in a higher ideality factor. This is especially prevalent in the comparison of modeled FF being so high, 68.4%. Importantly, much of the remaining difference between the modeled SubPc-F curve and measured SubPc-F curve is a result of the higher ideality factor. Most importantly, the V_{OC} is 0.97 V, which is particularly close to the measured value of 1.00 V, especially when considering the measurement is associated with a standard deviation of 19 mV. Creation of the SubPc molecule without a dipole will theoretically yield a device with a V_{OC} of approximately 0.90V.

Considering the possibility that the higher-than-expected V_{OC} is due to the polaron pair binding energy being lowered, we note the importance of dipole orientation. Brumbach *et al.* reported a V_{OC} for a titanyl phthalocyanine (TiOPc) donor achieving *less* of its potential maximum, as compared to copper phthalocyanine, which has no dipole. This could possibly be a result of TiOPc having a stronger dipole, but in a less favorable direction for polaron pair dissociation. Additional examples can be found in literature, where the use of the oblong-shaped C_{70} in place of spherical C_{60}, when paired with SubPc-Cl, affects the polaron pair orientations attainable without modification of the dipole. The maximum V_{OC} attainable is then 1.05 V for C_{70} [29, 30] versus 1.10 V for C_{60} [11], further supporting the link between polaron pair orientation and V_{OC}.

4.7 Summary

In summary, a new small molecular donor material has been synthesized and applied in the study of fundamental processes governing the performance of OPV cells, isolating the role of permanent electric dipole with other structural features of the molecule remaining identical. While axial substitution of fluorine for chlorine resulted in a smaller HOMO-LUMO gap at the heterojunction, detailed modeling of the heterojunction permitted the comparison of observed V_{OC} to its thermodynamic maximum value. While the V_{OC} of SubPc-F devices fall short of its thermodynamic limit, it is 90 mV higher than what is attained by SubPc-Cl relative to *its* thermodynamic limit. We attribute this net effect to the smaller dipole moment and the donor-acceptor interfacial structure that favor polaron pair dissociation. Furthermore, we have presented a framework for calculation of the JV curve for any polaron pair with a chemically modified dipole, assisted by *ab initio* calculations of the molecule structure and energetics.

4.8 References

[1] B. Rand, D. Burk, S. Forrest, Offset energies at organic semiconductor heterojunctions and their influence on the open-circuit voltage of thin-film solar cells, Physical Review B, 75 (2007) 115327.

[2] N. Li, B.E. Lassiter, R.R. Lunt, G. Wei, S.R. Forrest, Open circuit voltage enhancement due to reduced dark current in small molecule photovoltaic cells, Applied Physics Letters, 94 (2009) 023307.

[3] M.D. Perez, C. Borek, S.R. Forrest, M.E. Thompson, Molecular and Morphological Influences on the Open Circuit Voltages of Organic Photovoltaic Devices, Journal of the American Chemical Society, 131 (2009) 9281-9286.

[4] N.C. Giebink, G.P. Wiederrecht, M.R. Wasielewski, S.R. Forrest, Ideal diode equation for organic heterojunctions. I. Derivation and application, Physical Review B, 82 (2010) 155305.

[5] M. Brumbach, D. Placencia, N.R. Armstrong, Titanyl Phthalocyanine/C60 Heterojunctions: Band-Edge Offsets and Photovoltaic Device Performance, The Journal of Physical Chemistry C, 112 (2008) 3142-3151.

[6] W. Chen, S. Chen, S. Chen, Y. Li Huang, H. Huang, D.C. Qi, X.Y. Gao, J. Ma, A.T.S. Wee, Orientation-controlled charge transfer at CuPc/F16CuPc interfaces, Journal of Applied Physics, 106 (2009) 064910.

[7] A. Kumar, S. Sista, Y. Yang, Dipole induced anomalous S-shape I-V curves in polymer solar cells, Journal of Applied Physics, 105 (2009) 094512.

[8] A. Tada, Y. Geng, Q. Wei, K. Hashimoto, K. Tajima, Tailoring organic heterojunction interfaces in bilayer polymer photovoltaic devices, Nature materials, 10 (2011) 450-455.

[9] N.C. Giebink, B.E. Lassiter, G.P. Wiederrecht, M.R. Wasielewski, S.R. Forrest, Ideal diode equation for organic heterojunctions. II. The role of polaron pair recombination, Physical Review B, 82 (2010) 155306.

[10] K.L. Mutolo, E.I. Mayo, B.P. Rand, S.R. Forrest, M.E. Thompson, Enhanced Open-Circuit Voltage in Subphthalocyanine/C60 Organic Photovoltaic Cells, Journal of the American Chemical Society, 128 (2006) 8108-8109.

[11] R. Pandey, A.A. Gunawan, K.A. Mkhoyan, R.J. Holmes, Efficient Organic Photovoltaic Cells Based on Nanocrystalline Mixtures of Boron Subphthalocyanine Chloride and C60, Advanced Functional Materials, 22 (2012) 617-624.

[12] W.A. Luhman, R.J. Holmes, Investigation of Energy Transfer in Organic Photovoltaic Cells and Impact on Exciton Diffusion Length Measurements, Advanced Functional Materials, 21 (2011) 764-771.

[13] R.R. Lunt, N.C. Giebink, A.A. Belak, J.B. Benziger, S.R. Forrest, Exciton diffusion lengths of organic semiconductor thin films measured by spectrally resolved photoluminescence quenching, Journal of Applied Physics, 105 (2009) 053711.

[14] H.H.P. Gommans, D. Cheyns, T. Aernouts, C. Girotto, J. Poortmans, P. Heremans, Electro-Optical Study of Subphthalocyanine in a Bilayer Organic Solar Cell, Advanced Functional Materials, 17 (2007) 2653-2658.

[15] V.R. Ferro, J.M. García de la Vega, R.H. González-Jonte, L.A. Poveda, A theoretical study of subphthalocyanine and its nitro- and tertbutyl-derivatives, Journal of Molecular Structure: THEOCHEM, 537 (2001) 223-234.

[16] G.E. Morse, T.P. Bender, Boron subphthalocyanines as organic electronic materials, ACS applied materials & interfaces, 4 (2012) 5055-5068.

[17] X. Tong, B.E. Lassiter, S.R. Forrest, Inverted organic photovoltaic cells with high open-circuit voltage, Organic Electronics, 11 (2010) 705-709.

[18] P. Sullivan, A. Duraud, l. Hancox, N. Beaumont, G. Mirri, J.H.R. Tucker, R.A. Hatton, M. Shipman, T.S. Jones, Halogenated Boron Subphthalocyanines as Light Harvesting Electron Acceptors in Organic Photovoltaics, Advanced Energy Materials, 1 (2011) 352-355.

[19] A.D. Becke, Density-functional thermochemistry. III. The role of exact exchange, The Journal of Chemical Physics, 98 (1993) 5648-5652.

[20] C. Lee, W. Yang, R.G. Parr, Development of the Colle-Salvetti correlation-energy formula into a functional of the electron density, Physical Review B, 37 (1988) 785-789.

[21] M.J.T. Frisch, G. W.; Schlegel, H. B.; Scuseria, G. E.; Robb, M. A.; Cheeseman, J. R.; Scalmani, G.; Barone, V.; Mennucci, B.; Petersson, G. A.; Nakatsuji, H.; Caricato, M.; Li, X.; Hratchian, H. P.; Izmaylov, A. F.; Bloino, J.; Zheng, G.; Sonnenberg, J. L.; Hada, M.; Ehara, M.; Toyota, K.; Fukuda, R.; Hasegawa, J.; Ishida, M.; Nakajima, T.; Honda, Y.; Kitao, O.; Nakai, H.; Vreven, T.; Montgomery, J. A., Jr.; Peralta, J. E.; Ogliaro, F.; Bearpark, M.; Heyd, J. J.; Brothers, E.; Kudin, K. N.; Staroverov, V. N.; Kobayashi, R.; Normand, J.; Raghavachari, K.; Rendell, A.; Burant, J. C.; Iyengar, S. S.; Tomasi, J.; Cossi, M.; Rega, N.; Millam, N. J.; Klene, M.; Knox, J. E.; Cross, J. B.; Bakken, V.; Adamo, C.; Jaramillo, J.; Gomperts, R.; Stratmann, R. E.; Yazyev, O.; Austin, A. J.; Cammi, R.; Pomelli, C.; Ochterski, J. W.; Martin, R. L.; Morokuma, K.; Zakrzewski, V. G.; Voth, G. A.; Salvador, P.; Dannenberg, J. J.; Dapprich, S.; Daniels, A. D.; Farkas, Ö.; Foresman, J. B.; Ortiz, J. V.; Cioslowski, J.; Fox, D. J., Gaussian~09 Revision D.01, Gaussian, Inc.2009.

[22] G.A. Petersson, M.A. Al-Laham, A complete basis set model chemistry. II. Open-shell systems and the total energies of the first-row atoms, The Journal of Chemical Physics, 94 (1991) 6081-6090.

[23] R. Bauernschmitt, R. Ahlrichs, Treatment of electronic excitations within the adiabatic approximation of time dependent density functional theory, Chemical Physics Letters, 256 (1996) 454-464.

[24] A. Dreuw, M. Head-Gordon, Single-Reference ab Initio Methods for the Calculation of Excited States of Large Molecules, Chemical Reviews, 105 (2005) 4009-4037.

[25] J. Guilleme, D. González-Rodríguez, T. Torres, Triflate-Subphthalocyanines: Versatile, Reactive Intermediates for Axial Functionalization at the Boron Atom, Angewandte Chemie International Edition, 50 (2011) 3506-3509.

[26] L.A.A. Pettersson, L.S. Roman, O. Inganäs, Modeling photocurrent action spectra of photovoltaic devices based on organic thin films, Journal of Applied Physics, 86 (1999) 487.

[27] A. Barito, M.E. Sykes, D. Bilby, J. Amonoo, Y. Jin, S.E. Morris, P.F. Green, J. Kim, M. Shtein, Recovering lost excitons in organic photovoltaics using a transparent dissociation layer, Journal of Applied Physics, 113 (2013) -.

[28] C.K. Renshaw, J.D. Zimmerman, B.E. Lassiter, S.R. Forrest, Photoconductivity in donor-acceptor heterojunction organic photovoltaics, Physical Review B, 86 (2012) 085324.

[29] R. Pandey, Y. Zou, R.J. Holmes, Efficient, bulk heterojunction organic photovoltaic cells based on boron subphthalocyanine chloride-C70, Applied Physics Letters, 101 (2012) 033308.

[30] B.E. Lassiter, J.D. Zimmerman, A. Panda, X. Xiao, S.R. Forrest, Tandem organic photovoltaics using both solution and vacuum deposited small molecules, Applied Physics Letters, 101 (2012) -.

CHAPTER 5

CONCLUSIONS AND FUTURE WORK

5.1 Conclusions

OPVs are a promising technology for supplying a significant portion of the world's energy demands as it continues to grow. Rapid, inexpensive roll-to-roll production not limited by material cost or scarcity provides incredible potential for not only supplying power to portable devices, but also for large area installations, all with relative ease – potentially as simple as unrolling a solar foil on a roof. With low efficiency and short lifetime being the major limiting factors to commercial adoption, this work provides concepts to increase the V_{OC} and J_{SC} of OPVs, based on stack design and processing, to minimize exciton losses and engineer molecules for polaron pairs to include dissociation-assisting dipoles.

Chapter 2 discusses the major loss mechanisms, being absorption and exciton relaxation in J_{SC}, and non-radiative polaron pair recombination in the V_{OC}. A modified model is proposed that accounts for the physical separation distance between charge centers in a polaron pair. It suggests the use of two design elements for consideration when engineering molecules that form the polaron pair: (i) an optimal charge center separation distance, and (ii) a properly oriented dipole. Both of these can lower the polaron pair binding energy, thus increasing polaron dissociation relative to recombination, which will increase the V_{OC} closer to the thermodynamic limit suggested by Rau et al.

In Chapter 3, exploration into the feasibility of asymmetric donor orientation, especially one containing a dipole (i.e. SubPc-Cl) is attempted through the simple processing step of inverting the deposition order. Despite optimizing the inverted OPV stack for a lower J_{SC} than possible, a very high efficiency is observed for a SubPc-Cl/C_{60} device, despite using one fewer film, and fewer processing steps. A tradeoff is observed between high V_{OC} and high J_{SC}, with the former appearing in the conventional OPV and the latter in an inverted OPV. The high J_{SC} can be explained by the inverted process modifying the behavior of excitons with two interfaces adjacent to the heterojunction, those between the active layer and buffer layers. Rather than quenching excitons at on the donor side, and reflecting them on the acceptor side, as in the cOPV, the iOPV interfaces reflect and dissociate excitons at the donor and acceptor buffer interfaces, respectively. The iOPV is thus a cascade device, and significantly reduces losses from exciton relaxation.

In Chapter 4, the possibility of engineering the donor dipole is explored though chemical modification of SubPc-Cl. The axial chlorine atom in SubPc-Cl is for Fluorine, significantly increasing decreasing the dipole strength, from 4.83 Debye to 3.54 Debye, as calculated by DFT. After synthesis and characterization of SubPc-F, to have similar absorption to SubPc-Cl, but a lower HOMO energy of 5.39 eV versus 5.54 eV for SubPc-Cl, as measured by cyclic voltammetry, an approximately 8% lower V_{OC} in the device with SubPc-F as a donor, though the J_{SC} is statistically unchanged. DFT simulation of two likely polaron pairs for each donor suggest that the dipole of either SubPc molecule can increase or decrease the polaron pair binding energy. The energy change associated with the dipole of each polaron pair is calculated and used in the model suggested in Chapter 2 to predict the SubPc-F JV curve from the fitted diode properties originating from SubPc-Cl. The model comes close to reproducing the SubPc-F JV characteristics, though a perfect fit requires consideration of a higher ideality factor in the SubPc-F device, most likely as a result of the SubPc-F purity being lesser than that of SubPc-Cl. This suggests that the dipole can have a significant impact on reducing losses associated with the polaron pair binding energy, and should be considered, along with molecular orientation and separation distance, when designing a donor and acceptor for their polaron pair properties.

5.2 Future work

5.2.1 Additional axially modified molecules

Additional modified SubPc molecules should be created, namely SubPc-Br and SubPc-Ph, to verify that the dipole model is accurate. SubPc-Br has been calculated to have a dipole of 4.96 Debye, and, as such, should give a V_{OC} similar to SubPc-Cl in the absence of shifted energy levels. SubPc-Ph (i.e. boron subphthalocyanine phenol) should have a very weak dipole, but a much larger polaron pair separation, allowing for a trend with respect to dipole strength, though there is a greater potential for significant differences in molecular ordering. This being the case, grazing-incidence X-ray diffraction should be performed on all films, as this is more sensitive measurement technique for determining molecular ordering that standard XRD.

5.2.2 *Consideration of charge transfer*

One of the shortcomings in the model suggested in Chapter 2 is that the calculation of J_X is assumed to be completely independent of charge transfer and polaron pair dissociation. That is to say that the possibility of an exciton forming from a polaron pair is not considered, the rate forward rate for charge transfer is assumed to be much larger than the backward rate, thus the assumption of pure 100% charge transfer efficiency at the heterojunction is valid, and the two models may be calculated separately.

Considering that the HOMO-HOMO and LUMO-LUMO energy offset, ΔE_{HH} and ΔE_{LL}, respectively, is most efficient devices to date is large (i.e. >0.3 eV), these assumptions are expected. However, with the introduction of multi-layer cascade devices with some $\Delta E_{HH} \approx 0.1$ eV, and possibly less, this assumption must be called into question. More importantly, engineering polaron pairs to increase $r_{PP,}$ and thus k_{PPd}, will likely decrease charge transfer rates. Both of these effects are important for pushing efficiency of OPV devices higher, but will potentially cause the assumption of a zero population boundary condition for excitons at the heterojunction to be incorrect.

These two models, J_{SC} and JV calculations, should be bridged by charge transfer rates for the ability to better account for exciton population at the heterojunction, and intermediate polaron pair population, thus creating a more complete model of JV performance. The polaron pair separation distance can then be optimized for a balance between charge transfer and polaron pair dissociation.

Importantly, shifting the HOMO and LUMO levels of the donor relative to the acceptor, or vice versa, will affect ΔE_{HL} in opposition to ΔE_{HH} and ΔE_{LL}. Specifically, for a donor with a constant band gap, increasing ΔE_{HL}, which will increase V_{OC}, will decrease

ΔE_{HH} and ΔE_{LL}, thus decreasing charge transfer and lowering J_{SC}. This will demonstrate the suspected tradeoff between V_{OC} and J_{SC} that often discussed, and allow for optimization of the PCE.

5.2.3 Polaron pair dyad molecules

Designs of donor-acceptor dyads and triads have been demonstrated in single-layer OPVs with limited success, typically having a PCE under 2% [1, 2]. This is likely a result of high recombination and poor charge transport [3]. However, such molecules allow for precise design of polaron pair geometry, including breadth of r_{PP} distribution. Rather than using processing methods to attempt molecular alignment or surface roughening to control the V_{OC}, a monolayer of donor-acceptor dyad molecules could be placed at the interface of the donor and acceptor for more precise control of charge transfer and polaron pair dissociation. Donor and acceptor processing conditions can then be for high ordering, and thus high absorption with strong exciton and charge transport, whereas V_{OC} is controlled by the monolayer for polaron pair engineering.

5.3 References

[1] J. Roncali, Single Material Solar Cells: the Next Frontier for Organic Photovoltaics?, Advanced Energy Materials, 1 (2011) 147-160.

[2] Y. Lin, Y. Li, X. Zhan, Small molecule semiconductors for high-efficiency organic photovoltaics, Chemical Society reviews, 41 (2012) 4245-4272.

[3] X. Zhan, D. Zhu, Conjugated polymers for high-efficiency organic photovoltaics, Polymer Chemistry, 1 (2010) 409-419.

APPENDIX A

EQE MODEL CODE

Code to make EQE plot

```
clear all
clc

LineThickness = 4;
AxesThickness = 1;
BorderThickness = 2;
MarkerSize = 12;
FontSize = 18;
Transp = 0.25;

%% Figure 2 & S2 - EQE, IQE, Absorption
load('materials.mat','tauc60','tausubpc')
Ldc60 = 16E-9;                        % diffusion length of C60 (m)
Dc60 = Ldc60^2/tauc60;                % diffusivity of C60 (m^2/s)
Ldsubpccl =10E-9;                     % diffusion length of subpc (m)
Dsubpccl = Ldsubpccl^2/tausubpc;      % diffusivity of subpc (m^2/s)
Ldsubpcf = 10E-9;                     % diffusion length of subpc (m)
Dsubpcf = Ldsubpcf^2/tausubpc;        % diffusivity of subpc (m^2/s)
save('materials.mat','-append','Ldc60','Dc60','Ldsubpccl','Dsubpccl',
'Ldsubpcf','Dsubpcf')

[out] = OPV_Back_v3beta('standard subpc.txt', [153,5,13,33,10], {}, 0,
'TE', '');
subpccl.EQEcalc = out.EQE(10:100)';
subpccl.IQEcalc = out.IQE_tot(10:100)';
subpccl.Jcalc = out.J
subpccl.Abscalc = out.A_tot(10:100)';
%
[out] = OPV_Back_v3beta('standard subpcf.txt', [153,1,13,42,10], {}, 0,
'TE', '');
subpcf.EQEcalc = out.EQE(10:100)';
subpcf.IQEcalc = out.IQE_tot(10:100)';
subpcf.Jcalc = out.J
subpcf.Abscalc = out.A_tot(10:100)';

devsens = 1;
```

```
refsens = 1;
eqefile = '130620\EQE\130620BC';
Aeqe = pi()*(0.0503)^2; % cm^2
subpcf.EQE1 = EQE_dataExt(eqefile, Aeqe, devsens, refsens);
eqefile = '130620\EQE\130620BE';
Aeqe = pi()*(0.0501)^2; % cm^2
subpcf.EQE2 = EQE_dataExt(eqefile, Aeqe, devsens, refsens);
eqefile = '130620\EQE\130620BF';
Aeqe = pi()*(0.0509)^2; % cm^2
subpcf.EQE3 = EQE_dataExt(eqefile, Aeqe, devsens, refsens);
subpcf.EQE = mean([subpcf.EQE1,subpcf.EQE2,subpcf.EQE3],2);

devsens = 2;
refsens = 5;
eqefile = '130625\EQE\130625BE';
Aeqe = pi()*(0.0497)^2; % cm^2
subpccl.EQE1 = EQE_dataExt(eqefile, Aeqe, devsens, refsens);
eqefile = '130625\EQE\130625BF';
Aeqe = pi()*(0.0496)^2; % cm^2
subpccl.EQE2 = EQE_dataExt(eqefile, Aeqe, devsens, refsens);
eqefile = '130625\EQE\130625BH';
Aeqe = pi()*(0.0498)^2; % cm^2
subpccl.EQE3 = EQE_dataExt(eqefile, Aeqe, devsens, refsens);
subpccl.EQE = mean([subpccl.EQE1,subpccl.EQE2,subpccl.EQE3],2);

wl = 350:5:800;

figure(2); clf;
box
hold all
axis([400 700 0 0.5]);
set(gca, 'FontSize', FontSize,'linewidth',BorderThickness)
ylabel('EQE');
xlabel('Wavelength (nm)');
plot(wl, subpccl.EQE, 'blackx', 'linewidth', LineThickness/2,
'markersize', MarkerSize);
plot(wl-5, subpccl.EQEcalc, 'black', 'linewidth', LineThickness);
plot(wl, subpcf.EQE, 'redx', 'linewidth', LineThickness/2,
'markersize', MarkerSize);
plot(wl-5, subpcf.EQEcalc, 'red', 'linewidth', LineThickness);
saveas(gcf, 'figure3.ai')
saveas(gcf, 'figure3.fig')
```

Example input file ‘130505A.TXT’

```
air        1    env
glass      7E5  subs
ito        150  anode,tvar1
moo3       5    ebl,tvar2
subpccl    13   activeqd,tvar3
c60        36   activedr,tvar4
bcp        10   ebl,tvar5
al         100  cathode
air        1    env
```

‘OPV_Back_v3beta.m’

```
function [output] = OPV_Back_v3(stack, tvar, mvar, phi0, polarization,
LibSave)
% layers should be an array of strings containing the material names in
% lowercase letters, and t should be an array of corresponding
% thicknesses. Original source code: Brendan O'Connor; SE Morris and AJ
% Barito rewrote for advanced functions.
% This method follows that developed in Peumans JAP 2003, Pettersson
% JAP 1999, Heavens, Leckner, smiglie. Two corrections needed in
% Petterson: reflectivity term and equation 4, from Snells law; and
% modified by Kwang Hyup An 2009. For p-polarized and s-polarized light
% Everything put in SI units of m
% % % %
libpath = 'Library';
%libpath = 'E:\Steve Morris\Device Modeling\Library';
format long
output = struct;
%% build stack file %%
% read stack file only once
fid = fopen(char(stack),'r');
scan = textscan(fid, '%s %f %s');
fclose(fid);
% build stack file inputs
[t, film, ref, D, tau] = StackBuild(scan, tvar, mvar);
input.t = t*1E9;
input.film = film;
input.ref = ref;
input.D = D;
input.tau = tau;
input.phi0 = phi0;
input.polarization = polarization;
%% check the library for that stack
for N = 1:1
    if strfind(LibSave,'load') == 1
        output = LibraryLoad(t, film, ref, D, tau, phi0, polarization,
libpath);
    end
    if isfield(output,'EQE')==0
        output = OPV_EQE(input);
        LibrarySave(output,LibSave,libpath);
    end
end
end

%% Calculate the Abs, E-field, Ex gen, IQE, EQE, Jx %%
%%%%%%%%%%%%%%%%%%%%%%%%%%%%%%%%%%%%%%%%%%%%%%%%%%%%%%
function [output] = OPV_EQE(input)
t = input.t*1E-9;
t_top_substrate = t(2); %Used in TMM calculation for power transmitted
through glass substrate
t(2) = 0;   %Resets substrate thickness to zero to eliminate time
needed to calculate field in substrate
film = input.film;
ref = input.ref;
D = input.D;
tau = input.tau;
```

```
phi0 = input.phi0;
polarization = input.polarization;
%% Constants
global c eta0 h qe
c = 3*10^8;         % speed of light m/s
h = 6.626E-34;      % plank constant joule-s
qe = 1.602E-19;     % electron charge C/electron
eta0 = 8.854E-12; % free permativity (C^2)/(N m^2)= F/m = As/Vm
dz = .1*1E-9;       % mesh size for field distribution and Finite
                    % Difference Method (meters)

%% Wavelength Loop
s = size(t, 1)-2;         % total number of films in the stack

%spectrum data
lambda0 = 305;            % initial wavelength (nm)
dlambda = 5;              % wavelength stepping size (nm)
lambdaf = 800;            % final wavelength
lambda_s = lambda0:dlambda:lambdaf; % nm
M = size(lambda_s, 2);  % number of steps or data points of wavelength
% n in materials.mat only goes up to 900 nm, so this limits M
% except subpc only goes up to 800 nm
lambda_sm = (lambda_s)*10^-9;  % meters

%%
%pre-allocate variables
T = zeros(1,M);
R = zeros(1,M);
IglassITOp = zeros(1,M);
A_tot = zeros(1,M);
zend = round(sum(t(1:end-1))/1E-10);
EEp = zeros(zend, M);
Gp = zeros(zend, M);
EQESp = zeros(s+1,M);  % EQE per layer per wavelength
EQE_G_Sp = zeros(s+1,M);
EQE  = zeros(1,M);
EQE_G = zeros(1,M);
flux = zeros(s+1, M);
flux_pop = zeros(s+1,M);
G_pop = zeros(s+1,M);
pp = zeros(zend,M);
%%
% bb:   counter for wavelength until endpoint M
for bb = 1:M
    clear lambda n q xi x y z Ep Hp Ne Nph
    tt = zeros(1,zend);
    active = 0; % used later to determine heterjunction position

    % lambda is wavelength over which you are currently calculating (m)
    lambda = lambda_sm(bb);
    n = ref(:, bb);          % refractive index vector for stack at
lambda
    q = (n.^2 - n(1)^2*sin(phi0*pi/180)).^0.5;
    xi = q.*(2*pi/lambda);
```

```
    %% Transfer Matrix Model Calculation (Function located at bottom)
%%

%%%%%%%%%%%%%%%%%%%%%%%%%%%%%%%%%%%%%%%%%%%%%%%%%%%%%%%%%%%%%%%%%%%%

    % inputs
    % n:        refractive index for given wavelength, lambda
    % q:        propagation factor (angle dependent)
    % xi:      phase change wave experiences as it traverses the film
    % t:        thickness of each film
    % lambda:   wavelength currently under investigation, numerically
    % returns
    % tpp:      forward propagating transmission coefficient (p-
polarized)
    % tmp:      reverse propagating transmission coefficient (p-
polarized)
    [tpp,tmp,T(bb),R(bb),IglassITOp(bb),A_tot(bb)] = TMM(n, q, xi, t,
t_top_substrate, lambda, polarization); %IglassITOp(bb)


    %% Calculate EE (electric field), Q (time avg'd abs.), and G (exc.
gen. rate) for each layer%%

%%%%%%%%%%%%%%%%%%%%%%%%%%%%%%%%%%%%%%%%%%%%%%%%%%%%%%%%%%%%%%%%%%%%%%%
%%%%%%%%%%%%%%%%%%%%%%%

    for x = 2:s+1         % stack layer index
        dend = round(t(x)/dz); % total number of points in film
        for y = 1:dend     % layer segment index
            z = round(sum(t(1:x-1))/dz+y);       % mesh point within
entire stack
            tt(z) = sum(t(1:x-1))+y*dz;     % depth within device stack
(including glass)

            Ep = (tpp(x)*exp(1i*xi(x)*y*dz) + tmp(x)*exp(-
1i*xi(x)*y*dz))*(q(x)/n(x));
            EEp(z, bb) = IglassITOp(bb)*abs(Ep)^2;

            % time averaged absorbed power versus mesh point in stack
            Qp =
((4*pi*c*eta0*imag(n(x))*real(n(x)))/(2*lambda))*EEp(z, bb);
            Gp(z, bb) = (lambda/(h*c))*Qp;  %exciton generation rate
        end

        %% FD-ODE calculations %%
        %%%%%%%%%%%%%%%%%%%%%%%%%
        ext = char(film{x, 2}); % read the layer identifier tag
        if isempty(strfind(ext, 'active')) == 0

            d = dz*(1:dend);        % generate depth vector in meters

            % define vectors for exc gen, lifetime, and diff length
            Gv = Gp(round(sum(t(1:x-1))/dz+1):round(sum(t(1:x))/dz),
bb);
            clear tauv; tauv=ones(dend,1)*tau(x);
```

```
            bc = strrep(ext, 'active','');
            bc = strtok(bc,','); %remove extraneous info s.a. 'tvar1'
or 'mvar'
            switch bc
                case 'rd' %Reflect Left, Dissociate Right
                    [p, flux(x, bb), flux_pop(x, bb), G_pop(x, bb)] =
DriftDiffusion(D(x), tauv, Gv, 0, d, 01);
                case 'dr' %Dissociate Left, Reflect Right
                    [p, flux(x, bb), flux_pop(x, bb), G_pop(x, bb)] =
DriftDiffusion(D(x), tauv, Gv, 0, d, 10);
                case 'dd' %Dissociate Left & Right
                    [p, flux(x, bb), flux_pop(x, bb), G_pop(x, bb)] =
DriftDiffusion(D(x), tauv, Gv, 0, d, 11);
                case 'qd' %Quench Left, Dissociate Right
                    [p, flux(x, bb), flux_pop(x, bb), G_pop(x, bb)] =
DriftDiffusion(D(x), tauv, Gv, 0, d, 21);
                case 'dq' %Dissociate Left, Quench Right
                    [p, flux(x, bb), flux_pop(x, bb), G_pop(x, bb)] =
DriftDiffusion(D(x), tauv, Gv, 0, d, 12);
            end


            pp(round(sum(t(1:x-1))/dz)+(1:dend), bb) = p; % exc
population versus position
        end

        %% EQE Calculation For Each Wavelength %%
        %%%%%%%%%%%%%%%%%%%%%%%%%%%%%%%%%%%%%%%%%

        Nph = 0.5*c*eta0/(h*c/lambda);  % photons/(m^2 s)

        if active < 2
            Ne = abs(flux(x, bb));    % electrons/(m^2 s)
            Ne_G = abs(G_pop(x,bb));
        else
            Ne = abs(flux(x, bb));
            Ne_G = abs(G_pop(x,bb));
        end
        EQESp(x, bb) = Ne/Nph;  % EQE per layer per wavelength
        EQE_G_Sp(x,bb) = Ne_G/Nph;


    end

    EQE(bb) = sum(EQESp(:,bb));
    EQE_G(bb) = sum(EQE_G_Sp(:,bb));

end
HJ = 1;
J_HJ = 0;
for x = 1:s
```

```
    J_layer(x) = sum(qe*photonDens(lambda0:lambdaf).*interp1(lambda_s,
EQESp(x,:), lambda0:lambdaf)/10); % mA/(cm^2)
    J_HJ(HJ) = J_HJ(HJ)+J_layer(x);
    if strfind(film{x,2},'rz')==1
        HJ = HJ+1;
        J_HJ(HJ) = 0;
    end
end


%% Device Property Outputs %%
%%%%%%%%%%%%%%%%%%%%%%%%%%%%%
IQE_tot = EQE./A_tot;%IglassITOp.*IQE_tot; %Account for thick substrate
A_active = EQE_G;
IQE_active = EQE./A_active; %IglassITOp.*IQE_active;


% divide the current by the number of heterojunctions (series
operation)
J = min(J_HJ);

output.dz = dz;
output.t = t;
output.tt = tt;
output.pp = pp;
output.J = J;
output.J_layer = J_layer;
output.J_HJ = J_HJ;
output.EEp = EEp;
output.EQE = EQE;
output.IQE_tot = IQE_tot;
output.IQE_active = IQE_active;
output.A_active = A_active;
output.Qp = Qp;
output.Gp = Gp;
output.R = R;
output.T = T;
output.A_tot = A_tot;
output.IglassITOp = IglassITOp;
% save inputs as well
t(2) = t_top_substrate;
output.input.t = t*1E9;
output.input.film = film;
output.input.ref = ref;
output.input.D = D;
output.input.tau = tau;
output.input.phi0 = phi0;
output.input.polarization = polarization;
end

%% Look in the library for the device %%
%%%%%%%%%%%%%%%%%%%%%%%%%%%%%%%%%%%%%%%%
function [output] = LibraryLoad(t, film, ref, D, tau, phi0,
polarization, libpath)
    folder = film{1,1};
```

```
    file = num2str(t(1)*1E9);
    for x = 2:size(t,1)
        folder = strcat(folder,'_',film{x,1});
        file = strcat(file,'_',num2str(t(x)*1E9));
        if strfind(film{x,2},'active')==1
            ext_token = strrep(film{x,2}, 'active','');
            ext_token = strtok(ext_token,',');
            folder = strcat(folder,'.',ext_token);
        elseif strfind(film{x,2},'DDR')==1
            folder = strcat(folder,'DDR');
        end
    end
    file = strcat(file,'.mat');
    filepath = strcat(libpath,'/',folder,'/',file);
    A = dir(filepath);
    if size(A,1)>0
        load(filepath, 'output')
        % check if ref, D, tau, phi0, polarization exist
        check_exist = prod(1*isfield(output.input,{'D' 'tau' 'ref'
'phi0' 'polarization'}));
        if check_exist == 1
            % now you must check if ref, D, tau, phi0, polarization are
the same
            check_values(1) = prod(1*(output.input.D==D));
            check_values(2) = prod(1*(output.input.tau==tau));
            check_values(3) = prod(1*prod(1*(output.input.ref==ref)));
            check_values(4) = 1*(output.input.phi0==phi0);
            check_values(5) =
strcmp(output.input.polarization,polarization);
            if prod(check_values) == 1
                disp('loaded library file')
                return;
            end
            if check_values(1) == 0
                disp('D values do not match')
            end
            if check_values(2) == 0
                disp('tau values do not match')
            end
            if check_values(3) == 0
                disp('ref values do not match')
            end
            if check_values(4) == 0
                disp('phi0 values do not match')
            end
            if check_values(5) == 0
                disp('polarization values do not match')
            end
        else
            disp('missing a field! continuing with calculation');
        end
    end
    output = struct;
end
%% Save the device output to the library %%
%%%%%%%%%%%%%%%%%%%%%%%%%%%%%%%%%%%%%%%%%%%
```

```
function [] = LibrarySave(output,LibSave, libpath)
% warning!! EEp, Qp, and Gp are 2100 kB each!
% use rmfield(output.input, 'Gp') to remove them
    folder = output.input.film{1,1};
    file = num2str(output.input.t(1));
    for x = 2:size(output.input.t,1)
        folder = strcat(folder,'_',output.input.film{x,1});
        file = strcat(file,'_',num2str(output.input.t(x)));
        if strfind(output.input.film{x,2},'active')==1
            ext_token = strrep(output.input.film{x,2}, 'active','');
            ext_token = strtok(ext_token,',');
            folder = strcat(folder,'.',ext_token);
        elseif strfind(output.input.film{x,2},'DDR')==1
            folder = strcat(folder,'DDR');
        end
    end
    file = strcat(file,'.mat');
    filepath = strcat(libpath,'/',folder,'/',file);
if strfind(LibSave,'save') > 0
    if isdir(libpath)~= 1
        disp('library path not found!')
        return;
    end
    if isdir(strcat(libpath,'/',folder))~=1
        mkdir(libpath,folder);
    end
    if strfind(LibSave,'lite') > 0
        output = rmfield(output, {'Qp' 'EEp' 'Gp' 'pp' 'tt'});
    end
    save(filepath, 'output');
    disp('saved to library')
else
    disp('stack not saved, check LibSave tag');
end
end
%% Build a stack of material properties %%
%%%%%%%%%%%%%%%%%%%%%%%%%%%%%%%%%%%%%%%%%%
function [t, film, ref, D, tau] = StackBuild(scan, tvar, mvar)
% build the thickness vector and refractive index array via internal
% function, StackBuild

% inputs %
% stack:        name of text file containing stack information
% tvar:         array containing new thickness for film with tvar tag
in file
% mvar:         array containing new material for film with mvar tag in
file

% returns %
% t:            array containing thickness of each layer
% t_top_substrate:  thickness of second layer in stack (should be
either substrate or air)
% film:         array containing name of each film
% dev:          number of devices (defined by recombination zones [for
tandems])
% ref:          matrix of refractive index vs wavelength for each film
```

```
% Ld:           array containing exciton diffusion length for each film
% tau:          array containing exciton lifetime for each film
t = scan{2}*1E-9;
s = size(t,1);
%
ref = zeros(s,120);
D = zeros(1,s);
Ld = zeros(1,s);
tau = zeros(1,s);
film = cell(s,2);
% buld refractive index matrix of stack from materials database
for x = 1:s
    mat = char(scan{1}(x));
    ext = char(scan{3}(x));
    if isfinite(strfind(ext,'var')) == 1
        N = str2double(ext(strfind(ext, 'var')+3:size(ext,2)));
        switch ext(strfind(ext, 'var')-1)
            case 't'
                t(x) = tvar(N)*1E-9;
                disp([mat,' is now ',num2str(tvar(N)),' nm']);
            case 'm'
                mat = mvar{N};
                disp(['layer ',num2str(x),' is now ',mat]);
        end
    end
    % Load values from materials.mat (e.g. Ldsubpc, not Ld.subpc)
    vars = {['n',mat], ['D',mat], ['Ld',mat], ['tau',mat]};
    g = load('materials.mat', vars{:});
    ref(x,:) = g.(vars{1});
    D(x) = g.(vars{2});
    Ld(x) = g.(vars{3});
    tau(x) = g.(vars{4});
    film{x, 1} = mat;
    film{x, 2} = ext;

    clear(mat, 'g');
end
end
%% Transfer Matrix Method %%
%%%%%%%%%%%%%%%%%%%%%%%%%%%
function [tpp, tmp, Ti, Ri, IglassITOp, Ai] = TMM(n, ~, xi, d,
d_substrate, lambda, ~)
incov = @(S)[abs(S(1,1))^2 -abs(S(1,2))^2; abs(S(2,1))^2
(abs(det(S))^2-abs(S(1,2)*S(2,1))^2)/abs(S(1,1))^2];
% transposes are not necessary when the variable is properly initiated
d = transpose(d);
xi = transpose(xi);
layers = size(d, 2);
phi = zeros(1,layers);
d(2) = d_substrate;

x = 1;
kz(x) = 2*pi*n(x)/lambda*cos(phi(x));
beta(x) = d(x)*kz(x);
L(:,:,x) = [exp(-1i*beta(x)) 0; 0 exp(1i*beta(x))];
rp = zeros(1,layers-1);
```

```
tp = zeros(1,layers-1);
Ip = zeros(2,2,layers);
for x = 2:layers
    kz(x) = 2*pi*n(x)/lambda*cos(phi(x));
    beta(x) = d(x)*kz(x);
    L(:,:,x) = [exp(-1i*beta(x)) 0; 0 exp(1i*beta(x))];
    rp(x-1) = -(n(x)*cos(phi(x-1))-n(x-1)*cos(phi(x)))/(n(x)*cos(phi(x-
1))+n(x-1)*cos(phi(x))); % doesn't match paper convention, but is
correct
    %     rs(x-1) = (n(x)*cos(phi(x))-n(x-1)*cos(phi(x-
1)))/(n(x)*cos(phi(x))+n(x-1)*cos(phi(x-1))); % doesn't match paper
convention, but is correct
    tp(x-1) = 2*n(x-1)*cos(phi(x-1))/(n(x)*cos(phi(x-1))+n(x-
1)*cos(phi(x)));
    %     ts(x-1) = 2*n(x-1)*cos(phi(x-1))/(n(x)*cos(phi(x))+n(x-
1)*cos(phi(x-1)));
    Ip(:,:,x-1) = 1/tp(x-1)*[1 rp(x-1); rp(x-1) 1];
    %     Is(:,:,x-1) = 1/ts(x-1)*[1 rs(x-1); rs(x-1) 1];
end

% deteremine location of coherent stack (in a later release)
% xcheck = d > 1000E-9;
% currently this only applies to devices on glass/ito
x0 = 3;              % first layer of coherent stack
xend = layers-1;     % last layer of coherent stack
xb = xend;
% p-polarized section
Sp_left = Ip(:,:,x0-1);
Sp_right = Ip(:,:,xend);
rp_left(x0)  = Sp_left(2,1)/Sp_left(1,1);
rp_left_(x0) = -Sp_left(1,2)/Sp_left(1,1);
tp_left(x0)  = 1/Sp_left(1,1);
rp_right(xb) = Sp_right(2,1)/Sp_right(1,1);
tp_right(xb) = 1/Sp_right(1,1);
% % s-polarized section
% Ss_left = Is(:,:,x0-1);
% Ss_right = Is(:,:,xend);
% rs_left(x0)  = Ss_left(2,1)/Ss_left(1,1);
% rs_left_(x0) = -Ss_left(1,2)/Ss_left(1,1);
% ts_left(x0)  = 1/Ss_left(1,1);
% rs_right(xb) = Ss_right(2,1)/Ss_right(1,1);
% ts_right(xb) = 1/Ss_right(1,1);
for x = x0:xend
    xb = xb-1;
    % p-polarized
    Sp_left = Sp_left*L(:,:,x)*Ip(:,:,x);
    Sp_right = Ip(:,:,xb)*L(:,:,xb+1)*Sp_right;
    rp_left(x+1)  = Sp_left(2,1)/Sp_left(1,1);
    rp_left_(x+1) = -Sp_left(1,2)/Sp_left(1,1);
    tp_left(x+1)  = 1/Sp_left(1,1);
    rp_right(xb) = Sp_right(2,1)/Sp_right(1,1);
    tp_right(xb) = 1/Sp_right(1,1);
    %     % s-polarized
    %     Ss_left = Ss_left*L(:,:,x)*Is(:,:,x);
    %     Ss_right = Is(:,:,xb)*L(:,:,xb+1)*Ss_right;
    %     rs_left(x+1)  = Ss_left(2,1)/Ss_left(1,1);
```

```
    %     rs_left_(x+1) = -Ss_left(1,2)/Ss_left(1,1);
    %     ts_left(x+1)  = 1/Ss_left(1,1);
    %     rs_right(xb) = Ss_right(2,1)/Ss_right(1,1);
    %     ts_right(xb) = 1/Ss_right(1,1);
end
Ib23p = incov(Sp_left);
% Ib23s = incov(Ss_left);

tpp = tp_left(1:xend)./(1-
rp_left_(1:xend).*rp_right.*exp(1i.*2.*xi(1:xend).*d(1:xend)));
tmp = tpp.*rp_right.*exp(1i.*2.*xi(1:xend).*d(1:xend));
% tps = ts_left(1:xend)./(1-
rs_left_(1:xend).*rs_right.*exp(1i.*2.*xi(1:xend).*d(1:xend)));
% tms = tps.*rs_right.*exp(1i.*2.*xi(1:xend).*d(1:xend));
%
% r = Sp_left(2,1)/Sp_left(1,1);
% t = 1/Sp_left(1,1);
% Rc = abs(r)^2;
% % it is unclear how to handle the complex conjugate in Tc_p
% Tc_p =
abs(t)^2*real(conj(n(end)*cos(phi(end))))/real(n(1)*cos(phi(1)));
% Tc_s = abs(t)^2*real(n(end)*cos(phi(end)))/real(n(1)*cos(phi(1)));
% Ac = 1-Rc-Tc_p;

% incoherent section
Ib(:,:,1) = incov(Ip(:,:,1));
Lb(:,:,2) = abs(L(:,:,2)).^2;

Sb = Ib(:,:,1)*Lb(:,:,2)*Ib23p;
IglassITOp = [1,0]*Ib23p*[1/Sb(1,1);0];

Rbf = Sb(2,1)/Sb(1,1);  % reflectance at the front interface
Tbf = 1/Sb(1,1);        % transmittance at the front interface
% Rbr = -Sb(1,2)/Sb(1,1); % reflectance at the back interface
% Tbr = det(Sb)/Sb(1,1);  % transmittance at the back interface

Ri = Rbf;
Ti = Tbf*real(n(end))/n(1);
Ai = 1-Ri-Ti;
end
%% Diffusion Calculations %%
%%%%%%%%%%%%%%%%%%%%%%%%%%%%
function [pf, flux, flux_pop, G_pop] = DriftDiffusion(D, tau, G, R, d,
type)
% drift-diffusion solution - finite difference ODE45 method
% experimental code, ddtau and ddLd vary with layer position
% (c) 2012 Steven Morris, Adam Barito, University of Michigan LNECD

% ddLd^2/ddtau*d^2(p)/(dz)^2 - ddR + ddG = dp/dt

% ddLd is the diffusion length in meters
% ddtau is the exciton lifetime in seconds
% ddG is the generation rate in excitons/m^3/s
% ddR is the recombination rate in excitons/m^3/s
% p is the exciton population density, excitons/m^3
```

```
% d is the FD vector of thickness in m

% variables that must reach the BC functions
%global ddD ddtau ddG ddR dddz ddn

ddD = D;
ddtau = tau';
%ddLd = (ddD.*ddtau).^.5;
ddG = G;
ddR = R;

dddz = d(2) - d(1);
ddn = size(d, 2);
p0 = zeros(ddn, 1);    % presize the population density vector

switch type
    %% Reflect Left, Dissociate Right
    case 01

        ddG = flipud(ddG);

        M = zeros(ddn); %Initialize matrix with governing equation for
each mesh point
        M(1,1) = 1; %Zero value at left

        M(ddn,ddn) = -(2+(dddz^2/ddD/ddtau(ddn))); %Last row zero flux
        M(ddn,ddn-1) = 2;
        for i = 2:ddn-1
            for j = 1:ddn
                if i==j
                    M(i,j) = -(2+(dddz^2/ddD/ddtau(i)));
                elseif i == j+1
                    M(i,j) = 1;
                elseif i == j-1
                    M(i,j) = 1;
                end
            end
        end


        A = zeros(ddn,1); %Initialize right-hand-side vector
        for i = 2:ddn
            A(i) = -dddz^2/ddD*ddG(i);
        end
        pf = p0;
        pf = M\A;
        flux = ddD*abs(pf(1)-pf(2))/(1*dddz);
        pf = flipud(pf);

        flux_pop = 0;
        G_pop = 0;
        for i = 2:ddn
            flux_pop_i = dddz*(G(i) - pf(i)/tau(i));
            flux_pop = flux_pop + flux_pop_i;
```

```
            G_pop = G_pop + (G(i))*dddz;
        end
        %% Dissociate Left, Reflect Right
    case 10

        M = zeros(ddn); %Initialize matrix with governing equation for
each mesh point
        M(1,1) = 1; %Zero value at left
        M(ddn,ddn) = -(2+(dddz^2/ddD/ddtau(ddn))); %Last row zero flux
        M(ddn,ddn-1) = 2;
        for i = 2:ddn-1
            for j = 1:ddn
                if i==j
                    M(i,j) = -(2+(dddz^2/ddD/ddtau(i)));
                elseif i == j+1
                    M(i,j) = 1;
                elseif i == j-1
                    M(i,j) = 1;
                end
            end
        end

        A = zeros(ddn,1); %Initialize right-hand-side vector
        for i = 2:ddn
            A(i) = -dddz^2/ddD*ddG(i);
        end
        pf = p0;
        pf = M\A;
        flux = ddD*abs(pf(1)-pf(2))/(1*dddz);

        G_pop = 0;
        flux_pop = 0;
        for i = 2:ddn
            flux_pop_i = dddz*(G(i) - pf(i)/tau(i));
            flux_pop = flux_pop + flux_pop_i;
            G_pop = G_pop + (G(i))*dddz;
        end
        %% Dissociate Left & Right
    case 11

        ddG = flipud(ddG);

        M = zeros(ddn); %Initialize matrix with governing equation for
each mesh point
        M(1,1) = 1; %Zero value at left

        M(ddn,ddn) = 1;
        for i = 2:ddn-1
            for j = 1:ddn
                if i==j
                    M(i,j) = -(2+(dddz^2/ddD/ddtau(i)));
                elseif i == j+1
                    M(i,j) = 1;
                elseif i == j-1
                    M(i,j) = 1;
```

```
                end
            end
        end


        A = zeros(ddn,1); %Initialize right-hand-side vector
        for i = 2:ddn -1
            A(i) = -dddz^2/ddD*ddG(i);
        end

        pf = p0;
        pf = M\A;
        flux = ddD*(abs(pf(1)-pf(2))/(1*dddz) + abs(pf(ddn)-pf(ddn-
1))/dddz); %Cascade

        pf = flipud(pf);
        flux_pop = 0;
        G_pop = 0;
        for i = 2:ddn
            flux_pop_i = dddz*(G(i) - pf(i)/tau(i));
            flux_pop = flux_pop + flux_pop_i;
            G_pop = G_pop + (G(i))*dddz;
        end
        %% Quench Left, Dissociate Right
    case 21
        ddG = flipud(ddG);

        M = zeros(ddn); %Initialize matrix with governing equation for
each mesh point
        M(1,1) = 1; %Zero value at left

        M(ddn,ddn) = 1;
        for i = 2:ddn-1
            for j = 1:ddn
                if i==j
                    M(i,j) = -(2+(dddz^2/ddD/ddtau(i)));
                elseif i == j+1
                    M(i,j) = 1;
                elseif i == j-1
                    M(i,j) = 1;
                end
            end
        end


        A = zeros(ddn,1); %Initialize right-hand-side vector
        for i = 2:ddn -1
            A(i) = -dddz^2/ddD*ddG(i);
        end

        pf = p0;
        pf = M\A;
        flux = ddD*(abs(pf(1)-pf(2))/(1*dddz)); %Quenching
```

```
        pf = flipud(pf);

        flux_pop = 0;
        G_pop = 0;
        for i = 2:ddn
            flux_pop_i = dddz*(G(i) - pf(i)/tau(i));
            flux_pop = flux_pop + flux_pop_i;
            G_pop = G_pop + (G(i))*dddz;
        end
        %% Dissociate Left, Quench Right
    case 12 %
        M = zeros(ddn); %Initialize matrix with governing equation for
each mesh point
        M(1,1) = 1; %Zero value at left

        M(ddn,ddn) = 1;
        for i = 2:ddn-1
            for j = 1:ddn
                if i==j
                    M(i,j) = -(2+(dddz^2/ddD/ddtau(i)));
                elseif i == j+1
                    M(i,j) = 1;
                elseif i == j-1
                    M(i,j) = 1;
                end
            end
        end


        A = zeros(ddn,1); %Initialize right-hand-side vector
        for i = 2:ddn -1
            A(i) = -dddz^2/ddD*ddG(i);
        end

        pf = p0;
        pf = M\A;
        flux = ddD*(abs(pf(1)-pf(2))/(1*dddz)); %Quenching

        pf = flipud(pf);

        flux_pop = 0;
        G_pop = 0;
        for i = 2:ddn
            flux_pop_i = dddz*(G(i) - pf(i)/tau(i));
            flux_pop = flux_pop + flux_pop_i;
            G_pop = G_pop + (G(i))*dddz;
        end

    case 2

        ddG = flipud(ddG);
```

```
        M = zeros(ddn); %Initialize matrix with governing equation for
each mesh point
        M(1,1) = 1; %Zero value at left

        M(ddn,ddn) = 1;
        for i = 2:ddn-1
            for j = 1:ddn
                if i==j
                    M(i,j) = -(2+(dddz^2/ddD/ddtau(i)));
                elseif i == j+1
                    M(i,j) = 1;
                elseif i == j-1
                    M(i,j) = 1;
                end
            end
        end

        A = zeros(ddn,1); %Initialize right-hand-side vector
        for i = 2:ddn -1
            A(i) = -dddz^2/ddD*ddG(i);
        end

        pf = p0;
        pf = M\A;
        flux = ddD*(abs(pf(1)-pf(2))/(1*dddz)); %Quenching
        %flux = ddD*(abs(pf(1)-pf(2))/(1*dddz)); %SubPc/C60
        %flux = ddD*(abs(pf(ddn)-pf(ddn-1))/(1*dddz)); %NPD/SubPc

        pf = flipud(pf);

        flux_pop = 0;
        G_pop = 0;
        for i = 2:ddn
            flux_pop_i = dddz*(G(i) - pf(i)/tau(i));
            flux_pop = flux_pop + flux_pop_i;
            G_pop = G_pop + (G(i))*dddz;
        end

end

clear ddLd ddtau ddG ddR dddz ddn
end
```

---

end of OPV_Back_v3beta.m

EQE_dataExt

```
% This program is for reading data from the EQE measurement, and
% analyzing the data to calculate EQE-Lambda
% Developed by Kwang Hyup An, 2008
% Copyright @ Max Shtein, Kevin Pipe, Kwang Hyup An
% Modified by Steven Morris

function [EQE, WL] = EQE_dataExt(filename,ADEV,sens, refsens)
fn_dev        = strcat(filename,'.txt');
% Current data file from the device
fn_ref        = strcat(filename,'_ref.txt');
% Reference light power from the Si-Detector

LOCK_SEN_DEV  = sens;
%in mV, Lock-in amplifier SENSITIVITY for device measurement
LOCK_SEN_PIN  = refsens;
%in mV Lock-in amplifier SENSITIVITY for Si-detector measurement
PMETER_RNG    = 6.113; %in uW ; Si-Detector power meter setting (Range)
AMP           = 1E6; %V/A ;
AHOLE         = pi*0.25*(0.001)^2;
% Hole area in the thick metal mask placed on the Si-Detector
ADEV          = ADEV/10000;
% Actual measured device area

% START WAVELENGTH SHOULD BE 350 nm;
% FINAL WAVELENGTH SHOULD BE 900 nm;
% WAVELENGTH INTERVAL SHOULD BE 5 nm;

% RESPONSITIVITY DATA COMES FROM THE Si-detector calibration data
Responsivity=[0.227262482   ,0.258918244    ,0.289142175
,0.317995721    ,0.345538574    ,0.371828694    ,0.396922336
,0.420874074    ,0.443736825    ,0.465561873    ,0.486398897
,0.506295993    ,0.5252997  ,0.543455021    ,0.560805456
,0.577393019    ,0.593258263    ,0.608440312    ,0.622976878
,0.636904288    ,0.650257511    ,0.66307018 ,0.675374618
,0.687201864    ,0.698581692    ,0.709542646    ,0.720112053
,0.730316057    ,0.740179639    ,0.749726642    ,0.7589798
,0.767960755    ,0.776690088    ,0.785187343    ,0.793471049
,0.801558746    ,0.809467012    ,0.817211484    ,0.824806885
,0.832267048    ,0.839604941    ,0.846832693    ,0.853961616
,0.86100223 ,0.867964292    ,0.874856815    ,0.881688098
,0.888465744    ,0.895196692    ,0.901887239    ,0.908543061
,0.915169245    ,0.921770307    ,0.92835022 ,0.934912438
,0.941459923    ,0.947995165    ,0.95452021 ,0.961036686
,0.967545824    ,0.974048484    ,0.980545183    ,0.987036115
,0.993521179    ,1  ,1.00647196 ,1.012936216    ,1.019391729
,1.025837287    ,1.032271532    ,1.038692981    ,1.045100051
,1.051491091    ,1.057864394    ,1.064218235    ,1.070550887
,1.076860647    ,1.083145865    ,1.089404962    ,1.095636463
,1.101839015    ,1.108011413    ,1.114152626    ,1.120261824
,1.126338398    ,1.132381986    ,1.138392501    ,1.144370152
,1.150315471    ,1.156229336    ,1.162112996    ,1.167968099
,1.17379671 ,1.179601343    ,1.185384982    ,1.191151106
,1.196903712    ,1.202647345    ,1.208387117    ,1.214128735
```

```
,1.21987852,1.21987852,1.21987852,1.21987852,1.21987852,1.21987852,1.21
987852,1.21987852,1.21987852,1.21987852,1.21987852];
Responsivity=Responsivity';
%####################################

H = 6.626E-34;
C = 299792000;
Q = 6.242E18;

fid = fopen(fn_dev,'r');
[rawdata, count] = fscanf(fid, '%g %g', [2 inf]);
fclose(fid);
rawdata = rawdata';
WL = rawdata(:,1);
fcurrent = rawdata(:,2);
praw = importdata(fn_ref);
pin = interp1(round(praw(:,1))',praw(:,2)',round(WL));
Resp = interp1([350:5:900],Responsivity,WL);
clear rawdata;

% calculating input power and number of photon
LOCK_SEN_PIN  = LOCK_SEN_PIN/10;
pin           = (LOCK_SEN_PIN*sqrt(2)*0.001*PMETER_RNG)*pin;
intensity     = (1.E-6/AHOLE)*pin./Resp;
NPH           = (ADEV*1.E-9/H/C)*intensity.*WL;

% calculating generated h+ and e- pairs
LOCK_SEN_DEV  = LOCK_SEN_DEV/10;
current       = (LOCK_SEN_DEV*sqrt(2)*0.001/AMP)*fcurrent;
NCH           = Q*current;

% EXTERNAL QUANTUM EFFICIENCY DATA
EQE           = NCH./NPH;
%%%%%%%%%%%%%%%%%%%%%%%%%%%%%%%%%%
end
```

End of ‘EQE_dataExt.m’

APPENDIX B

JV MODEL

Script to plot JV curves

```
%% Figure 3 - JV curve
clear dev

% load JV data for substrate 130625
load('130625\130625JV.mat')
mexclude_cl = [10];      % ignore bad device
m0_cl = size(dev,2);
mexsize_cl = size(mexclude_cl,2);
n0 = size(dev(1).j,2);
JVmatrix = zeros(n0,m0_cl-mexsize_cl);
for n = 1:n0
    p=0;
    for m = 1:m0_cl
        if any(m==mexclude_cl)==0
            p = p+1;
            JVmatrix(n,p) = dev(m).j(n);
        end
    end
end
J_cl = mean(JVmatrix,2);
Jsd_cl = std(JVmatrix,0,2);
t_star_cl = tinv(0.95, m0_cl-mexsize_cl-1);
V_cl = dev(1).v;
dev.v = V_cl;

%%% BEGIN GIEBINK %%%
r_pp = 0.922E-7;
dev.X = -0.15;
dev.HOMO_D = 5.60;

JxD = 1.0;
JxA = 1.0/110;
load('Giebink Model/devfit130625AB.mat')
dev.nD = devfit.nD;
dev.nA = devfit.nA;
dev.JsD = JxD*devfit.JsD;
dev.JsA = JxA*devfit.JsA;
```

```
dev.Rs = devfit.Rs/20;        % device series resistance (Ohms/cm^2)
dev.Rsh = devfit.Rsh*1E20;    % device shunt resistance (Ohms/cm^2)
dev.Spc = 0.0000;
%
dev.T = 300;      % materials temperature (K)
dev.Jx0 = 0;      % exciton photocurrent reaching HJ (mA/cm^2)
dev.a0 = r_pp;    % PP separation distance (cm)
dev.taur =120E-9; % PP lifetime (s)
% layer thicknesses
dev.d = 64E-7;    % device thickness (cm)
dev.tD = 13E-7;   % donor thickness (cm)
dev.tA = 36E-7;   % acceptor thickness (cm)
% energy levels
dev.wf_An = 6.02; % anode work function (eV)
dev.wf_Ca = 4.0;  % cathode work function (eV)
%dev.HOMO_D = 5.45;     % HOMO level of donor (eV)
dev.LUMO_A = 3.7; % LUMO level of acceptor (eV)
% organic properties
dev.epsr = 4.1;         % relative permittivity
dev.mun_0 = 5.2E-10;    % zero field electron mobility (cm^2/V/s)
dev.gamman = 1.2E-3;    % Poole-Frankel electron mobility coefficient
                        % [(m/V)^(1/2)]
dev.mup_0 = 2.8E-5;     % zero field hole mobility (cm^2/V/s)
dev.gammap = 7.6E-4;    % Poole-Frankel hole mobility coefficient
%
kb = 8.617E-5;
T = 300;
EHL = dev.HOMO_D-dev.LUMO_A+dev.X;
dev.JsD =   JxD*devfit.JsD*exp(-(EHL-1.9)/devfit.nD/kb/T);
dev.JsA =  JxA*devfit.JsA*exp(-(EHL-1.9)/devfit.nA/kb/T);
dev.Jx0 = 4.2     % exciton photocurrent reaching HJ (mA/cm^2)
dev.a0 = r_pp;    % PP separation distance (cm)
dev.cl = GRfun(dev);

figure(3); clf;
hold all
box
axis([-0.5 1.2 -5 2])
set(gca, 'FontSize', FontSize,'linewidth',BorderThickness)
xlabel('Bias(V)', 'fontsize', FontSize);
ylabel('Current Density (mA/cm^2)', 'fontsize', FontSize);
line([-1 5],[0 0], 'Color', 'black', 'LineWidth', AxesThickness);
line([0 0],[-10 10], 'Color', 'black', 'LineWidth', AxesThickness);
plot(V_cl,J_cl,'black', 'LineWidth', LineThickness)
jbfill(V_cl, transpose(J_cl+t_star_cl*Jsd_cl/sqrt(m0_cl-mexsize_cl)),
transpose(J_cl-t_star_cl*Jsd_cl/sqrt(m0_cl-mexsize_cl)), 'blue',
'blue',0,Transp)
```

end of Giebink script

‘GRfun.m’ - iterative calculation of JV points

```
function Dev = GRfun(Dev)
% GiebinkRenshaw Fitting is for fitting bilayer organic photovoltaics.
Devices will be read in from experimental data using ReadDevileFile,
and both log-linear (fig 2) and linear-linear (fig 2) plots will be
generated where it's best to use the light curve for fitting taur and
the dark curve for fitting nD, nA, JsD0, and JsA0. The final plot will
be a superposition of two diode curves, where Js controls the "height"
and n controls the slope of each curve on fig 1. curve. Seeing as it is
a superposition, it is possible that the dark curve will show one layer
dominate at low bias and the other dominate at higher bias. In the
example below, first the donor will dominate (0 to 1.2V), then the
acceptor (1.2 to 1.5V), then the series resistance (>1.5V). Consider
this when attempting to fit the dark current.
%% Example Values
% nD   = 18;        % ideality factor in donor
% nA   = 1.9;       % ideality factor in acceptor
% JsD0 = 50E9;      % (dark saturation current)/a/krecp (A/cm^3) in
donor
% JsA0 = 9E5;       % (dark saturation current)/a/krecn (A/cm^3) in
acceptor
% taur = 1E-9;      % PP recombination time(s)
% a0   = 3E-7;      % initial PP separation distance (cm)
% Rs = 50;          % series resistance (Ohm-cm^2)
% Jx0 = 0;          % HJ exciton flux (mA/cm^2)
% Spc = 0;          % photoconductance (mA/V-cm^2)
% T = 300;          % device temperature (K)
% Vbi = 2.4;        % built-in potential
% E_HL = 1.8;       % heterojunction energy level offset (eV)
% phi_Ac = 0.4;     % cathode injection barrier (eV)
% phi_Do = -1;      % anode injection barrier (eV)
% mun_0 = 5.2E-10;  % zero field electron mobility (cm^2/V/s)
% gamman = 1.2E-3;  % Poole-Frankel electron mobility coefficient
[(m/V)^(1/2)]
% mup_0 = 2.8E-5;   % zero field hole mobility (cm^2/V/s)
% gammap = 7.6E-4;  % Poole-Frankel hole mobility coefficient
[(m/V)^(1/2)]
% d = 44E-7;        % total organic thickness (cm)
% tA = 27E-7;       % acceptor thickness (cm)
% tD = 7E-7;        % donor thickness (cm)
%%%%%%%%%%%%%%%%%%%%%%%%%%%%%%%%%%%%%%%%%%%%%%%%%%%%%%%%%%%%%%%%%%%%%%%
% volage sweep
Vstart = Dev.v(1);        % starting bias
dV = Dev.v(2)-Dev.v(1);     % bias increment
Vend = Dev.v(end);        % ending bias

kr   = 1/(Dev.taur);    % PP recombination rate (1/s)
%%%%%%%%%%%%%%%%%%%%%%%%%%%%%%%%%%%%%%%%%%%%%%%%%%%%%%%%%%%%%%%%%%%%%%%
Va = Vstart;
% according to the Giebink model, Jph = -q*Jx*(kppd/(kppd+kppr)), and
Jsc = Jph when Va = 0. We can approximate the electric field in the
device as Vbi/thickness intead of solving the poisson equation.

% Environmental properties
q = 1.6E-19;        % charge on carrier (C/electron)
kb = 1.38065E-23;   % boltzmann constant (J/K)
```

```
eps0 = 8.854E-14;   % vacuum permittivity (F/cm)
beta = q/kb/Dev.T;  % "voltage" of environment (V)
eps = Dev.epsr*eps0;% permittivity of medium (F/cm)

Vbi     = Dev.wf_An-Dev.wf_Ca;      % built-in potential (V)
E_HL    = Dev.HOMO_D-Dev.LUMO_A;    % interfacial gap (eV)

% electric field calculations (assuming linear profile, SCLC)
delA = Dev.tA/Dev.d;    % fraction of potential dropped across acceptor
delD = Dev.tD/Dev.d;    % fraction of potential dropped across donor
FI = (Va-Vbi)/Dev.d;    % field at interface assuming linear profile
Jx = Dev.Jx0/1000/q;    % exciton flux (A/cm^2)/q

% zero applied field electron mobility in acceptor
mun = @(FI)Dev.mun_0*exp(Dev.gamman*abs(FI)^.5);
mup = @(FI)Dev.mup_0*exp(Dev.gammap*abs(FI)^.5);

% langevin coefficients
krecn = q*mun(Vbi/Dev.d)/eps; % bimolecular recombination constant
krecp = q*mup(Vbi/Dev.d)/eps; % bimolecular recombination constant
krec = (krecp + krecn);       % total constant

% PP separations (a), and distribution at each separation (X)
a = Dev.a0;
X = 0;

% zero applied field forward (dissociation) rate constant
Epp =  q./(4.*pi().*eps.*a)+Dev.X;    % distribution of PP energies
b = -q^3*(-Vbi/Dev.d)/(8*pi()*eps*kb^2*Dev.T^2);
Y = 1;
for m = 1:20
    Y = Y + b^m*(-1)^m*(-2)^m/factorial(m)/gamma(m+2);
end
kf00 = (3./4./pi()./a.^3).*krec.*exp(-Epp.*q./kb./Dev.T)*Y
kf0(1:size(a,2)) = kf00;%trapz(a, X.*kf00);
kr(1:size(a,2)) = kr;
Spc = Dev.Spc;       % photoconductance (mA/V-cm^2)

% trap dominant regime (low intensity, nt,pt>>n,p)
% recombination primarily occurs at trap states (i.e. a free electron,
n_I, in the donor recombines with a trapped hole, p_It, in the donor
and vice versa)

Va = 0.0;
FI = (Va-Vbi)/Dev.d;
krecn = q*mun(FI)/eps;   % bimolecular recombination constant
krecp = q*mup(FI)/eps;   % bimolecular recombination constant
krec = krecn + krecp;
%%%%%%%%%%%%%%%%%%%%%% CALCULATE KF AN ETA %%%%%%%%%%%%%%%%%%%%%%%%%%%
if Va < Vbi
    b = -q^3*FI/(8*pi()*eps*kb^2*Dev.T^2);
    F = 1;      % field induced dissociation factor
    for y = 1:100
        F = F + b^y*(-1)^y*(-2)^y/factorial(y)/gamma(y+2);
    end
```

```
    kf = (3./4./pi()./a.^3).*krec.*exp(-Epp.*q./kb./Dev.T).*F;
else
    rc = q^2/(4*pi()*eps*kb*Dev.T); % onsager exciton radius
    dE = FI*rc;
    kf = (3./4./pi()./a.^3).*krec.*exp(-(Epp+dE).*q./kb./Dev.T);
end
eta = kf./(kf+kr);
JsD = a.*(1-eta).*krecp;
JsA = a.*(1-eta).*krecn;

if isfield(Dev, 'JsD') == 1
    Dev.JsD0 = Dev.JsD/trapz(a, X.*JsD);
end
if isfield(Dev, 'JsA') == 1
    Dev.JsA0 = Dev.JsA/trapz(a, X.*JsA);
end

% find at V=0
%%%%%%%%%%%%%%%%%%%%%%%%%%%%%%%%%%%%%%%%%%%%%%%%%%%%%%%%%%%%%%%%%%%%%%%%%%
%%%%%%%%%%%%%%%%%%%%%%%%%%%%%%%%%%%%%%%%%%%%%%%%%%%%%%%%%%%%%%%%%%%%%%%%%%
Va = 0;
x0 = interp1(Dev.v,1:max(size(Dev.v)),0);
x = x0;
FI = (Va-Vbi)/Dev.d;
krecn = q*mun(FI)/eps;   % bimolecular recombination constant
krecp = q*mup(FI)/eps;   % bimolecular recombination constant
Jguess = Jx*q;
[J(x) JsD(x) JsA(x)] = GRcalc(Va, Jguess, Vbi, Jx, Spc, kr, kf00,
krecn, krecp, Dev, q, eps, kb, a, X, Epp);

% solve for V>0, starting at V = 0
parfor x = (x0+1):floor((Vend-Vstart)/dV+2)
    Va = Vstart+(x-1)*dV;
    FI = (Va-Vbi)/Dev.d;
    krecn = q*mun(FI)/eps;   % bimolecular recombination constant
    krecp = q*mup(FI)/eps;   % bimolecular recombination constant
    Jguess = 0;
    [J(x) JsD(x) JsA(x)] = GRcalc(Va, Jguess, Vbi, Jx, Spc, kr, kf00,
krecn, krecp, Dev, q, eps, kb, a, X, Epp);
end

parfor x = 1:(x0-1)
    Va = Vstart+(x-1)*dV;
    FI = (Va-Vbi)/Dev.d;
    krecn = q*mun(FI)/eps;   % bimolecular recombination constant
    krecp = q*mup(FI)/eps;   % bimolecular recombination constant
    Jguess = 0;%J(x+1);
    [J(x) JsD(x) JsA(x)] = GRcalc(Va, Jguess, Vbi, Jx, Spc, kr, kf00,
krecn, krecp, Dev, q, eps, kb, a, X, Epp);
end

Dev.Jgr = J;
Dev.JsD = JsD;
Dev.JsA = JsA;
end
```

```
function [J JsD JsA] = GRcalc(Va, Jguess, Vbi, Jx, Spc, kr, kf00,
krecn, krecp, Dev, q, eps, kb, a, X, Epp)
FI = (Va-Vbi)/Dev.d;

krec = krecn + krecp;
%%%%%%%%%%%%%%%%%%%%%% CALCULATE KF AN ETA %%%%%%%%%%%%%%%%%%%%%%%%%%%
if Va < Vbi
    b = -q^3*FI/(8*pi()*eps*kb^2*Dev.T^2);
    F = 1;      % field induced dissociation factor
    for y = 1:100
        F = F + b^y*(-1)^y*(-2)^y/factorial(y)/gamma(y+2);
    end
    kf = (3./4./pi()./a.^3).*krec.*exp(-Epp.*q./kb./Dev.T).*F;
else
    rc = q^2/(4*pi()*eps*kb*Dev.T); % onsager exciton radius
    %dE = q*FI*(sqrt(rc^2-a(z)^2*sin(theta)^2)-a(z)*cos(theta));
    dE = FI*rc;
    kf = (3./4./pi()./a.^3).*krec.*exp(-(Epp+dE).*q./kb./Dev.T);
end
eta = kf./(kf+kr);
JsA = a.*(1-eta).*krecn.*Dev.JsA0;
JsD = a.*(1-eta).*krecp.*Dev.JsD0;

for z = 1:size(a,2)
    % function for calculating current density, Jfun = 0 for implicit
    % solution of J at each PP separation distance
    Jfun = @(J)(Dev.Rsh/(Dev.Rs+Dev.Rsh))*JsD(z).*(exp(q.*(Va-
J.*Dev.Rs)./Dev.nD./kb./Dev.T)-kf(z)./kf00(z))...
        +(Dev.Rsh/(Dev.Rs+Dev.Rsh))*JsA(z).*(exp(q.*(Va-
J.*Dev.Rs)./Dev.nA./kb./Dev.T)-kf(z)./kf00(z))...
        +Va/(Dev.Rs+Dev.Rsh)...
        -q.*eta(z).*Jx...
        +Spc.*(Va-J.*Dev.Rs-Vbi)...
        -J;
    J0(z) = fzero(Jfun, -Jguess); % find root of Jfun for implicit soln
(A/cm^2)
end
J = trapz(a, X.*J0); % array for current density (A/cm^2)
JsD = trapz(a, X.*JsD);
JsA = trapz(a, X.*JsA);
%%%%%%%%%%%%%%%%%%%%%%%%%% DONE %%%%%%%%%%%%%%%%%%%%%%%%%%%%%%%%%%%%%%
end
```

end of 'GRfun.m'